Using a Mouse Model to Study the Role of PBRM1 Loss in the Development of Clear Cell Renal Cell Carcinoma

Author: Niklas Kupfer

Examiner:

Prof. Dr. Tuncay Baubec

Host supervisor:

Prof. Sir Peter J. Ratcliffe

Ratcliffe Lab,

Target Discovery Institute, University of Oxford

Final report of the general research profile in

Molecular and Cellular Life Science, M.Sc.

Utrecht, 10.09.2024

I. Abstract

A fundamental challenge when studying the evolution and origin of cancer is understanding the early events following oncogenic mutations. In the case of clear cell renal cell carcinoma (ccRCC), the truncal event is the inactivation of the von Hippel-Lindau (*VHL*) tumour suppressor gene. However, despite this event being near universal in all ccRCC cases, *VHL* inactivation alone does not lead to the formation of tumours, and the inactivation of a second tumour suppressor gene is needed for tumorigenesis. This raises important questions about how the concomitant loss of these tumour suppressors drives tumorigenesis and what early changes this loss imposes on cells.

To investigate these early events of ccRCC evolution, this study utilises a reporter mouse model that combines the inducible inactivation of *Vhl* with the expression of a tdTomato fluorescent marker in the renal tubular epithelium. This enables visualisation and extraction of *Vhl*-null cells from renal tissues before they undergo morphological alterations. This model was further expanded for the Polybromo-1 (*Pbrm1*) gene, the second most commonly mutated gene in ccRCC. By integrating histological assessments, molecular profiling, and digital pathology techniques, this study investigates time-dependent changes in survival, expansion, morphology, and clustering of renal tubular epithelial cells after *Vhl* and/or *Pbrm1* inactivation. In addition, transcriptome analysis was carried out to elucidate the early changes imposed on cells after losing *Vhl* and *Pbrm1*.

The study revealed that while *Pbrm1* inactivation does not significantly alter the expansion of *Vhl*-null cells within the kidney cortex, it plays a crucial role in driving early tumour-like morphological changes. Notably, the combined loss of *Vhl* and *Pbrm1* results in the formation of dysplastic tumour-like lesions and cystic tubules, morphological alterations that do not appear when either gene is inactivated alone. Interestingly, despite these morphological shifts,

transcriptome analyses showed that the impact of *Pbrm1* inactivation on the gene expression profile of *Vhl*-null cells is relatively modest.

These results provide new perspectives on the early molecular and cellular changes that lead to ccRCC. They suggest that while *Pbrm1* inactivation is necessary for initiating structural abnormalities in *Vhl*-null cells, its transcriptional effects are less pronounced than anticipated. This work highlights the need for further investigation into non-transcriptional mechanisms in ccRCC development and advances our understanding of the early stages of cancer evolution driven by *Vhl* and *Pbrm1* mutations.

II. Layman Summary

Human cancer is not just one but a group of many diseases that can be found in different forms in nearly every organ. These diseases have in common that they are defined by uncontrolled cell division and potential invasion of other organs. Although all of these diseases are called cancer, their cause, progression, and therefore the way we try to treat them is very different from one another. Commonly the cause of cancer is an undetected or unrepaired change in the DNA of cells, called mutation, which leads them to acquire an evolutionary advantage over other cells and persist in the tissue. Oftentimes, these cells acquire additional mutations over time which are necessary in order to form cancer.

This study is investigating the development of clear cell renal cell carcinoma (ccRCC) which is the most common form of kidney cancer. In this case, the truncal mutation acquired by cells is causing the loss of the Von Hippel-Lindau gene (*VHL*). This gene encodes for a protein which is a central component of the oxygen sensing mechanism of the cell. When the pVHL protein is lost, the cells think that there is not enough oxygen present for it to operate normally and they initiate a cascade of measures to adapt to this lack of oxygen. Amongst others, these measures promote the growth of blood vessels and change the cellular metabolism to be more oxygen-independent. Although these measures are beneficial for tumour growth, losing VHL alone has shown to be insufficient to cause cancer. In the case of ccRCC, a second mutation is needed to form cancer. The most common second mutation is causing the loss of the PBRM1 protein. This protein is involved in many cellular processes like remodelling the 3D structure of DNA and ensuring the stability of chromosomes during cell division. It is known that *Vhl* loss and *Pbrm1* loss together in the same cell can cause cancer in mice, but how exactly the loss of *Pbrm1* cooperates with *Vhl* loss to do so is little understood. Therefore, in this study, we use a mouse model which deletes either one or both of these genes and marks cells that have

lost these genes with a fluorescent marker. This not only helps us to see cells carrying these mutations before they undergo any kind of morphological change but also to extract them from the tissue and study them on their own. By doing this we are able to get information on how these cells behave in their native tissue and how they change over time. Additionally, by extracting them we aim to find out how exactly the loss of *Pbrm1* interacts with the loss of *Vhl* to form cancer.

III. Acknowledgements

Hereby, I want to express my deep gratitude to Professor Sir Peter J. Ratcliffe for the opportunity to do my research project in his research group. I am very grateful for the chance to work on this amazing project and the pleasant working environment. I greatly appreciate the help and support I have received before, during, and after the work on my thesis and I highly value the efforts that have been made to make this incredible experience possible.

I want to extend my gratitude to Professor Christopher W. Pugh and Professor David R. Mole for sharing their incredible expertise during discussions and want to thank them for all the help and support I have received during my internship.

I also want to express my gratitude to my daily supervisors Dr. Julie Adam, Dr. Joanna D. C. C. Lima, and Dr. Samvid Kurlekar for the excellent supervision and guidance I have received during this internship. I am deeply thankful for the time they have invested in sharing their exceptional knowledge with me, in the wet and dry lab, which helped me grow as a scientist immensely. I am very grateful for the inspiring work ethic and motivation they bring to the lab. I am very thankful for being able to join their project and for all the effort that went into creating the basis for this thesis.

Further, I want to thank Dr. Ran Li for her help and expertise in the dry lab and for conducting the preprocessing of my RNA sequencing data.

I want to thank the entire Ratcliffe Lab for making this internship a very enjoyable experience. I am extremely grateful for all the help and support I received and for the warm and welcoming atmosphere. I wish everyone the best of luck for their future.

Last but not least, I want to thank the Nijbakker-Morra Foundation which has financially supported me during this internship with the master's student internship grant.

IV. Table of Contents

IV. List of Figures

VI. List of Tables

VII. List of Abbreviations

Abbreviations	Term
Aldoc	Aldolase C (mouse gene)
ANOVA	Analysis of Variance
Apoc3	Apolipoprotein C-III (mouse gene)
ARID2	AT-Rich Interaction Domain 2
BAF180	BRG1-associated factor 180
BAH	Bromo Adjacent Homology
BAP1	BRCA1-Associated Protein 1
BH	Benjamini - Hochberg
BRCA1	Breast Cancer 1
BRD7	Bromodomain Containing 7
BrdU	5-bromo-2'-deoxyuridine
BRG1	Brahma-Related Gene 1
BSA	Bovine Serum Albumin
ccRCC	Clear Cell Renal Cell Carcinoma
CDKN1A	Cyclin-Dependent Kinase Inhibitor 1A
Cre	Cre recombinase
Cp	Ceruloplasmin
DAB	3,3′-Diaminobenzidine
Defb19	Defensin Beta 19 (mouse gene)
DNA	Deoxyribonucleic Acid
DPX	Dibutylphthalate Polystyrene Xylene

DTT	Dithiothreitol
Efhd1	EF-Hand Domain Family Member 1 (mouse gene)
ER	Estrogen Receptor
FACS	Fluorescence-Activated Cell Sorting
FBS	Fetal Bovine Serum
FC	Fold Change
FDR	False Discovery Rate
FFPE	Formalin-Fixed, Paraffin-Embedded
fl	loxP-flanked (floxed)
HIF	Hypoxia-Inducible Factor
HMG	High Mobility Group
IHC	Immunohistochemistry
Ipo3	Importin 3 (mouse gene)
JAK-STAT	Janus Kinase-Signal Transducer and Activator of Transcription
KEGG	Kyoto Encyclopedia of Genes and Genomes
Ki67	Marker of Proliferation Ki-67
Ksp	Kidney-Specific Protein
Maff	MAF BZIP Transcription Factor F
mTORC1	Mechanistic Target of Rapamycin Complex 1
NF-κB	Nuclear Factor kappa-light-chain-enhancer of activated B cells
OD	Optical Density
P2A	Porcine teschovirus-1 2A (self-cleaving peptide)
Pax8	Paired Box 8
PBS	Phosphate-Buffered Saline
PBAF	Polybromo-Associated BRG1-Associated Factor

PB1	Polybromo 1
PBRM1	Polybromo 1 (protein)
PBRM1	Polybromo 1 (human gene)
Pbrm1	Polybromo 1 (mouse gene)
Pgk	Phosphoglycerate Kinase
PHD	Prolyl Hydroxylase Domain
PI3K	Phosphoinositide 3-Kinase
pVHL	Von Hippel-Lindau (protein)
RTE	Renal Tubular Epithelium
RNA	Ribonucleic Acid
RNA-seq	Ribonucleic Acid sequencing
SETD2	SET Domain Containing 2
Sglt2	Sodium-Glucose Cotransporter 2 (mouse gene)
SMARCA4	SWI/SNF Related, Matrix Associated, Actin Dependent Regulator of Chromatin, Subfamily A, Member 4
STAT3	Signal Transducer and Activator of Transcription 3
SWI/SNF	SWItch/Sucrose Non-Fermentable
TBS-T	Tris buffered Saline with Tween-20
TRACERx	Tracking Cancer Evolution through Therapy (Rx)
Vcam1	Vascular Cell Adhesion Molecule 1 (mouse gene)
VHL	Von Hippel-Lindau (human gene)
Vhl	Von Hippel-Lindau (mouse gene)

1. Introduction

1.1 Clear cell renal cell carcinoma

Clear cell renal cell carcinoma (ccRCC) is the most common form of kidney cancer accounting for about 75% of all cases (1). ccRCC tumour cells are characterised by clear cytoplasm and distinct cell borders visible in Haematoxylin & Eosin staining (Figure 1.1A). These features are attributable to the cancer cells' high lipid and glycogen content and are the reason for the name clear cell renal cell carcinoma (2,3). Renal tubular epithelial cells, particularly proximal tubular epithelial cells, were identified as the cell of origin of ccRCC. These cells reside in the renal cortex, one of four layers into which the kidney can be divided: Cortex, outer medulla, inner medulla and papilla (Figure 1.1B).

A striking feature of ccRCC is the long latency between truncal, genetic and mutational events and the actual formation of a tumour. The first event in the evolution of this type of renal cancer is the near-universal loss of chromosome arms 3p which can occur as early as childhood or adolescence (Figure 1.2A) (4). Chromosome arm 3p harbours several tumour suppressor genes which are in turn rendered haploinsufficient. During the course of years or decades, the other chromosomal copies of these haploinsufficient tumour suppressor genes will acquire additional inactivating mutations (5). The first and truncal inactivating mutation in ccRCC leads to the loss of the Von Hippel-Lindau (*VHL*) tumour suppressor gene. This loss of the *VHL* tumour suppressor gene is a sporadic event in 95-98% of all ccRCC cases. In 2-5% of ccRCC cases, patients suffer from 'VHL disease', which is characterised by *VHL* germline mutations that are either inherited or occur *de novo* (6,7). The sporadic inactivation of the *VHL* gene is caused by allelic deletion in ~60-70%, point mutation in ~20-30% and hypermethylation in ~10-20% of all ccRCC tumour samples and can occur 5-20 years after the initial loss of

chromosome arm 3p (5,8–10). In addition to this truncal mutation, which is insufficient to cause tumour formation by itself, other tumour suppressor genes need to be inactivated for tumorigenesis to occur (11–14). The most common secondary genes found to be mutated in ccRCC are Polybromo-1 (*PBRM1)* in 40% (15), BRCA1 associated protein-1 (*BAP1*) in 10% (16) and SET domain containing 2 (*SETD2*) in 10% (17) of all cases (Figure 1.2B).

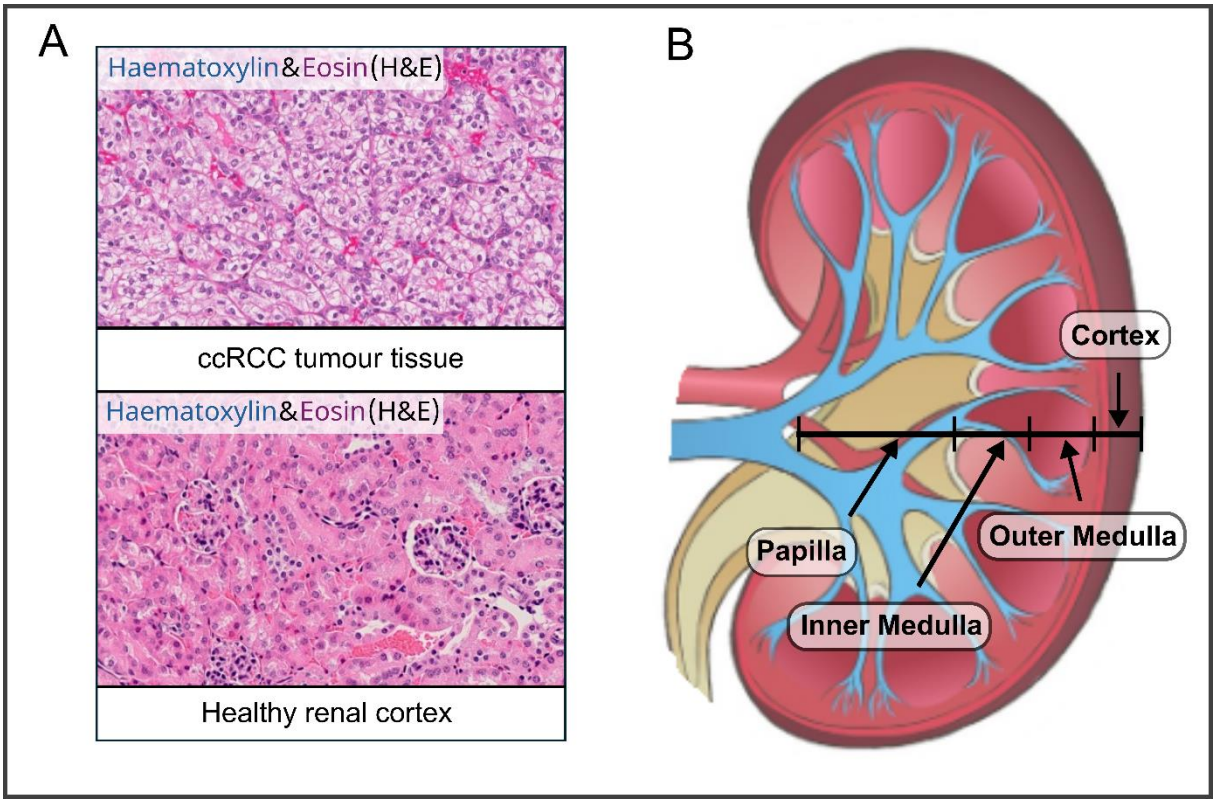

Figure 1.1: Histology of ccRCC tissue compared to the healthy renal cortex and four layers of the kidney: (A) *Haematoxylin & Eosin staining of ccRCC tumour tissue showing the distinct clear cell phenotype cause by lipid and glycogen accumulation in the cytoplasm. Below, the Haematoxylin & Eosin staining of a healthy renal cortex.* ***(B)*** *The general division of the kidney into four layers: Cortex, outer medulla, inner medulla and papilla. (H&E staining of ccRCC adapted from Mubarak et al., 2024)*

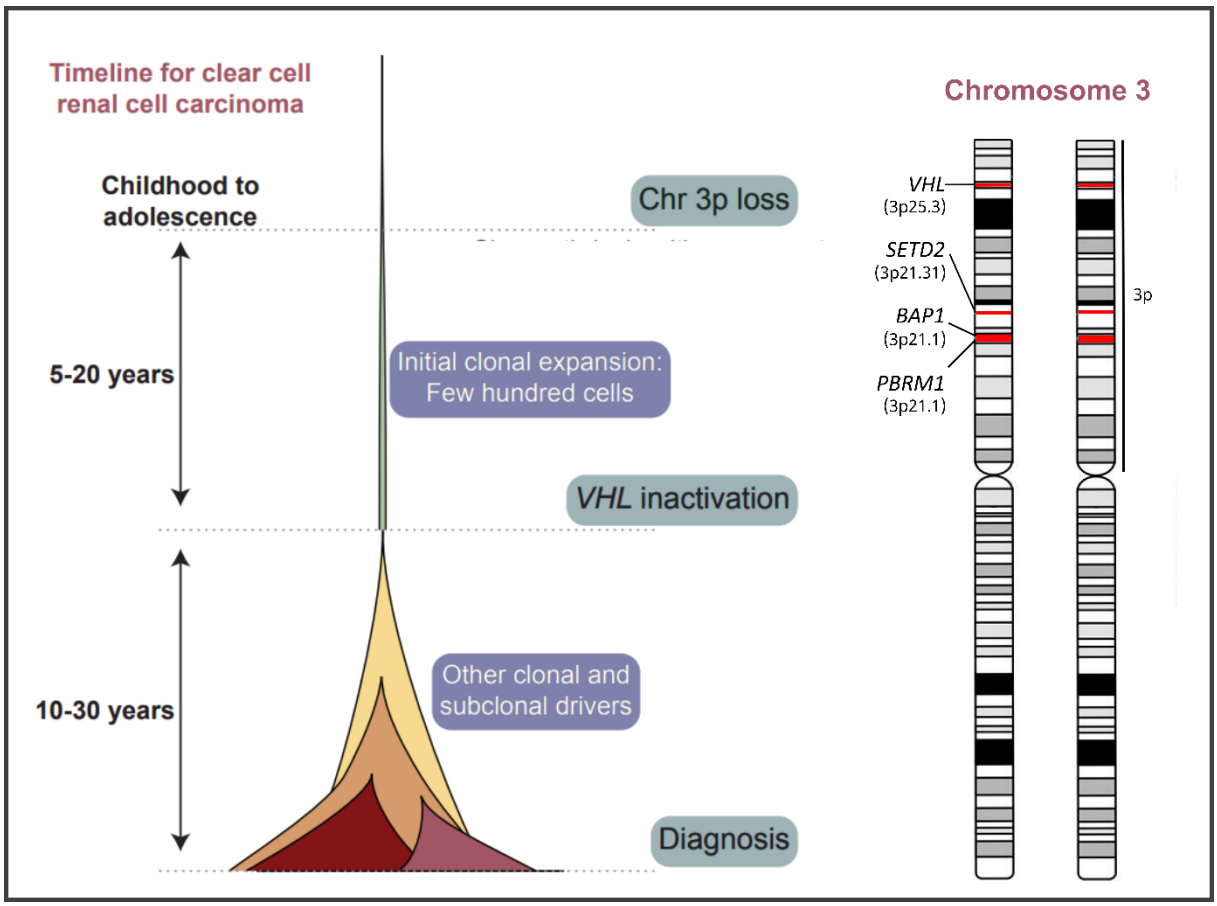

Figure 1.2: Timeline of clear cell renal cell carcinoma (ccRCC) progression and chromosome 3p: *Left: The timeline for ccRCC progression displaying the long latency of ccRCC and the subsequent steps needed for ccRCC to occur according to TRACERx renal (Mitchell et al, 2018). Right: Chromosome 3p and the three most commonly tumour suppressor genes mutated in ccRCC: VHL, PBRM1, BAP1 and SETD2 (Adapted from Mitchell et al., 2018)*

1.1.1 Von Hippel-Lindau: a tumour suppressor in ccRCC

The Von Hippel-Lindau (*VHL*) gene is the most common tumour suppressor gene found to be mutated in ccRCC (8,15). *VHL* plays a crucial role in cellular oxygen sensing and is integral to various regulatory pathways that maintain cellular homeostasis. It encodes for pVHL, whose best-described function is being part of an E3 ubiquitin ligase complex responsible for targeting hypoxia-inducible factors (HIFs) for ubiquitination and proteasomal degradation under normoxic conditions (18,19). Here, pVHL functions as a substrate recognition subunit, binding HIF1A and HIF2A which are hydroxylated in an oxygen-dependent manner (20,21). This binding and the subsequent ubiquitination of HIF1A and HIF2A leads to the degradation of these two HIF isoforms. Under hypoxic conditions, HIF1A and HIF2A are not hydroxylated due to the lack of oxygen, therefore they will not be bound by pVHL and are not ubiquitinated for degradation. This leads to the stabilisation of HIF1A and HIF2A, which in turn can for heterodimers with HIF1B and translocate to the nucleus (22). In the nucleus, these heterodimers exhibit their function as transcription factors for various genes, binding to hypoxia-responsive elements in gene promoters or promoter-distant enhancers (23). Similarly, loss of pVHL leads to the same stabilisation of HIF1A and HIF2A as under hypoxic conditions, leading to a condition called pseudo-hypoxia.

The stabilisation of HIF1A and HIF2A caused by the loss of VHL leads to inappropriate activation of downstream target genes that would normally be activated under hypoxic conditions only. Thus, VHL loss and subsequent HIF stabilisation contribute directly to activating protumorigenic pathways by regulating the expression of a multitude of target genes (24). Of note is that the loss of VHL alone or the subsequent stabilization of HIF1A/HIF2A does not lead to tumour development in mouse kidneys (25–27).

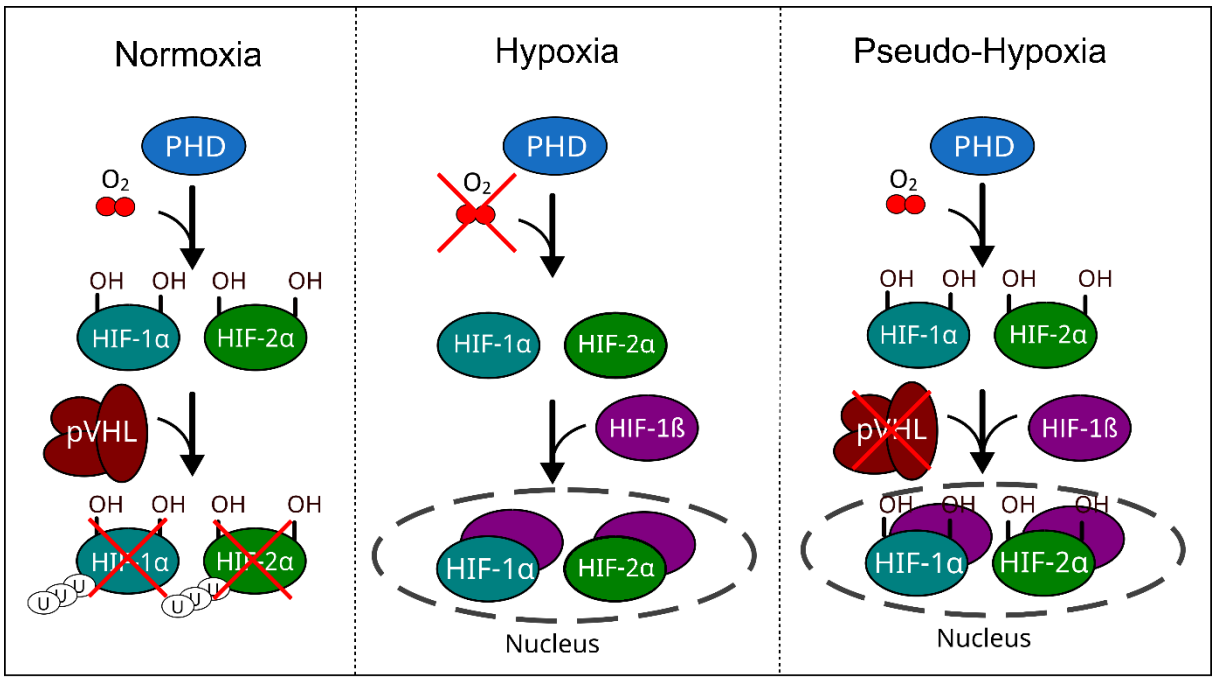

Figure 1.3: Mechanism of cellular oxygen sensing and the role of pVHL and HIF: Left: *Under normoxic conditions hydroxylated HIFs are recognized by pVHL and ubiquitinated for proteasomal degradation.* ***Middle:*** *Under hypoxic conditions HIFs are not hydroxylated due to the lack of oxygen, form heterodimers with HIF1ß, and translocate to the nucleus to act as transcription factors.* ***Right:*** *Pseudo-hypoxic conditions are caused by the absence of pVHL which prevents the degradation of hydroxylated HIFs which therefore can form heterodimers with HIF1ß and translocate to the nucleus to act as transcription factors.*

1.1.2 Polybromo 1: A tumour suppressor gene in ccRCC

PBRM1 is a tumour suppressor gene that plays a pivotal role in chromatin remodelling, transcriptional regulation, and maintenance of genomic integrity (28). The PBRM1 protein is also known as PB1 (Polybromo1) and BAF180 (BRG1-associated factor 180) and is one of the unique subunits of the SWI/SNF (SWItch/Sucrose Non-Fermentable) chromatin remodelling complex subtype PBAF (Polybromo-associated BRG1-associated factor) (29). PBAF is a large 1.2 MDa complex consistent of a motor subunit SMARCA4 and 11 auxiliary subunits including PBRM1, ARID2 and BRD7. This SWI/SNF complex subtype is crucial for modulating the accessibility of chromatin to the transcriptional machinery, thereby influencing gene expression (30). In recent years, *PBRM1* has gained significant attention due to its frequent mutation in various cancers, particularly in ccRCC, where it is the second most commonly mutated gene after *VHL* (8,31).

The PBRM1 protein is comprised of six bromodomains, two bromo adjacent homology (BAH) domains and a high mobility group (HMG) domain. Bromodomains are so-called readers of acetylation marks such as, but not limited to, acetylated lysine groups on histone tails whereas BAH domains were shown to bind methylated and unmodified amino acid residues. The HMG domain is a DNA-binding motive. The composition of PBRM1 suggests its function in protein-protein interaction, DNA binding, and protein recruitment. Hence this is reflected in the proposed mechanisms of how *PBRM1* exhibits its function as a tumour suppressor gene and its role in the chromatin remodelling complex PBAF.

First, the inactivation of *PBRM1* disrupts chromatin remodelling, leading to aberrant gene expression patterns that favour tumorigenesis. It has been demonstrated that the *PBRM1* gene product acts as a target recognition subunit of the chromatin remodelling complex PBAF.

In the absence of PBRM1, the PBAF complex is redirected from promoter-proximal regions to distal enhancers which contain NF-κB motifs. This alteration of PBAF specificity causes the heightening of NF-κB activity and the expression of protumorigenic NF-κB target genes (32). Second, PBRM1 has been shown to be involved in maintaining chromosome stability during mitosis by recruiting the PBAF complex to the mitotic spindle. Here PBRM1 is binding to the α-TubK40me3 mark on microtubules *via* its BAH domains and tethering the chromatin to the cytoskeleton by binding acetylated histone tails *via* its bromodomains. *In vitro*, the absence of PBRM1 has caused increased genome instability resulting in the formation of micronuclei, lagging chromosomes, multipolar spindles, and chromosome bridges (33). Third, in human cancer samples PBRM1 expression levels have been found to correlate with the expression of p21. Here PBRM1 acts as an acylation reader protein, binding to the acetylated lysine 382 (K382Ac) of p53 *via* bromodomain 4 and recruiting p53 to its target gene promotors. In this setting PBRM1 will bind acetylated histone tails, support the expression of p53 target genes like *CDKN1A* (p21), and hence suppress tumour growth (34,35).

1.2 Mouse models to study *Vhl* and *Pbrm1* loss in ccRCC

While ccRCC evolution is characterised by the near-universal, biallelic loss of *VHL* as the truncal genomic event, this alone has been shown insufficient for tumorigenesis (5). For ccRCC to form loss of an additional tumour suppressor gene like *PBRM1* is required (8,36). Although *VHL* and *PBRM1* are well-studied on their own and potential mechanisms have been uncovered *in vitro* that could potentially contribute to tumorigenesis, little is known about how exactly the loss of *VHL* and *PBRM1* interact *in vivo* to cause ccRCC (5). In order to study the impact of *VHL*, *PBRM1*, or concomitant *VHL/PBRM1* loss, several knock-out mouse models have been created aiming to reproduce the genetic events in human ccRCC.

1.2.1 Previous mouse models used to study *Vhl* and *Pbrm1* loss in ccRCC

To date, three different mouse models have been published studying the effects of concomitant *Vhl/Pbrm1* loss in the renal tubular epithelium (RTE). Each of these utilises a different variation of the Cre recombinase-mediated biallelic inactivation of *Vhl* and/or *Pbrm1*.

First, Nargund *et al* (11) utilised the kidney-specific *Cadherin* 16 promoter (*Ksp*) to drive the expression of the Cre recombinase. The expression under this promotor is initiated at embryonic day 14.5 targeting Cre expression to epithelial cells of the developing kidney and additionally to the genitourinary tract. Further, this promotor will continue expressing in developed renal tubular epithelial cells. In combination with biallelic, loxP flanked (floxed (*fl*)) *Vhl* and *Pbrm1* gene constructs, $Vhl^{fl/fl}$; Ksp-*Cre*, $Pbrm1^{fl/fl}$; ^{Ksp}-*Cre*, and $Vhl^{fl/fl}$; $Pbrm1^{fl/fl}$ *Ksp-Cre* mouse lines were created to model *Vhl*, *Pbrm1* and concomitant *Vhl/Pbrm1* loss. The Vhl^{fl}

gene has two parallel *loxP* sites flanking the promoter and exon 1 which leads to the excision of these parts of the *Vhl* gene rendering the gene non-functional (37). This Vhl^{fl} ($Vhl^{jae.fl}$) allele was used in all mouse models reviewed here. The $Pbrm1^{fl}$ gene contains two parallel *loxP* sites flanking exon 11 of *Pbrm1* and Cre-mediated excision introduces a frameshift, rendering the product of this gene non-functional (38). The deletion of these genes was confirmed by genomic polymerase chain reaction (PCR) genotyping.

Here, biallelic *Vhl* or *Pbrm1* loss alone was shown to be insufficient to cause kidney cancer. In contrast, $Vhl^{fl/fl}$*; Pbrm1*$^{fl/fl}$*; Ksp-Cre* mice developed transplantable, multifocal, clear-cell kidney cancer after 8-17 months. Further, gene expression analysis of RNA extracted from the renal cortex of 12-week-old $Vhl^{fl/fl}$*; Ksp-Cre*, *Pbrm1*$^{fl/fl}$*; Ksp-Cre*, and $Vhl^{fl/fl}$*; Pbrm1*$^{fl/fl}$*; Ksp-Cre* mice revealed distinct gene expression patterns. The authors have found that upon concomitant loss of *Vhl* and *Pbrm1* genes involved in the JAK-STAT pathway, the HIF1A pathway, Focal Adhesion/PI3K, and Toxoplasmosis were significantly overrepresented among upregulated genes. Further, they could show that genes involved in Oxidative Phosphorylation were overrepresented amongst downregulated genes. Here it was emphasized that loss of *Pbrm1* is amplifying the expression of HIF1A target genes in *Vhl*-null cells. In addition, gene expression analysis of full ccRCC tumours found in aged $Vhl^{fl/fl}$*; Pbrm1*$^{fl/fl}$*; Ksp-Cre* mice was conducted and significant activation of the mTOR pathway was found.

Second, in a comparable study, Gu *et al* (13) created a similar mouse model using different promoters to drive Cre recombinase expression. They compared *Pax8*, which is a frequently overexpressed transcription factor in ccRCC to *Sglt2* and *Villin* which are driving expression of Cre in proximal convoluted tubules. *Sglt2* was chosen since it is expressed in proximal tubular cells specifically in the brush border membrane of the S1 segments (39). *Villin* was used since it is expressed in cells that develop brush borders such as renal proximal tubular cells (40). In mice, used for this study *Pax8-Cre*, *Sglt2-Cre* and *Villin-Cre* were expressed

constitutively. The *Vhl*$^{fl/fl}$ and *Pbrm1*$^{fl/fl}$ alleles used in this model were the same as those described above, used by Nargund *et al*.

They reported that only concomitant loss of *Vhl* and *Pbrm1* in cells expressing *Pax8* caused ccRCC-like tumours, confirming that only the biallelic loss of both tumour suppressor genes induces tumorigenesis. Further, the lack of tumour formation when Cre recombinase expression is driven by *Sglt2* and *Villin* has led Gu *et al.* to challenge the notion that ccRCC arises from proximal convoluted tubules. In contrast, they suggest that ccRCC arises from parietal cells of the bowman capsule which are derived from the *Pax8* lineage and not from *Sglt2*- and *Villin*-expressing cells. This is further supported by histological analysis of kidneys from *Vhl*$^{fl/fl}$*; Pbrm1*$^{fl/fl}$*; Pax8-Cre* mice showing dilated bowman capsule structure and nuclear enlargement with a variable cytoplasmic clearing in the lining parietal epithelial cells of the bowman capsule. Additionally, they showed that the formation of high-grade Pbrm1-deficient tumours is induced by the activation of mTORC1.

The third mouse model developed by Espana-Augusti *et al*. (12) utilized the same Pax8 promotor to drive the expression of an inducible *CreER*^{T2} transgene in the renal tubular epithelium (41). In contrast to the previously mentioned studies, concomitant *Vhl/Pbrm1* loss was induced by injecting 5x 2mg tamoxifen 1 month after the mice were born. This inducible inactivation allowed for targeting the fully developed renal tubular epithelium. In agreement with both above-mentioned studies it was found that only concomitant loss of *Vhl* and *Pbrm1* but not loss of *Vhl* or *Pbrm1* alone leads to the formation of ccRCC-like tumours. Therefore, finding multifocal neoplastic ccRCC-like tumours alongside benign cysts 20 months after tamoxifen-induced *Vhl/Pbrm1*-loss brought evidence that ccRCC can arise from the fully developed renal tubular epithelium. The *Vhl* allele used in this model in the same *Vhl*^{fl} allele as described above. The *Pbrm1*^{fl} allele used in this study is different to the previously described floxed *Pbrm1* since it introduces the frameshift at exon 4 instead of exon 11.

Taken together all three studies have shown that only concomitant loss of *Vhl* and *Pbrm1* but not loss of either tumour suppressor gene by itself can induce the formation of ccRCC in mice. Further, they have identified *Pax8* as a suitable driver of *Cre*-mediated *Vhl/Pbrm1* loss to cause ccRCC-like tumours in the renal tubular epithelium.

1.2.2 Oncogenic cell tagging to study *Vhl* loss in renal tubular epithelium *in vivo*

However, these studies did not provide insight into how the loss of these tumour-suppressor genes contributes to cancer initiation. Further, it remains elusive what cell-type specific and temporal effects loss of *Vhl* and *Pbrm1* has in the renal tubular epithelial cells in its native context. This is partly due to the inability to visualise and extract cells that have lost these tumour suppressor genes before they undergo morphological alterations.

To overcome these limitations, Kurlekar & Lima *et al*. (14) have developed a mouse model which couples the inducible inactivation of *Vhl* in the renal tubular epithelium to the expression of a tdTomato fluorescent reported gene. To achieve this, an allele ($Vhl^{pjr.fl}$) was designed that allows for the Cre-mediated knock-in of the tdTomato reporter and the excision of exons 2 and 3 of *Vhl* in two steps (Figure 1.4). First, a Cre-mediated, reversible inversion between two antiparallel *loxP* sites places the tdTomato reporter gene in frame, downstream of *Vhl*. This inversion places two *lox2272* sites parallel to each other, flanking exon 2 and 3 of *Vhl* enabling the Cre-mediated, irreversible excision of these two exons ($Vhl^{pjr.inrec}$). This will place the tdTomato reporter gene in frame with the native *Vhl* promoter and exon 1 of *Vhl* ($Vhl^{pjr.KO}$). Cotranscription of tdTomato and *Vhl* exon 1 is enabled by a splice-acceptor (SA) and their translation is uncoupled by a porcine teschovirus 2A sequence (P2A). The resulting *Vhl* fragment consisting of only exon 1 lacks residues necessary for the interaction with substrates

and binding partners hence rendering it nonfunctional (20,42). Therefore, this allele links the inactivation of *Vhl* with the expression of the tdTomato reporter gene.

This allele is coupled with either a wild-type allele (Vhl^{wt}) or a constitutively knocked-out *Vhl* allele ($Vhl^{jae.KO}$) (37). These combinations in turn enable the inducible monoallelic ($Vhl^{wt/pjr.fl}$) or biallelic ($Vhl^{jae.KO/pjr.fl}$) inactivation of the *Vhl* gene. To target the renal tubular epithelium specifically for *Vhl* inactivation, a tamoxifen-inducible *Pax8*-driven $CreER^{T2}$ allele (*Pax8-*$CreER^{T2}$) was used (41). As confirmed by immunoblotting, only the biallelic loss of *Vhl* leads to the stabilisation of HIF1A and HIF2A and in turn, monoallelic loss of *Vhl* is insufficient to stabilise HIF1A and HIF2A (Figure 1.5A). Since the goal of this study was to primarily investigate biallelic loss of *Vhl* as it occurs in ccRCC oncogenesis, monoallelic *Vhl*-loss ($Vhl^{wt/pjr.fl}$) was used as a control (ConKO) to compare biallelic *Vhl*-loss ($Vhl^{jae.KO/pjr.fl}$) (VKO) to. Of note is that previous mouse models inactivated both copies of *Vhl* simultaneously in order to recreate *Vhl*-null cells. In contrast, this model relies on one constitutively inactivated *Vhl* allele which is inherited. The genetic outcome, that is the loss of *Vhl,* is the same in both cases but the order in which the loss of the individual alleles occurs is different. Compared to previous models the inheritance of an inactive *Vhl* allele and the inactivation of the second allele later in life represents the start of ccRCC onset as found in some VHL disease patients. The simultaneous inactivation of both genes at the same time is very unlikely in nature.

A major advantage of this mouse model is that coupling *Vhl*-loss to the expression of the tdTomato fluorescent reporter gene enables the visualisation of cells that have lost *Vhl* by immunostaining, regardless of whether they have changed morphology (Figure 1.5B). Because the fluorescence of tdTomato was of low intensity in fixed tissues, immunostaining using an antibody for the fluorescent reporter protein was used to enhance detection. In addition to that, the inducible *Pax8-*$CreER^{T2}$ allows for the spatiotemporal control of *Vhl* inactivation. Thus, this model was used to study the long-term survival of recombined cells in the renal tubular

epithelium. To do so kidney sections of ConKO and VKO mice, immunostained for tdTomato, have been analysed at an early (1-3 weeks) and late (>4 months) time point after tamoxifen-induced recombination. Comparing the number of tdTomato-positive cells at early and late time points, with respect to their distribution in four regions of the kidney (cortex, outer medulla, inner medulla, and papilla), revealed that biallelic *Vhl*-loss leads to increased survival of cells in the cortex and outer medulla. Importantly, this survival advantage was insufficient for tumour formation and no morphological abnormalities were reported by Kurlekar & Lima *et al* (14).

Another advantage of this model is that the expression of tdTomato upon *Vhl*-loss not only enables the visualisation of recombined cells but also allows for the extraction of tdTomato-positive cells from kidney tissue. This was done by dissociating fresh kidneys and conducting fluorescent-activated cell sorting (FACS) to obtain single-cell suspensions for tdTomato-positive and tdTomato-negative cells. Subsequent single-cell transcriptome analysis revealed cell type-specific and time-dependant changes in response to biallelic loss of *Vhl*.

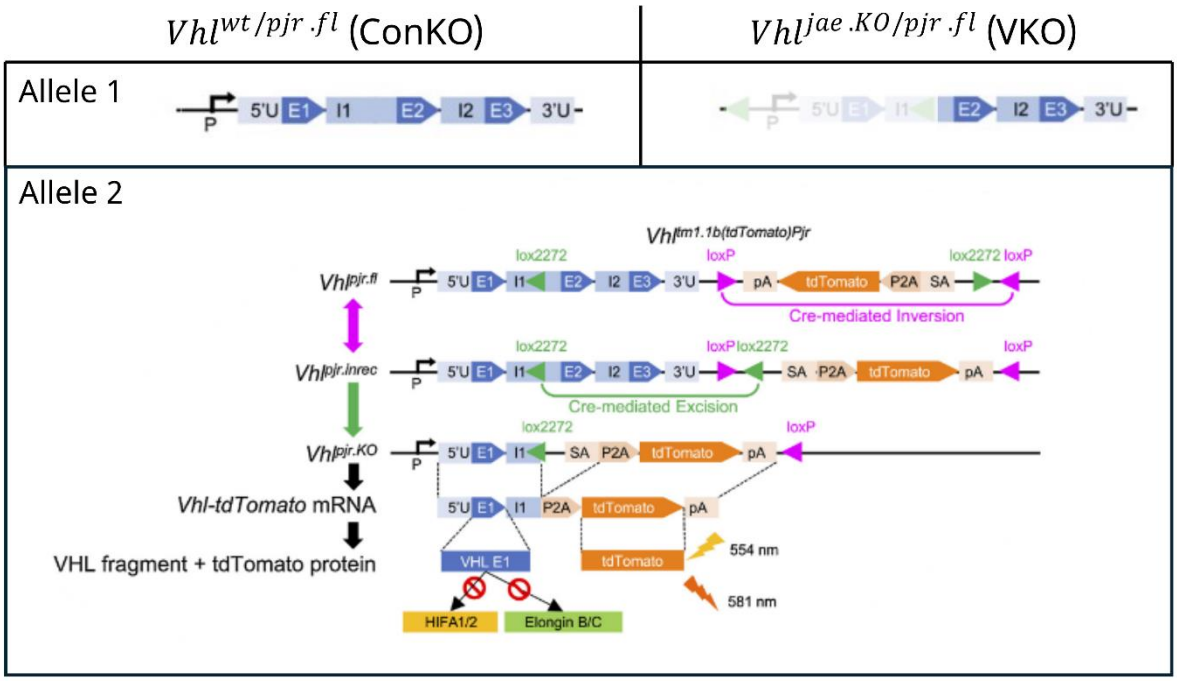

Figure 1.4: Architecture and combination of Vhl alleles to induce monoallelic (ConKO) or biallelic (VKO) loss of the Vhl gene: *The first allele is variable in ConKO and VKO to cause monoallelic or biallelic inactivation of the Vhl gene respectively. Therefore, the first Vhl allele of ConKO is a wild-type (wt) allele and the first Vhl allele of VKO is a constitutively inactivated VHL allele which has lost its promoter and exon 1 (jae.KO). The second Vhl allele is the same in both genotypes and couples Vhl inactivation to the expression of a tdTomato reporter gene via Cre-mediated inversion and excision. (Adapted from Kurlekar and Lima et al., 2024)*

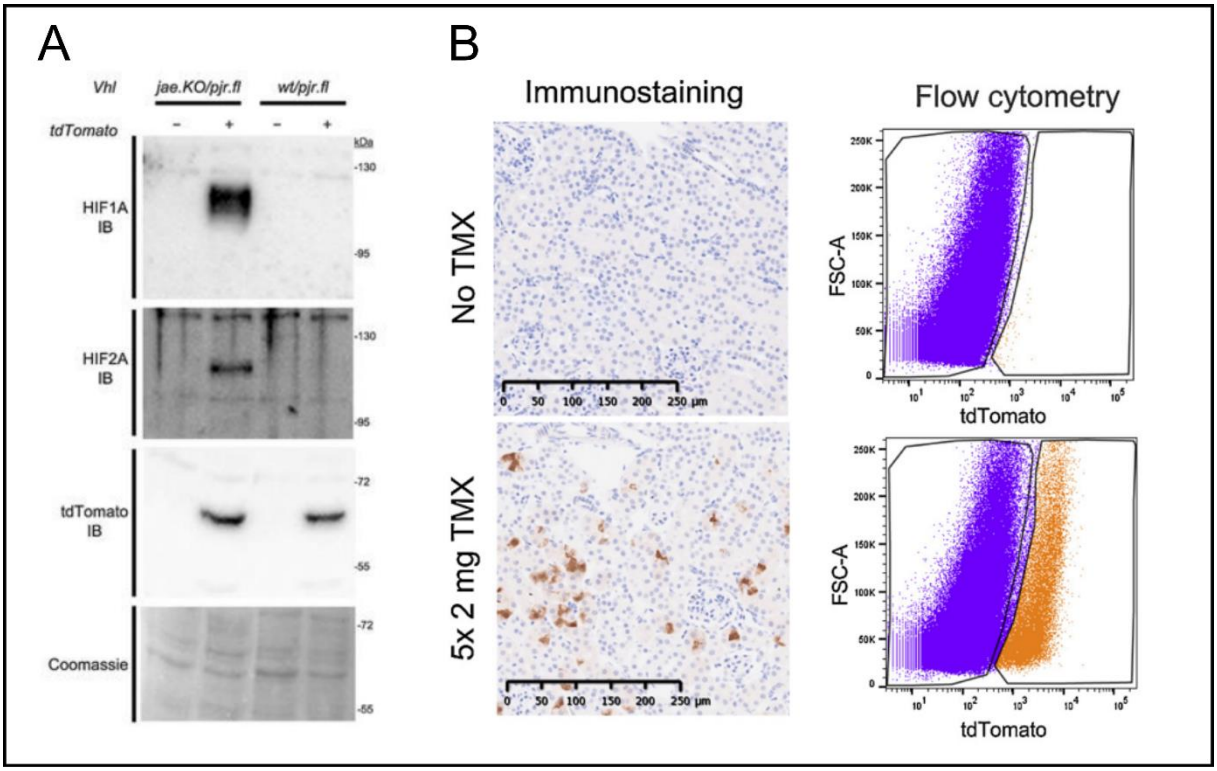

Figure 1.5: Confirmation of monoallelic and biallelic Vhl inactivation coupled to tdTomato expression and utilization of the model via immunostaining and flow cytometry: (A) *Immunoblots for HIF1A, HIF2A and tdTomato in flow cytometry sorted tdTomato-positive and tdTomato-negative cells from dissociated kidneys harvested from* $Vhl^{jae.KO/pjr.fl}$ *or* $Vhl^{wt/pjr.fl}$ *Pax8-*$CreER^{T2}$ *mice which have been given 5x 2 mg tamoxifen. (**B) Left:** Immunohistochemistry (IHC) for tdTomato, counterstained with haematoxylin in kidney sections of* $Vhl^{wt/pjr.fl}$*; Pax8-CreERT2 mice which have been untreated (top) or have been given 5 × 2 mg tamoxifen (bottom) at ×20 Magnification. **Right:** Fluorescent activated cell sorting (FACS) was conducted on dissociated kidneys of the same mice as used for IHC. (Adapted from Kurlekar and Lima et al., 2024)*

1.2.3 Expansion of the oncogenic cell tagging model for the *Pbrm1* gene

The oncogenic cell tagging model by Kurlekar & Lima *et al*. (14) was initially developed to study cell type-specific and time-dependent effects of *Vhl* loss in renal tubular epithelial cells. Due to the ability to extract and characterise cells in advance of morphological abnormality, this system poses a new opportunity to study the concomitant loss of *Vhl* and other tumour suppressor genes essential for tumorigenesis. Therefore, this mouse model was expanded to include the loss of *Pbrm1,* the second most commonly lost tumour suppressor gene in ccRCC. To achieve this, the monoallelic ($Vhl^{wt/pjr.fl}$) and biallelic ($Vhl^{jae.KO/pjr.fl}$) loss of *Vhl* was coupled to homozygous conditional *Pbrm1* alleles (12). These alleles contain two parallel *loxP* sites flanking exon 4 of the *Pbrm1* gene (Figure 1.6A). These *loxP* sites allow for the Cre-mediated excision of exon 4 which leads to a frameshift in the 24 downstream exons of *Pbrm1* rendering the gene products of these recombined alleles nonfunctional. The addition of homozygous conditional $Pbrm1^{fl/fl}$ alleles to the previous model for conditional mono- and biallelic *Vhl* loss driven by *Pax8-CreER*^{T2} yielded mice that upon tamoxifen dosing lose both genes in the same cell in parts of the renal tubular epithelium and express the tdTomato reporter gene. This was confirmed *via* immunostaining for *Pbrm1* showing the lack of *Pbrm1* in $Vhl^{jae.KO/pjr.fl}$, $Pbrm1^{fl/fl}$, *Pax8-CreER*^{T2} (VPKO) cells after recombination in contrast to $Vhl^{jae.KO/pjr.fl}$, *Pax8-CreER*^{T2} (VKO) cells (Figure 1.6B). Further, it was confirmed that tdTomato expression in VPKO cells was coupled to biallelic *Pbrm1* loss by immunoblotting using FAC-sorted cells (Figure 1.6C).

The combination of biallelic *Pbrm1* loss with biallelic *Vhl* loss leads to conditions in renal tubular epithelial cells similar to those found in early ccRCC progression. These mice, termed VPKO, allow for visualising and extracting *Vhl/Pbrm1*-null renal tubular epithelial cells before they undergo any form of morphological alteration. Early analysis of these cells was not

possible previously. Further mice combining the conditional monoallelic loss of *Vhl* with biallelic loss of *Pbrm1* in the renal tubular epithelium, termed ConPKO, act as a control for the specific effects of *Pbrm1* loss on a *Vhl* haploinsufficient background.

Taken together, this novel mouse model opens new ways of studying concomitant *Vhl/Pbrm1* loss in the renal tubular epithelium and can potentially give insight into the early mechanisms of ccRCC tumorigenesis.

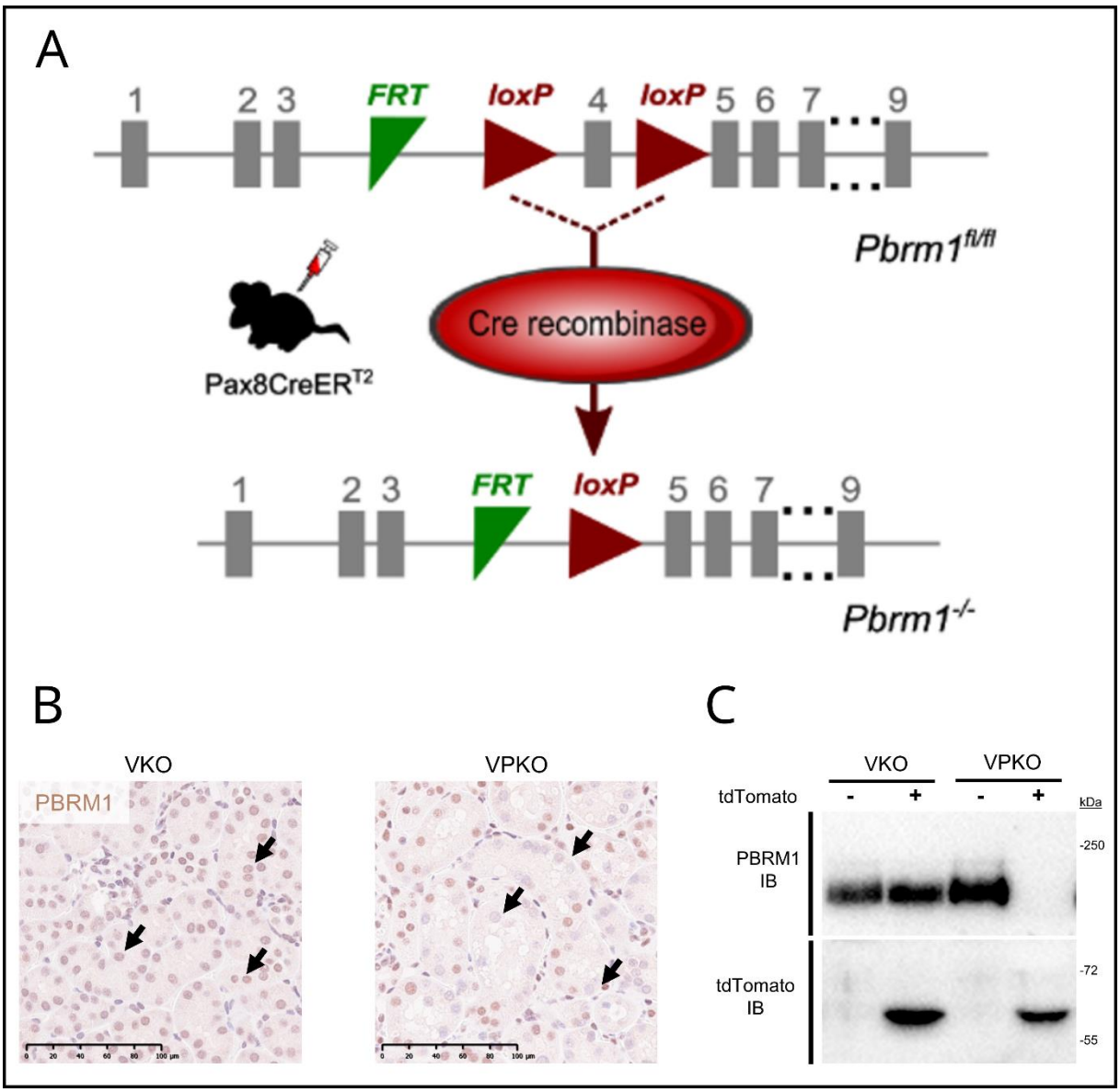

Figure 1.6: Architecture of the Pbrm1 allele to induce biallelic Pbrm1 loss and confirmation of Pbrm1 loss: *(A) The Pbrm1 gene utilized to induce biallelic Pbrm1 loss displaying the parallel loxP sites flanking exon 4. Cre-mediated excision of exon 4 introduces a frame shift in the exons downstream of exon 4 rendering the gene product non-functional. (Adapted from Espana-Augusti et al., 2017)* ***(B)*** *Representative immunohistochemistry staining for PBRM1 of kidney section from $Vhl^{jae.KO/pjr.fl}$, Pax8-$CreER^{T2}$ (VKO) and $Vhl^{jae.KO/pjr.fl}$, $Pbrm1^{fl/fl}$, Pax8-$CreER^{T2}$ (VPKO) mice treated with 5 x 2 mg tamoxifen. The black arrows on the left indicate nuclei stained positive for PBRM1. The black arrows on the right indicate nuclei stained negative for PBRM1. (IHC performed by Dr Joanna Lima)* ***(C)*** *Immunoblots for PBRM1 and tdTomato of FAC sorted tdTomato-negative (-) and tdTomato-positive (+) cells form $Vhl^{jae.KO/pjr.fl}$, Pax8-$CreER^{T2}$ (VKO) and $Vhl^{jae.KO/pjr.fl}$, $Pbrm1^{fl/fl}$, Pax8-$CreER^{T2}$ (VPKO) mice treated with 5 x 2 mg tamoxifen. (Architecture of $Pbrm1^{fl/fl}$ adapted from Espana-Augusti et al., 2017, Immunostaining performed by Dr. Joanna D.C.C. Lima, Immunobloting performed by Dr. Norma Masson)*

1.3 Aims and Objectives

So far, several studies have investigated the role of concomitant loss of *Vhl* and *Pbrm1* in the development of clear cell renal cell carcinoma (ccRCC). They all have found that only the concomitant loss of *Vhl* and *Pbrm1* in the renal tubular epithelium but not the loss of either tumour suppressor on its own leads to the formation of ccRCC. Several mechanisms were proposed for how the loss of these tumour suppressor genes interact and contribute to tumorigenesis but the initiating events of ccRCC evolution remain elusive. This is partly owed to the previous inability to visualise and extract renal tubular epithelial cells that have lost *Vhl* and *Pbrm1* in advance of morphological abnormality. To overcome this limitation a mouse model is used which couples concomitant *Vhl/Pbrm1* loss in the renal tubular epithelium with the expression of a tdTomato reporter gene. In the following thesis, this mouse model will be used to test the hypothesis that induced loss of *Vhl* and *Pbrm1* in the renal tubular epithelium causes dysplasia and oncogenesis. Further, this study aims to investigate the synergistic effects of *Vhl* and *Pbrm1* loss with respect to cell survival and distribution of cells in the renal cortex over time and to explore the hypothesis that *Pbrm1* loss imposes transcriptional changes on *Vhl*-null cells which contributes to early ccRCC evolution.

The specific aims of this study are to:

- Study the effects *Pbrm1* loss has on the observed expansion of *Vhl*-null, tubular epithelial cells in the renal cortex over time
- Reproduce the previously reported oncogenesis and dysplasia observed by others in renal tubular epithelial cells after the concomitant loss of *Vhl* and *Pbrm1*.
- Quantify early histological changes of tdTomato-positive cells in the renal cortex indicating an early onset of cancer development

- Investigate transcriptomic changes imposed by *Pbrm1* loss on *Vhl*-null, renal tubular epithelial cells as a potential cause for ccRCC evolution

2. Materials and Methods

2.1 Mice

Mice were housed in individually ventilated cages under a 13-hour light/11-hour dark cycle, with *ad libitum* access to food and water. *Vhl*$^{\text{tm1.1b(tdTomato)Pjr}}$ (*Vhl*$^{\text{wt/pjr.fl}}$) mice were generated using goGermline technology on a C57BL/6J background and were commissioned from Ozgene, Australia. To produce mice with a constitutive knock-out of the *Vhl*$^{\text{tm1jae}}$ allele (*Vhl*$^{jae.KO}$), *Vhl*$^{\text{tm1jae}}$ (*Vhl*$^{wt/jae.fl}$) mice (RRID:IMSR_JAX:012933) were obtained from The Jackson Laboratory and subsequently crossed with *Tg(Pgk1-cre)1Lni* (*Pgk1-Cre*) mice (RRID:IMSR_JAX:020811) (43). From the European Mouse Mutant Archive (EMMA) mice were sourced which carry the tamoxifen-inducible Cre-recombinase allele under the *Pax8* promoter (*Tg(Pax8-cre/ER*^{T2}*)CAmat*; termed *Pax8-CreER*^{T2}) (RRID:IMSR_HAR:9175) (41). Also on a C57BL/6J background, mice carrying a *Pbrm1* allele which can be conditionally inactivated (*Pbrm1*$^{tm1c(EUCOMM)Wtsi}$; termed *Pbrm1*^{fl}) (RRID:IMSR_JAX:031875)(12) were obtained from The Jackson Laboratory. *Vhl*$^{wt/pjr.fl}$*; Pax8-CreER*^{T2} mice (ConKO), *Vhl*$^{jae.KO/pjr.fl}$*; Pax8-CreER*^{T2} mice (VKO), *Vhl*$^{wt/pjr.fl}$*; Pbrm1*$^{fl/fl}$*; Pax8-CreER*^{T2} mice (ConPKO) and *Vhl*$^{jae.KO/pjr.fl}$*; Pbrm1*$^{fl/fl}$*; Pax8-CreER*^{T2} mice (VPKO) were bred on a *C57BL/6J* background and used between 2-20 months of age (Table 2.1). To induce recombination, mice weighing ≥20 g were administered 2mg tamoxifen on five consecutive days *via* oral gavage using sterile disposable plastic feeding tubes (Instech, FTP-20-38). Here a tamoxifen solution was prepared by diluting a 25% (w/v) stock solution of tamoxifen (Sigma, T5648) in absolute ethanol (Sigma, 51976) to a final concentration of 20 mg/ml in corn oil (Sigma, C8267). To create a 2 mg/ml solution, the 20 mg/ml stock was diluted using a mixture of 10% ethanol in corn oil. It was observed that female mice reached 20 g at 10-14 weeks of age, while males reached this weight

at 6-8 weeks. Breeding, harvesting and upkeep of mice was perfomed by Dr. Julie Adam, Dr. Joanna D.C.C. Lima and Dr. Samvid Kurlekar.

Table 2.1: Overview of mouse genotypes used in this study: *Four distinct genotypes were used in this study and are referred to as ConKO, VKO, ConPKO, and VPKO. Each genotype carries a unique combination of two Von Hippel-Lindau (Vhl) gene alleles and two Polybromo-1 (Pbrm1) gene alleles. Additionally, each genotype is carrying an inducible Cre-ER^{T2} allele. Recombination is induced by administration of 5 x 2 mg tamoxifen.*

Name	**Genotype**	***Vhl***		***Pbrm1***
		Allele1	Allele 2	Both Alleles
ConKO	*Vhl$^{wt/pjr.fl}$; Pbrm1$^{wt/wt}$; Pax8-CreER^{T2}*	*Vhl^{wt}*	*Vhl$^{tm1.1b(tdTomato)Pjr}$ (Vhl$^{pjr.fl}$)*	*Pbrm1^{wt}*
VKO	*Vhl$^{jae.KO/pjr.fl}$, Pbrm1$^{wt/wt}$; Pax8-CreER^{T2}*	*Vhl$^{jae.KO}$ (Vhl^{tm1jae})*	*Vhl$^{tm1.1b(tdTomato)Pjr}$ (Vhl$^{pjr.fl}$)*	*Pbrm1^{wt}*
ConPKO	*Vhl$^{wt/pjr.fl}$, Pbrm1$^{fl/fl}$; Pax8-CreER^{T2}*	*Vhl^{wt}*	*Vhl$^{tm1.1b(tdTomato)Pjr}$ (Vhl$^{pjr.fl}$)*	*Pbrm1^{fl} (Pbrm1$^{tm1c(EUCOMM)Wtsi}$)*
VPKO	*Vhl$^{jae.KO/pjr.fl}$, Pbrm1$^{fl/fl}$; Pax8-CreER^{T2}*	*Vhl$^{jae.KO}$ (Vhl^{tm1jae})*	*Vhl$^{tm1.1b(tdTomato)Pjr}$ (Vhl$^{pjr.fl}$)*	*Pbrm1^{fl} (Pbrm1$^{tm1c(EUCOMM)Wtsi}$)*

2.2 Tissue Harvest and Fixation

The kidney of mice was harvested at two distinct time points to study the immediate and long-term effects of their respective knock-outs. Here, the early time point is defined as 1-3 weeks and the late time point as >4 months after the fifth and last tamoxifen dose.

Mice were euthanised with terminal isoflurane anaesthesia, followed by vascular perfusion with 1x PBS (pH 7.4; Gibco, 70011) *via* the ventricle to clear blood from the tissues. Two different fixation techniques were employed depending on the subsequent analyses required. Immersion fixation was selected for tissues shared between immunohistochemistry (IHC) and flow cytometry with subsequent RNA sequencing. Hereby, tissues were incubated in 10% neutral buffered formalin (Sigma, HT501128) with gentle agitation at room temperature (RT) for 24 hours. Perfusion fixation was used for tissue preservation when used for IHC and RNA scope only. Here, perfusion fixation involved initial PBS flushing followed by perfusion with 4% (w/v) paraformaldehyde (Sigma, P1213) in 1x PBS (pH 7.4) at RT. Subsequently, tissues were transferred to 10% neutral buffered formalin (Sigma, HT501128).

2.3 Histological analysis

2.3.1 Tissue processing

Following fixation, tissues were transferred to 70% ethanol. Before being embedded in paraffin, tissues were dehydrated using a graded ethanol series (70%, 90%, 100%) and xylene. Formalin-fixed paraffin-embedded (FFPE) tissues were sectioned at 4 μm thickness using a Thermo Microm HM 355S Microtome. Approximately five sections are cut from each FFPE tissue block. Sections were floated on warm distilled water, mounted on poly-lysine-coated slides (Fisher, 10149870), and dried at 37°C for 3-24 hours. IHC was conducted shortly after tissue sections were cut to prevent oxidation and degradation of epitopes.

2.3.2 Single-label Immunohistochemistry (IHC)

For IHC, FFPE sections were first deparaffinized using xylene (2x 3min) and graded ethanol series (2x 3min 100%, 2x 3min 90%, 2x 3min 70%), followed by rehydration in double-distilled water. Antigen retrieval was performed using heat-induced epitope retrieval (HIER) in TE buffer (10 mM Tris, 1 mM EDTA; pH 9.0) in a steamer at a sub-boiling temperature (95°C – 98°C) for 15 min. Endogenous peroxidase activity was blocked with Dako Peroxidase Blocking Solution (Agilent, S2023) for 10 min at RT, and non-specific protein binding was prevented by incubating sections in 5% (w/v) bovine serum albumin (BSA, Sigma 5482) in 1x TBS-T (50 mM Tris, 31.6 mM NaCl, 0.1% (v/v) Tween-20; pH 8.4) for 40 min at RT. Primary α-tdTomato antibodies (Rockland, 600-401-379, Rabbit), diluted 1:1000 in Dako Antibody Diluent Solution (Agilent, S3022), were applied overnight at 4°C. Following primary antibody incubation, sections were washed in 1x TBS-T. The signal was detected using the Dako

Envision system (Agilent, K4003), with diaminobenzidine (DAB) exposure time set to 10 min. Nuclear counterstaining was performed with modified Harris Haematoxylin (Fisher, 72711), with differentiation in 0.25% HCl in 70% ethanol for 10 seconds. The haematoxylin stain was then blued in 0.06% (w/v) NH4OH in water for 30 seconds. Finally, slides were dehydrated using graded ethanol series (2x 3min 70%, 2x 3min 90%, 2x 3min 100%) and xylene (2x 3min) and mounted using DPX mountant (Merck, 06522).

2.3.3 Image analysis

After mounting, sections stained for tdTomato were imaged using the Hamamatsu NanoZoomer S210 slide scanner at 40x magnification. Images were reviewed using the NDP Viewer software which was also used to choose and extract all exemplar images presented in the following thesis. Further extracted exemplar images were analysed and processed using FIJI ImageJ.

2.3.4 TdTomato-positive cell quantification using Halo

The scanned tissue sections (Table 2.2) were used to determine and quantify the proportion of cells staining positive for tdTomato in the cortex. This proportion was quantified using HALO Image Analysis Software versions 3.5 and 3.6 (Indica Lab, Albuquerque, USA). For each kidney section, the renal cortex was manually annotated (Figure 2.1). This manual annotation used well-established anatomical features and the histological characteristics of renal tubules within this region. This included the position of the renal cortex in the kidney, cell density, the presence of glomeruli, and renal tubule architecture (44,45). To identify all cells of the cortex, the haematoxylin-stained nuclei were detected using the HALO AI v3.6 Nuclei Seq

algorithm. This was done since the detection of haematoxylin-stained nuclei is a reliable way of identifying cells which can later be deemed tdTomato-positive or negative. For the area of haematoxylin signal detected as a nucleus a threshold was chosen between 15 μm² and 200 μm², excluding all signals outside this range. Cells were classified as tdTomato-positive if the tdTomato signal exceeded a set intensity threshold within the detected nuclei and a 2 μm perimeter surrounding each nucleus. The same analysis parameters were applied across all slides stained for tdTomato.

Table 2.2: Scanned tissue sections used for the quantification of tdTomato-positive cells in the renal cortex using Halo: *Each genotype and the respective early (1-3 weeks after tamoxifen) and late (> 4 months after tamoxifen) time point listed was used for quantification of the proportion of tdTomato-positive cells in the renal cortex. The respective genotypes of the Von Hippel-Lindau (Vhl) gene and Polybromo 1 (Pbrm1) gene are shown. The number of sections listed represents the number of sections taken from individual mice, followed by the ratio of male to female mice. All mice received 5 x 2mg tamoxifen to induce recombination.*

Name	*Vhl*	*Pbrm1*	Time point	Sections: Male/Female	Tamoxifen
ConKO	wt/pjr.fl	wt/wt	Early	15: 9/6	5 x 2mg
VKO	jae.KO/pjr.fl	wt/wt	Early	13: 6/7	5 x 2mg
ConPKO	wt/pjr.fl	fl/fl	Early	13: 10/3	5 x 2mg
VPKO	jae.KO/pjr.fl	fl/fl	Early	16: 9/7	5 x 2mg
ConKO	wt/pjr.fl	wt/wt	Late	14: 10/4	5 x 2mg
VKO	jae.KO/pjr.fl	wt/wt	Late	10: 9/1	5 x 2mg
ConPKO	wt/pjr.fl	fl/fl	Late	17: 5/12	5 x 2mg
VPKO	jae.KO/pjr.fl	fl/fl	Late	30: 20/10	5 x 2mg

Figure 2.1: Example of a manually annotated renal cortex: *Representative kidney section stained for tdTomato (brown) and with haematoxylin (blue) with manually annotated cortex (yellow) as it was done for cell number and cluster quantification. The section was taken from* $Vhl^{wt/pjr.fl}$*;* $Pax8\text{-}CreER^{T2}$ *mouse harvested at the late time point*

2.3.5 Cluster quantification using QuPath

2.3.5.1 Pixel classifier training

The scanned stained tissue sections were further used to train a pixel classifier for contiguous tdTomato-positive clusters. This was done using the open-source digital pathology software QuPath version 0.5.1 (46). For this detection, an artificial neuronal network-based pixel classifier was trained on 10 stained tissue sections using the train pixel classifier function in QuPath. These 10 example images were uploaded to a QuPath project, and the image type was set to “Brightfield H-DAB”. Then, each randomly selected example region for tdTomato-positive cell clusters and tdTomato-negative cells were manually annotated in each image (Table 2.3). This was done by only displaying the DAB channel and encircling the respective positive or negative region using the wand tool (Figure 2.2). This was done for a random number of examples until a wide variety of examples was covered and until annotated positive and negative regions were equally represented by area (Table 2.3). The annotated example images were subsequently loaded into the “train pixel classifier” option using the “load training” function. As for the classifier type, the suggested “Artificial neuronal network (ANN_MLP)” class was chosen. For resolution, the full resolution of 2.5 pixels/µm was used and in the feature option, only the DAB channel with a scale of 0.5 and 1 was chosen. The classifier output was set to “Classification” and the region of interest was set to “Any annotation ROI”. Additionally, to help identify clusters separately that are very close together, an annotation boundary was set in the advanced options menu. Hereby, the outer 3 pixels of the detected DAB positive annotation are classified as negative. All other options were left at their recommended standard settings.

Table 2.3: Example images used to train pixel classifier: *10 example images used for classifier training all stained for tdTomato (DAB) and Haematoxylin. Positive Examples list the number of continuous DAB stains manually annotated. Negative Examples lists the number areas of non-DAB positive background annotated.*

Example Images	Positive Examples	Negative Examples
1	33	29
2	33	12
3	27	18
4	70	26
5	47	12
6	18	23
7	55	22
8	124	21
9	89	35
10	84	22

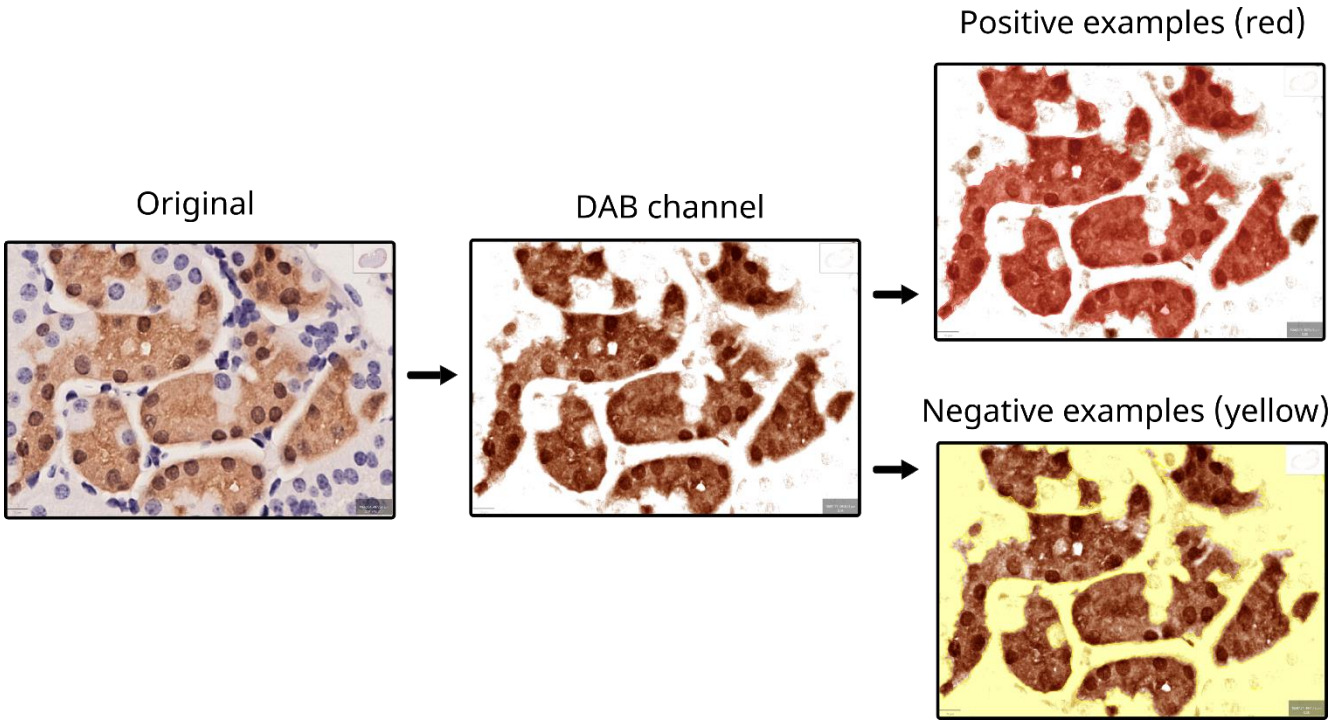

Figure 2.2: Examples of manually annotated tdTomato positive and negative areas: *Original IHC stained tissue section (left) stained for tdTomato (brown) and Haematoxylin (blue), DAB channel used for accurate manual annotation (middle), manually annotated tdTomato positive (right, top) and tdTomato negative (right, bottom) examples for training the pixel classifier*

2.3.5.2 Cluster and Cell Detection Workflow

Selected scanned tissue sections were used to annotate contiguous tdTomato-positive clusters using the cleated trained pixel classifier and to detect the nuclei within them (Table 2.4). To do so, the selected scanned tissue sections were uploaded to a QuPath project and the cortex was manually annotated. In the first step, the previously trained pixel classifier is applied to the annotated cortex with the maximum hole size set to 15µm² and the minimum annotation size set to 30µm². This creates new annotations around all contiguous tdTomato-positive signals (Figure 2.3). In the second step, the newly created annotations are selected and the nuclei within these annotations are detected *via* the watershed algorithm-based cell detection function (Figure 2.3). for cell detection following parameters were used: Detection Image: "Haematoxylin OD"; PixelSize: "0,5 µm"; Background radius: 8.0 µm; Median filter radius: "0.0µm"; Sigma: "1.5µm"; Minimum area: "10µm²"; Maximum area: "100µm²"; Threshold: 0.1; Max background intensity: "2.0"; Split by shape; "TRUE"; Exclude DAB: "FALSE"; Cell expansion: "7.0µm"; Include nuclei: "TRUE"; Smooth boundaries: "TRUE"; Make measurement: "TRUE". After the cells were detected within each annotation, the annotation measurements including the number of cells in each annotation were exported. This whole process was applied to all scanned tissue sections in the QuPath project at the same time in an automated fashion. Enabled by the "automate" function in QuPath a script was created that subsequently applies each step to the image and exports the measurements (Figure 2.3). The collected data was processed in R where annotations without detected cells were removed and scanned tissue slides were assigned to their genotype and timepoint. Violin charts showing the distribution of the number of cells per annotation were created using ggplot2. The mean cluster size was calculated by taking the mean of the number of cells detected in each annotation of each sample. This was plotted for each genotype and time point with bars displaying the mean and interquartile range. Statistical comparison was done using ANOVA test for group variability

and the non-parametric Kruskal-Wallis-test for significance in multiple comparisons. Additionally, clusters were separated into single cells and small clusters (1-5 cells per cluster), medium clusters (6-15 cells per cluster), and large clusters (15+ cells per cluster). The number of the respective clusters was divided by the total number of clusters in each sample. This proportion was plotted for each cluster size and genotype comparing early and late time points. The non-parametric Kruskal-Wallis-test was used to test for significance.

Table 2.4: Scanned tissue sections used for cluster quantification in QuPath: *Each Genotype and the respective early (1-3 weeks after tamoxifen) and late (> 4 months after tamoxifen) time point listed was used for cluster quantification. The respective genotypes of the Von Hippel-Lindau (Vhl) gene and Polybromo 1 (Pbrm1) gene are shown. The number of sections listed represents the number of sections taken from individual mice, followed by the ratio of male to female mice. All mice received 5 x 2mg tamoxifen to induce recombination.*

Name	*Vhl*	*Pbrm1*	Time point	Sections: Male/Female	Tamoxifen
ConKO	wt/pjr.fl	wt/wt	Early	12: 5/7	5 x 2mg
VKO	jae.KO/pjr.fl	wt/wt	Early	9: 4/5	5 x 2mg
ConPKO	wt/pjr.fl	fl/fl	Early	6: 4/2	5 x 2mg
VPKO	jae.KO/pjr.fl	fl/fl	Early	8: 5/3	5 x 2mg
ConKO	wt/pjr.fl	wt/wt	Late	11: 7/4	5 x 2mg
VKO	jae.KO/pjr.fl	wt/wt	Late	8: 6/2	5 x 2mg
ConPKO	wt/pjr.fl	fl/fl	Late	8: 4/4	5 x 2mg
VPKO	jae.KO/pjr.fl	fl/fl	Late	15: 9/6	5 x 2mg

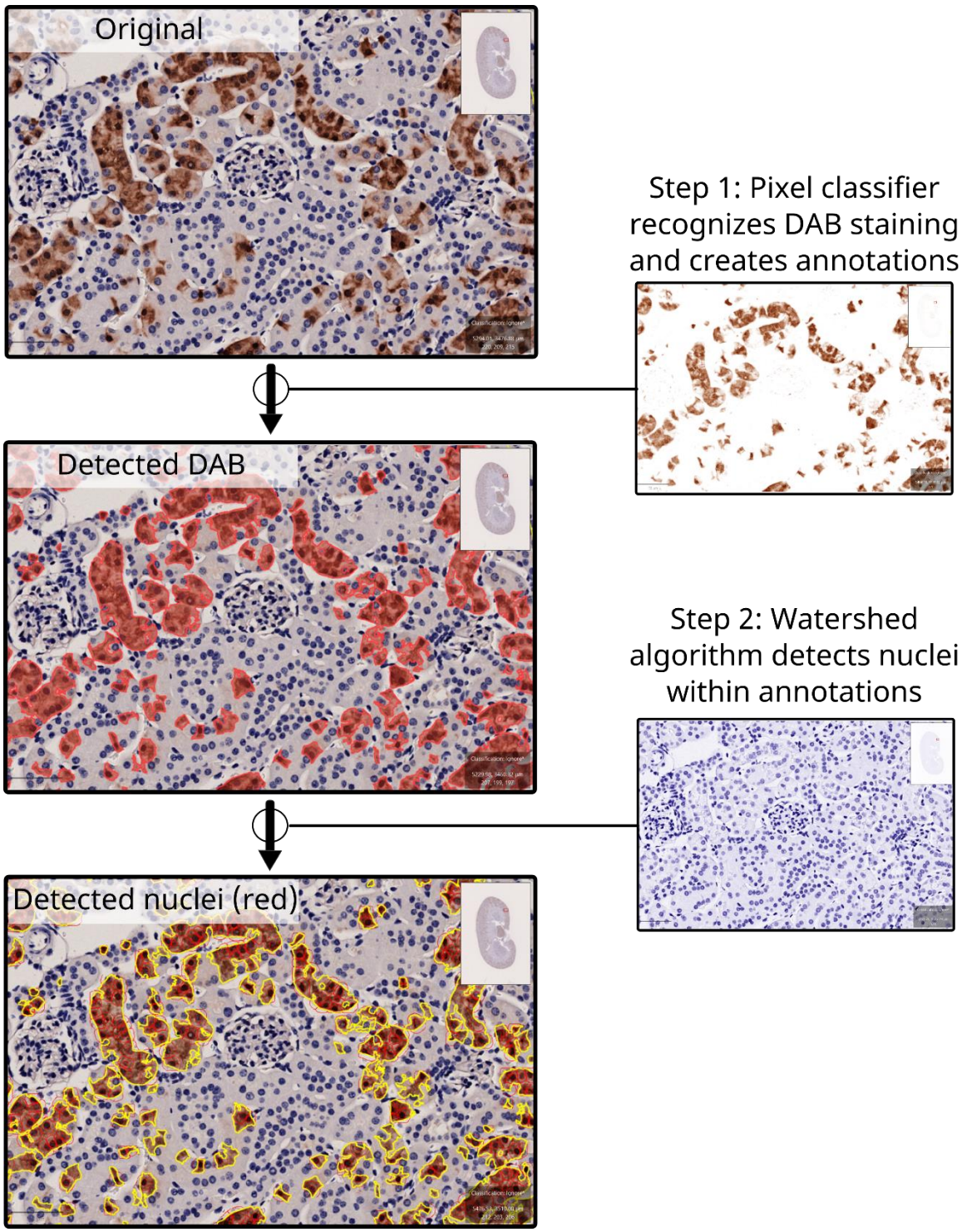

Figure 2.3: Schematic depiction of the developed QuPath workflow: *The original section was stained for tdTomato, uploaded to a QuPath project and the region of interest (cortex) was annotated.* ***Step1****: The workflow was applied to the project which utilised the pixel classifier to encircle contiguous tdTomato signals and to create annotations.* ***Step 2****: A watershed algorithm detects nuclei within the annotations. These detections will be exported and grouped by annotations. These data are subsequently used for the quantification of cluster size.*

2.4 RNA Sequencing of FAC sorted single cell suspensions

Table 2.5: Mice used for transcriptome analysis: *One fresh kidney was harvested of each mouse at the indicated time point after tamoxifen-induced recombination. Kidneys were dissociated and subsequently used for FAC sorting to extract and sequence their RNA. The respective genotypes for the Von Hippel-Lindau (Vhl) and Polybromo-1 (Pbrm1) gene are shown.*

Name	*Vhl*	*Pbrm1*	Days after tamoxifen	Sex	Tamoxifen
ConKO	wt/pjr.fl	wt/wt	360	Male	5 x 2mg
VKO	jae.KO/pjr.fl	wt/wt	332	Male	5 x 2mg
VKO	jae.KO/pjr.fl	wt/wt	298	Male	5 x 2mg
VPKO	jae.KO/pjr.fl	fl/fl	297	Male	5 x 2mg
VPKO	jae.KO/pjr.fl	fl/fl	298	Male	5 x 2mg

2.4.1 Kidney dissociation

Fresh kidneys (Table 2.5) were processed into single-cell suspensions suitable for fluorescence-activated cell sorting (FACS) for subsequent RNA extraction and sequencing (RNA-seq) experiments. The dissociation procedure was carried out using the Multi-Tissue Dissociation Kit 2 (Miltenyi, 130-110-203). After removing the renal capsule, the kidney tissue was finely minced with a scalpel for 5 min. The finely minced tissue was then enzymatically dissociated in a solution containing 1.45 ml of Buffer X, 30 µl of Enzyme D, 15 µl of Enzyme P, 15 µl of Buffer Y, and 6 µl of Enzyme A, which was prepared according to the manufacturer's protocol. The tube containing the mixture was submerged in water and incubated for 30 min at 37°C in a shaking incubator set to 150 rpm. To halt the enzymatic dissociation, 150 µl of Foetal Bovine Serum (FBS; Sigma, F7524) was added, followed by resuspension of the cells and

remaining tissue in 9 ml of RPMI-1640 medium (Merck, R0883). The resulting suspension was passed through a 40 μm cell strainer to remove undigested tissue. The filtered cell suspension was then centrifuged at 300g for 10 min at 4°C. To remove red blood cells, the cell pellet was resuspended in 3 ml of 1x RBC Lysis Buffer (Miltenyi, 130-094-183), prepared from 10x stock solution in double distilled water, and incubated for 2 min at room temperature. After lysis, the cells were centrifuged for 5 min at 300g at 4°C and resuspended in ice-cold D-PBS. The final cell count and viability were determined using a Thermo Scientific Countess II automated cell counter.

2.4.2 Fluorescent-activated cell sorting (FACS)

Single cells obtained after tissue dissociation were resuspended in D-PBS (Thermo, 14190144) containing 10% Fetal Bovine Serum (FBS) and 2 mM EDTA. To achieve a final concentration of 5 million viable cells per ml cells were resuspended in a volume according to the measured viability. For viability assessment while sorting, 10 μl of 10 μg/ml DAPI (Sigma, D9542) was added to the suspension 5 min prior to FAC sorting. Cell sorting was conducted using a BD Aria Fusion Cell Sorter at the Flow Cytometry Facility, Wellcome Trust Centre for Human Genetics by Dr Ruddy Montandon, Ghada Ben Youssef, and Mohammed Islam. The sorting was performed by members of the Flow Cytometry Facility. For fluorescence detection of tdTomato, it was excited with a laser at 561 nm wavelength, and its emission was captured using a 582/15 band pass filter. For DAPI fluorescence detection, it was excited with a laser at 405 nm wavelength and detected using a 450/40 band pass filter. Polypropylene tubes pre-coated with FBS were used to collect live, tdTomato-positive, single cells. Collected single-cell suspensions were then pelleted by centrifugation for 10 min at 300g, resuspended in PBS, and

recounted to determine yield and viability. After, suspensions were directly processed by extraction of the RNA for subsequent RNA-sequencing experiments.

2.4.3 RNA extraction

For the tdTomato positive cell suspension, RNA was extracted immediately after FACS sorting using the Qiagen RNeasy mini plus RNA extraction Kit (Qiagen, 74104). First, sorted cells were pelleted by centrifugation for 10 min at 300g and resuspended in 350 µL RLT buffer (Qiagen, 79216) containing 40 nM dithiothreitol (DTT; Thermo Fisher Scientific, R0861). For optimal lysis, the suspension was vortexed vigorously for 30 sec. After lysis, 350 µL of 70% ethanol was added to each sample and the mixture was loaded onto the RNeasy spin column. The columns were centrifuged for 15 sec at 8000g and the flow through was removed. To remove any residual genomic DNA from the column-bound RNA, an on-column DNase digestion step (Qiagen, 79254) was performed according to the manufacturer's instructions. This was followed by two rounds of washes with 500 µL RPE Buffer (Qiagen, 1018013) and 30 sec of centrifugation. This was followed by 3 min of centrifugation at full speed to remove any remaining wash buffer from the column. After washing, the extracted RNA is eluted by adding 25 µL nuclease-free water and centrifugation for 1 min at 8000g. The quality and concentration of the extracted RNA were checked using the Qubit™ RNA HS Assay Kit (Qubit, Q32852, Q32855) and Agilent RNA ScreenTape analysis (Agilent, 5067 5576).

2.4.4 Library Preparation and Sequencing

After RNA extraction, libraries were generated using a maximum of 500 ng of RNA. If the total amount of extracted RNA was lower than 500ng, all the available RNA was used to generate the library. To enrich for mRNA and separate it from rRNA, the NEBNext® Poly(A) mRNA Magnetic Isolation Module (New England Biolabs, E7490S) was used as per the manufacturer's protocol. After mRNA isolation, the NEBNext® Ultra™ II Directional RNA Library Prep Kit for Illumina® (New England Biolabs, E7760S) was employed, following the manufacturer's instructions for RNA fragmentation, cDNA synthesis, dA-tailing, adapter ligation, USER enzyme digestion, and PCR amplification. For the cDNA synthesis, samples containing <250 ng of RNA, a 25-fold adaptor dilution was chosen. If the sample contained more than 250 ng of RNA, a 10-fold adaptor dilution was used. Samples were indexed using the NEBNext® Multiplex Oligos for Illumina® (Dual Index Primers Set 1) (New England Biolabs, E7600S), following the manufacturer's instructions. Samples were pooled according to the respective quantity of adapter-bound mRNA which was measured by using the NEBNext Library Quant Kit for Illumina (New England Biolabs, E7630S). The Illumina NextSeq 1000/2000 system was used to sequence the pooled library which resulted in comprehensive RNA sequencing data. Library preparation was performed by Dr. Samvid Kurlekar.

2.4.4 Preprocessing of RNA sequencing data

A pipeline was applied to the generated RNA sequencing data which first removed adapter sequences with the use of TrimGalore (version 0.3.3, Babraham Bioinformatics). The next step of the pipeline employed HISAT2 (version 2.0.5) (47) to align the reads to the mm10 mouse reference genome, and fragments that did not map uniquely to the genome were removed using Picard tools (version 2.0.1, Broad Institute). Finally, the total read counts for each gene,

as defined by UCSC (GRCm38/mm10), were obtained using HTSeq (version 0.5.4p3) (48) with the "intersection-strict" mode. Subsequently, DESeq2 (49) was used to normalize the reads of each detected gene to the total read count of the sample. Next, two comparisons were made, on the one hand, to see the influence of *Vhl* loss on its own (VKO *vs* ConKO) and on the other hand to see the influence of *Pbrm1* loss on top of *Vhl* loss (VPKO *vs* VKO). Here, DESeq2 calculated the Log2 fold change (FC) between the mean read count of each condition for each gene. For each gene, a Wald test is applied to determine the significance of the fold change. To control for the false discovery rate (FDR) the resulting p-value is Benjamini and Hochberg (BH) adjusted. This resulted in gene lists ranking genes according to their significance. Preprocessing of raw sequencing data and development of the pipeline was performed by Dr. Ran Li.

2.4.4 Downstream analysis of RNA sequencing data

Both gene lists were used to plot volcano plots using the ggplot2 (50) package in R. Here, a -log10 adjusted *p*-value was calculated and plotted over the log2FC (VKO *vs* ConKO and VPKO *vs* VKO). The significance cutoff value was set to 0.05. A gene score was calculated by multiplying -log10 adjusted p-value and log2FC, which was used to rank genes. The top 25 highest-ranking genes were labelled with gene symbols. Next, Kyoto Encyclopaedia of Genes and Genomes (KEGG) pathway enrichment analysis was conducted on the significantly enriched genes ($p > 0.05$) of the upregulated (log2FC >1.2) genes for VKO *vs* ConKO as a control. The same was done for upregulated (log2FC > 1.2) and downregulated (log2FC < 1.2) genes of the VPKO *vs* VKO gene list. This was done using the enrichKEGG function of the R package clusterProfiler (51) and the results were plotted as a dot plot using the dotplot function. These dot plots show the respective pathway ranked by the gene ratio (number of genes mapped to the KEGG pathway divided by the total number of genes). The dot size represents the gene

count (number of genes mapped to the respective pathway) and the colour represents the BH-adjusted p-value. A scatter plot was created by plotting the Log2FC of VKO *vs* ConKO against the Log2FC of VPKO *vs* VKO for all genes that passed the significance threshold ($p < 0.05$). The genes were coloured according to whether they were found significant in VPKO *vs* VKO (purple), VKO *vs* ConKO (orange), or significant in both (green). A cutoff was defined for Log2FC at > 1.2 (red) and < -1.2 (blue). The R package ggVennDiagram (52) was used to plot Venn diagrams comparing upregulated genes in both comparisons and downregulated genes in both comparisons. Further, a comparison was made between upregulated genes and downregulated genes and vice versa. The centre of the Venn diagram displays the number of genes found in both comparisons. These genes are extracted and labelled with their gene symbols above and below the diagram. For the next analysis, two gene lists were used which have been previously established by Samvid Kurlekar and Joanna Lima using the VKO mouse model extended for a *Hif1a* and/or an *Epas1* knock-out. Here, single-cell RNA sequencing was conducted on tdTomato-positive cells resulting in lists of HIF1A- and HIF2A-specific target genes. These lists were used to conduct genes set enrichment analysis with the obtained RNA sequencing data. For both comparisons (VPKO *vs* VKO and VKO *vs* ConKO) genes were ranked on the x-axis according to their fold change. On the y-axis, the proportion of recovered gene set (HIF1A-target list or HIF2A target list) at the respective fold change was plotted. Further, genes from the HIF1A and HIF2A target lists found in our data sets were plotted in a heatmap using the R package pheatmap (53). Hereby, the normalised reads are taken and normalised for each gene (ConKO + VKO + VPKO = 0). The clustering was performed in an unsupervised fashion and genes were labelled as either HIF1A or HIF2A targets.

2.5 Statistics

To compare the survival of tdTomato-cells and the mean cluster sizes in the cortex of ConKO, VKO, ConPKO and VPKO mice at early and late time points the D'Agostino-Pearson omnibus normality test was applied to the data. If the data met the assumptions of normality, group differences were analysed using two-way ANOVA with Holm-Šidak correction for multiple comparisons. If the data did not pass the normality test, the Kruskal-Wallis test was applied for group comparisons, with Dunn’s correction for multiple testing.

For differential expression testing, *p* values were calculated using the Wald test to determine the significance of the fold change. Subsequently, the resulting *p*-values are adjusted using the Benjamini and Hochberg (BH) procedure to control for the false discovery rate (FDR).

3. Results

3.1 Histological analysis

Previous studies have investigated the change in the proportion of tdTomato-positive cells in the cortex, outer medulla, inner medulla, and papilla of the kidney of *Vhl*$^{jae.KO/pjr.fl}$, *Pax8-CreERT2* (VKO) and *Vhl*$^{wt/pjr.fl}$, *Pax8-CreERT2* (ConKO) mice over time. Comparison of the four regions of kidneys harvested at two distinct time points, early (1-3 weeks) and late (4-12 months) after tamoxifen treatment, revealed time-dependent changes in kidneys of VKO: an increase of tdTomato-positive cells in the cortex and a decrease in tdTomato-positive cells in the papilla. No changes were reported in either ConKO mice or in the outer and inner medulla of VKO mice. This suggested that homozygous *Vhl*-loss in tubular epithelial cells of the renal cortex leads to increased survival and expansion over time. As described before, *Pbrm1* is involved in several processes associated with cell division, therefore the aim was to investigate whether additional *Pbrm1* loss is affecting the expansion and survival of *Vhl*-null cells in the cortex.

3.1.1 *Pbrm1* loss does not affect the expansion of *Vhl*-null cells in the renal cortex

To assess the impact of *Pbrm1* loss on the survival of *Vhl*-null tubular epithelial cells within the renal cortex, kidneys were harvested from *Vhl*$^{wt/pjr.fl}$, *Pbrm1*$^{fl/fl}$, *Pax8*-CreERT2 (ConPKO) and *Vhl*$^{jae.KO/pjr.fl}$, *Pbrm1*$^{fl/fl}$, *Pax8*-CreERT2 (VPKO) mice at early (1-3 weeks) and late (4-12 months) time points following tamoxifen-induced recombination. Immunohistochemistry (IHC) was performed on kidney sections from both early (13 ConPKO,

16 VPKO) and late (17 ConPKO, 30 VPKO) time points to visualise and quantify tdTomato-positive cells within the renal cortex, with each section representing an individual animal. High-resolution scans of these sections were analysed using the AI-based cell detection software HALO®, which enabled precise identification and quantification of tdTomato-positive and -negative cells, thereby determining the proportion of tdTomato-positive cells in the renal cortex. These data were then compared to previously published results from VKO and ConKO kidney sections obtained using identical methods.

Initial visual comparisons of tdTomato-stained sections from ConKO, ConPKO, VKO, and VPKO kidneys at the early time point suggested no discernible differences in the number of tdTomato-positive cells. This observation was rigorously tested with HALO®, which confirmed that the proportion of tdTomato-positive cells in the renal cortex did not significantly differ between these groups (Supplementary Figure 1). These findings indicate that there is no immediate effect of *Vhl*, *Pbrm1*, or combined *Vhl/Pbrm1* loss on the number of tdTomato-positive cells in the cortex and that the initial number of recombined cells at the early time point is consistent across all genotypes.

At the late time point, visual examination of tdTomato-stained sections revealed an expected increase in the proportion of tdTomato-positive cells in VKO cortices following *Vhl* loss. Interestingly, a comparable increase was observed in VPKO cortices, suggesting a similar trend. Quantitative analysis corroborated these observations: the proportion of tdTomato-positive cells in VKO cortices increased significantly from 10% at the early time point to 19% at the late time point ($p = 0.001$) (Figure 3.1A), consistent with previously published findings. Similarly, VPKO cortices showed a significant increase in tdTomato-positive cells, from 11% to 17% ($p = 0.001$), over the same period. However, there was no statistically significant difference between VKO and VPKO at the late time point, indicating that *Pbrm1* loss does not alter the overall expansion of *Vhl*-null cells in the renal cortex.

Further validation was provided by plotting the number of tdTomato-positive cells per mm^2 of tissue, which controlled for potential increases in the total number of cortical cells due to immune cell infiltration (Supplementary Figure 2). In contrast, no significant differences were observed in the proportion of tdTomato-positive cells between early and late time points in ConKO and ConPKO mice (Figure 3.2B), suggesting that neither heterozygous *Vhl* loss nor homozygous *Pbrm1* loss independently affects cell survival in the renal cortex over time. Collectively, these results suggest that the expansion of VKO and VPKO cells in the renal cortex is driven primarily by *Vhl* loss.

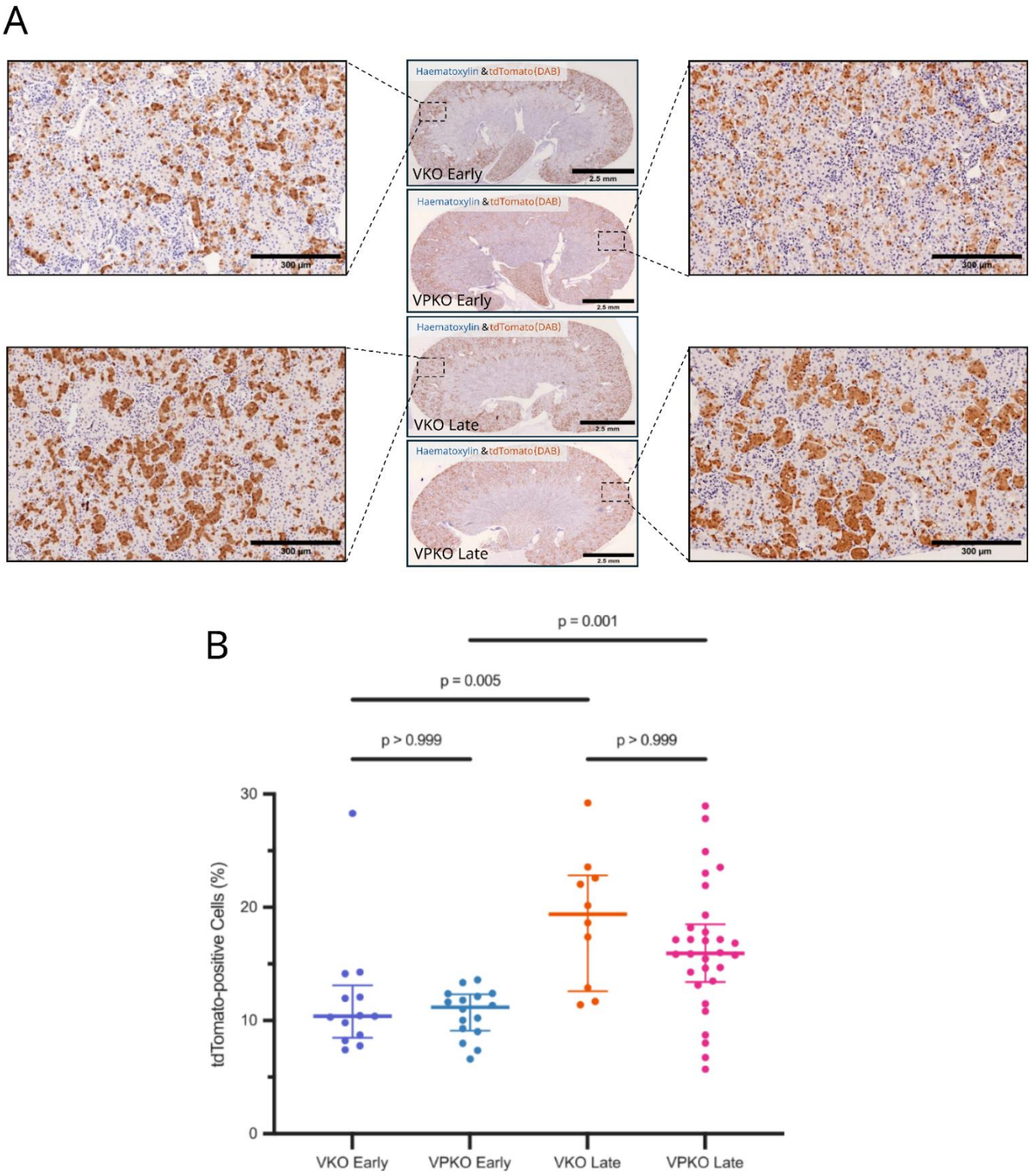

Figure 3.1: Qualitative and quantitative display of the proportions of tdTomato-positive cells in the renal cortex of VKO and VPKO mice: (A) *Exemplar image of the entire 4µm thick kidney section of VKO and VPKO at the early (1-3 weeks) and late (>4 months) time point stained for tdTomato (DAB) and Nuclei (Haematoxylin). Zoomed-in window shows an exemplary 20x image of the renal cortex for each genotype and time point.* ***(B)*** *The percentage of tdTomato-positive cells in the renal cortex, as detected by the AI-based HALO® cell detection system, plotted the cortices of 13 VKO and 16 VPKO kidney sections at the early time point and 10 VKO and 30 VPKO at the late time point. (1-3 weeks) and late (>4 months) time point. ANOVA test was used to test for group variability and significance in multiple comparisons was tested using the non-parametric Kruskal-Wallis-test.*

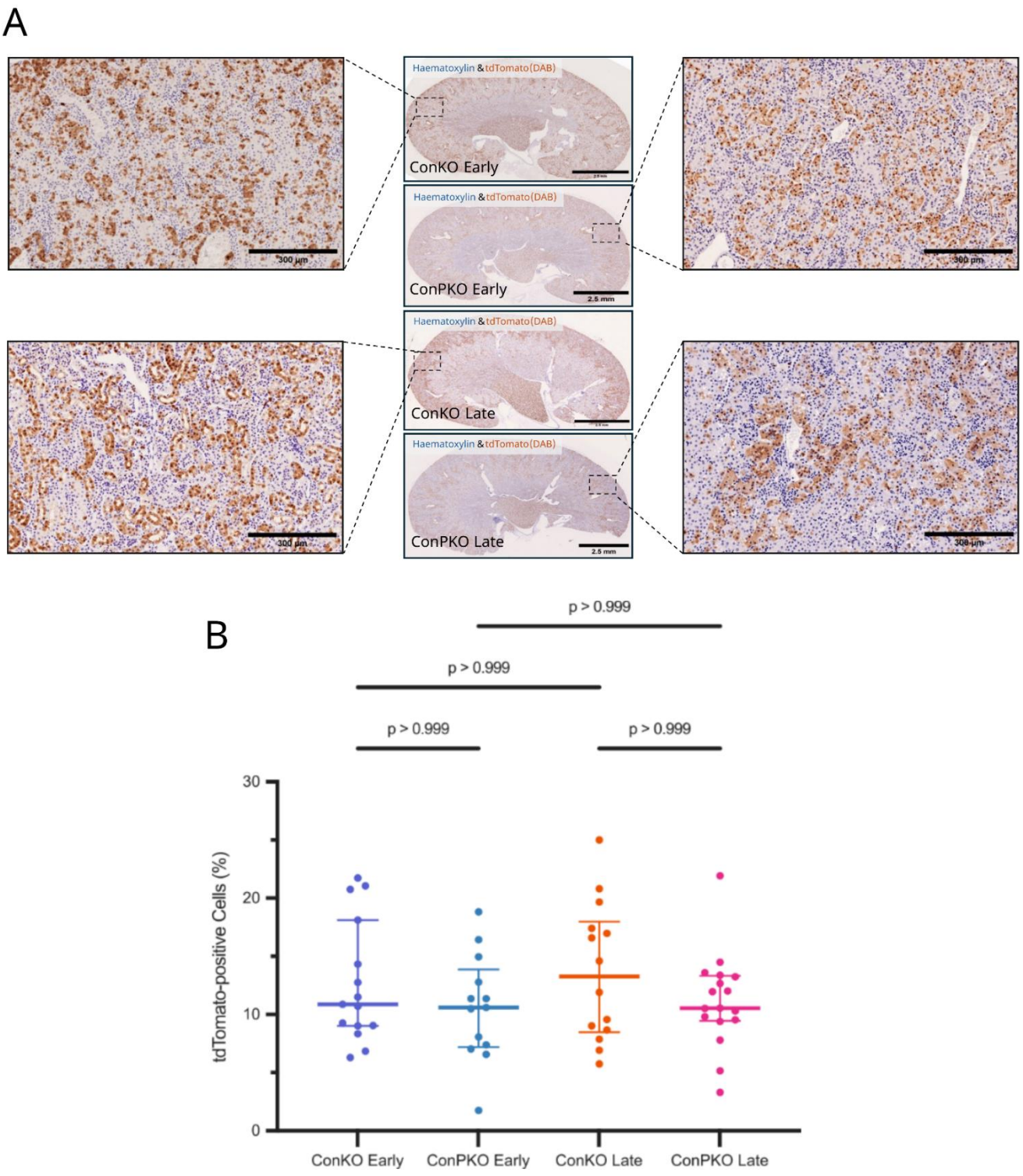

Figure 3.2: Qualitative and quantitative display of the proportions of tdTomato-positive cells in the renal cortex of ConKO and ConPKO mice: (A) *Exemplar image of the entire 4µm thick kidney section of ConKO and ConPKO at the early (1-3 weeks) and late (>4 months) time point stained for tdTomato (DAB) and Nuclei (Haematoxylin). Zoomed-in window shows an exemplary 20x image of the renal cortex for each genotype and time point.* ***(B)*** *Percentage of tdTomato-positive cells in the renal cortex, as detected by the AI-based HALO® cell detection system, plotted for ConKO and ConPKO cortices at the early (1-3 weeks) and late (>4 months) time point. ANOVA test was used to test for group variability and significance in multiple comparisons was tested using the non-parametric Kruskal-Wallis-test.*

3.1.2 The morphology of ConPKO and VPKO cell clusters is altered over time

Recent studies have highlighted the necessity of concomitant *Vhl* and *Pbrm1* loss in the renal tubular epithelium within the kidney cortex to induce ccRCC-like lesions after 17-20 months. These findings prompted an investigation into the morphology and distribution of tdTomato-positive cells in the kidney cortex of animals in the current experimental cohort. The upper age limit of the cohort at the late time point was 12 months. As expected, no solid tumour formation was observed within this timeframe. Given that this study, unlike previous ones, allowed for the visualisation of *Vhl/Pbrm1*-null cells before tumour formation, it was hypothesised that changes in the topology and organisation of tdTomato-positive cells might indicate the early onset of tumour formation. To explore this, the organisation of recombined cells relative to each other was examined, with a particular focus on the formation of clusters. Clusters were defined as a minimum of two directly adjacent recombined cells forming areas of contiguous tdTomato staining. The size and morphology of these clusters were compared over time according to genotype, and their potential to form tumours was evaluated.

To investigate the formation of tdTomato-positive clusters, all scanned slides of ConKO, ConPKO, VKO, and VPKO kidneys stained for tdTomato at early and late time points were manually reviewed. In the early time point sections from ConKO, ConPKO, VKO, and VPKO kidneys, recombined cells were evenly distributed, with few positive cells directly adjacent to each other. In rare instances, the cross-section of a tubule was predominantly composed of positive cells, forming small clusters. These clusters were typically interspersed with tdTomato-negative cells, and the affected tubules displayed no morphological differences from those entirely comprised of non-recombined, tdTomato-negative cells.

Comparing the distribution and morphology of tdTomato-positive cells in ConKO kidney sections between early and late time points revealed no visible changes. Small clusters of tdTomato-positive cells were occasionally formed by coincidental recombination in adjacent cells; however, these clusters did not expand over time and showed no morphological differences compared to adjacent non-recombined, tdTomato-negative cells (Figure 3.3A).

In ConPKO mice, the overall proportion of tdTomato-positive cells remained unchanged over time, with the number of clusters comparable to those found in ConKO cortices. Interestingly, a small subset of these clusters exhibited changes in morphology 12 months after recombination (Figures 3.3C & 3.3D). These morphologically abnormal clusters, forming the cross-section of tubules primarily composed of tdTomato-positive cells but occasionally interspersed with tdTomato-negative cells, were deemed dysplastic tubules. These tubules displayed an altered morphology characterised by a bulged appearance, fluctuating thickness, and a distinct deviation from the regular, uniform, tube-like shape of healthy tubules. Additional changes observed in these dysplastic tubules fell into two distinct categories: some resembled cystic tubules with a visibly dilated lumen surrounded by a tdTomato-positive cell border (Figure 3.4C), while others exhibited densely packed cells, resembling a tumour-like state with no visible lumen and closely packed nuclei (Figure 3.4D). These dysplastic tubules were only observed in the renal cortex and in no other region of the kidney. Adjacent tdTomato-negative tubules appeared completely normal, showing no differences compared to negative tubules in other genotypes though lesions in unmarked cells may be more difficult to detect.

In VKO cortices, HALO® cell detection analysis (Figure 3.1B) revealed an expansion of tdTomato-positive cells in the renal cortex, reflecting a slight decrease in single tdTomato-positive cells alongside an increase in the number of cells per contiguous tdTomato-positive cluster. These clusters, which occasionally spanned the entire cross-section of a tubule,

displayed no abnormalities and appeared morphologically similar to adjacent tubules entirely composed of non-recombined, tdTomato-negative cells (Figure 3.3B).

In VPKO cortices, an increase in the number of cells forming contiguous tdTomato-positive clusters was observed over time. These clusters expanded along the tubules of the cortex and occasionally occupied the entire cross-section of the tubule. Conversely, the number of single tdTomato-positive cells and patches of 2-4 cells appeared to decrease. Dysplastic tubules were visible in VPKO cortices as early as 5 months after recombination (Figures 3.4A, 4B), although these clusters remained a rare subset of tdTomato-positive clusters. Over time, the number of clusters increased, along with the severity of their morphological abnormalities. By 12 months, some clusters had lost their tubule-like structure, adopting a cystic tubule state (Figure 3.4C) or a tumour-like state (Figure 3.4D). Dysplastic tubules in VPKO cortices were more common and exhibited a more severe phenotype than those observed in ConPKO cortices. Again, dysplastic tubules in VPKO cortices were only observed in the renal cortex.

To explore the extent to which these morphological alterations contributed to cancer formation, kidney sections from VPKO mice 17 months after tamoxifen-induced recombination were reviewed. At this time point, which was not included in the statistical analysis, both the size and number of tdTomato-positive clusters had markedly increased. Cystic tubules had transformed into full-sized cysts (Figure 3.4E), and tumour-like tubules had developed into tumourlets, characterised by a loss of tubule structure and densely packed, disorganised cells (Figure 3.4F).

In summary, visual inspection of ConKO and VKO kidney cortices stained for tdTomato indicated that neither heterozygous nor homozygous knock-out of the *Vhl* gene led to any morphological alteration of recombined cells or clusters at any time point. Furthermore, homozygous *Vhl* loss did not result in increased clustering of cells. In contrast, clusters of tdTomato-positive cells in VPKO kidneys appeared larger and comprised more cells compared

to clusters in kidneys of other genotypes. Over time, positive cell clusters in VPKO kidneys increased in size and number, forming dysplastic lesions and dilated, cystic tubules. The earliest signs of dysplastic and dilated tubules were observed as early as 5 months after tamoxifen-induced recombination, with lesions displaying crowded, disorganised nuclei and large lesions appearing after 11 months. Although present, lesions in the renal cortex of ConPKO mice were less common and less severe than those observed in VPKO cortices and appeared later, 12 months after tamoxifen-induced recombination.

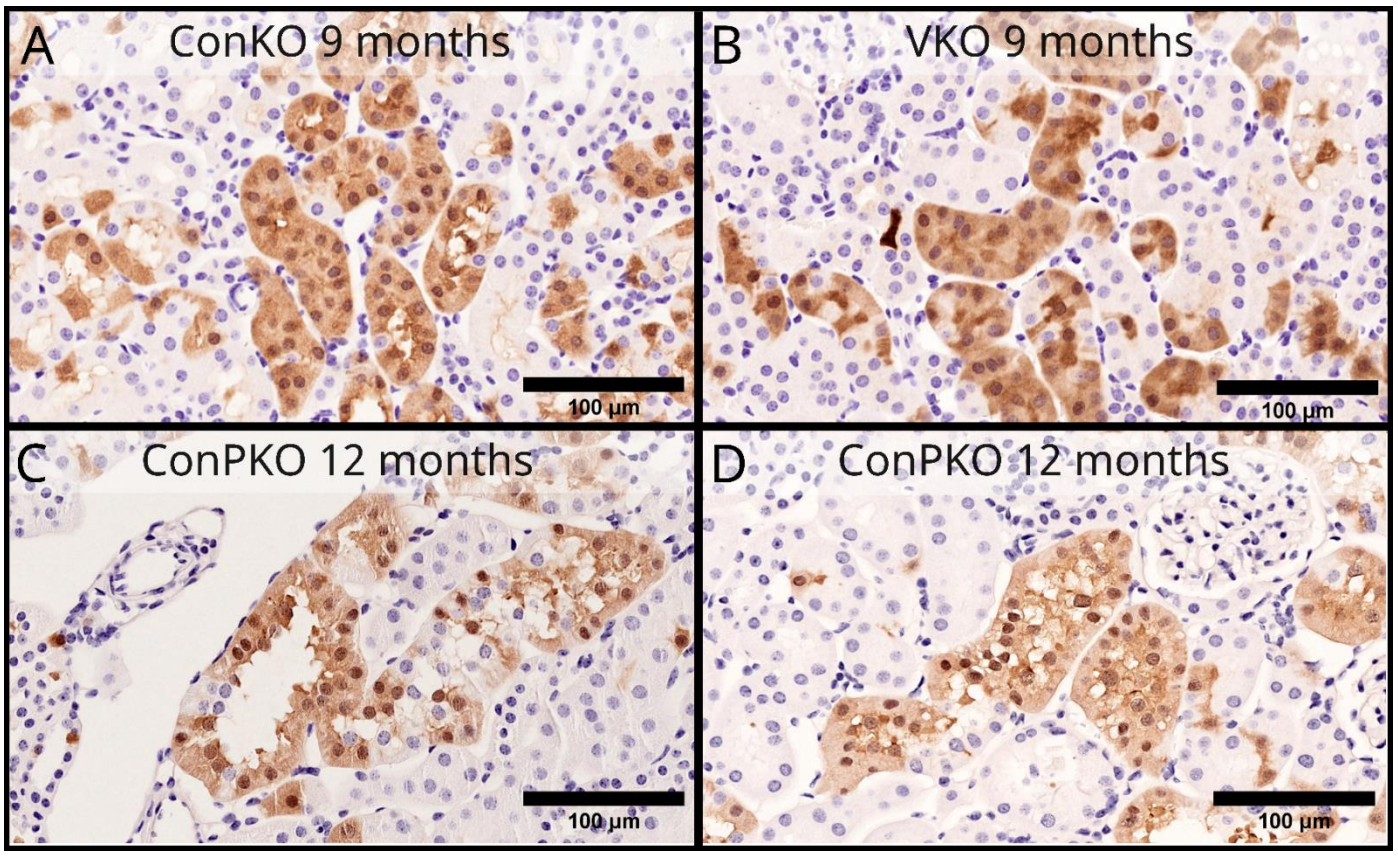

Figure 3.3: Examples of morphological abnormalities of tdTomato-positive cell clusters in cortices of ConKO, VKO, and ConPKO mice: *Representative image of tdTomato-positive cell clusters in the cortex of ConKO, VKO, and ConPKO mice. Image taken of 4µm thick kidney section stained for tdTomato (DAB) and Nuclei (Haematoxylin) with Hamamatsu NanoZoomer S210 at 40x magnification.* ***(A)*** *Image of average clusters found in the cortex of ConKO mice 9 months after tamoxifen-induced recombination.* ***(B)*** *Image of average clusters found in the cortex of VKO mice 9 months after tamoxifen-induced recombination.* ***(C)*** *Image of clusters found in the cortex of ConPKO mice 12 months after tamoxifen-induced recombination. The image represents dysplastic tubules of the cystic tubule type displayed by some tdTomato-positive cell clusters in the cortex of ConPKO mice.* ***(D)*** *Image of clusters found in the cortex of ConPKO mice 12 months after tamoxifen-induced recombination. The image represents dysplastic tubules of the tumour-like type displayed by some tdTomato-positive cell clusters in the cortex of ConPKO mice.*

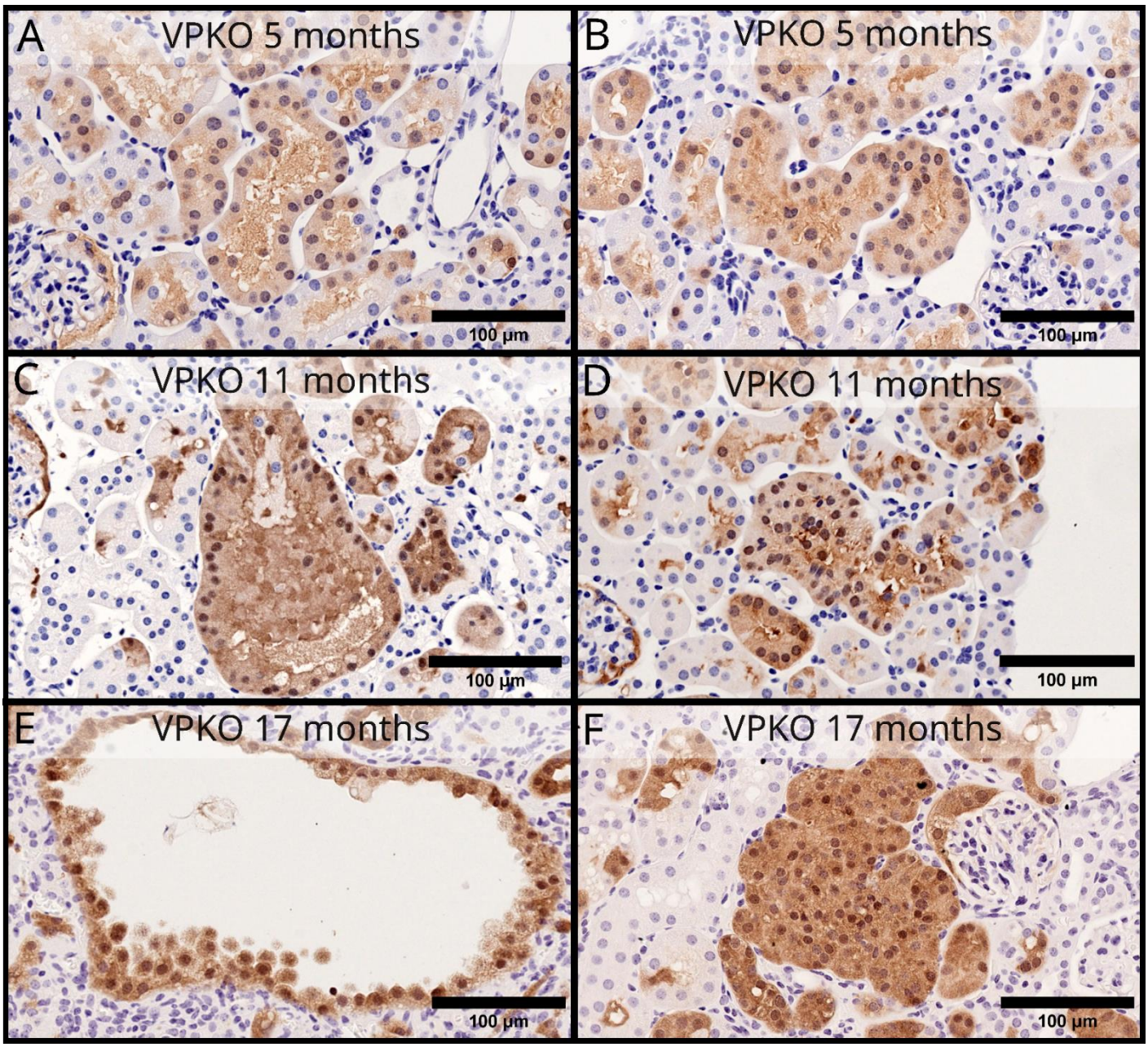

Figure 3.4: Examples of the morphology of tdTomato-positive cell clusters in cortices of VPKO mice: *Exemplar image of tdTomato-positive cell clusters in the cortex of VPKO mice. Image taken of 4µm thick kidney section stained for tdTomato (DAB) and Nuclei (Haematoxylin) with Hamamatsu NanoZoomer S210 at 40x magnification. Representative images are shown of the two distinct populations of tdTomato-positive cell clusters with an altered phenotype (tubule state). Images represent tdTomato-positive dysplastic tubules found in the cortex of VPKO mice 5 months after tamoxifen-induced recombination, representing the cystic tubule type (**A**) and the tumour-like tubule type (**B**). As well as clusters found in the cortex of VPKO mice 12 months after tamoxifen-induced recombination, representing the cystic tubule type (**C**) and the tumour-like tubule type (**D**). Further images display clusters found in the cortex of VPKO mice 17 months after tamoxifen-induced recombination, representing the cystic tubule type (cyst) (**E**) and the tumour-like tubule type (tumorlet) (**F**).*

3.1.3 VPKO cells form larger clusters over time

The formation of larger, abnormal tdTomato-positive clusters in the cortex of VPKO kidneys potentially signifies the early onset of tumour formation. To investigate this, and to quantify the increase in cluster size over time, a workflow for the detection and analysis of DAB-stained, tdTomato-positive clusters was developed. Unlike the HALO® cell detection analysis, this method does not detect individual cells but instead identifies contiguous tdTomato-positive clusters. The digital pathology analysis software QuPath was employed to create a 'neural-network-based pixel classifier.' Using QuPath's 'train pixel classifier' function, a neural network was trained on a set of 10 example images by manually annotating DAB-stained, tdTomato-positive clusters and surrounding tdTomato-negative tissue. This pixel classifier was then able to reliably detect and annotate contiguous tdTomato-positive cell clusters in an automated manner.

The pixel classifier was applied to the cortex of kidney sections from 12 ConKO, 6 ConPKO, 9 VKO, and 8 VPKO mice at the early time point, and 11 ConKO, 8 ConPKO, 8 VKO, and 15 VPKO mice at the late time point, all stained for tdTomato. This allowed for the detection of all contiguous tdTomato-positive clusters consisting of directly adjacent recombined cells. For each genotype and time point, clusters were annotated, nuclei within each cluster were detected, and the detection data were exported for further analysis (Figure 3.5A). This data was then used to analyse cluster formation and changes in cluster size over time in the cortex.

The first step in the analysis involved comparing the mean distribution of cell numbers within contiguous tdTomato signals in the cortex of each genotype and time point. These distributions were visualised as violin plots, scaled logarithmically to ensure consistent representation. At the early time point, the mean distributions of cells within contiguous

tdTomato signals in the cortices of ConKO, ConPKO, VKO, and VPKO kidneys were similar (Figure 3.5B). Most of the detected signals represented single cells or small clusters of 2-8 cells, with only a small fraction of clusters comprising more than 8 cells.

No significant difference was observed when comparing cell distribution between early and late time points in ConKO cortices. In both instances, the majority of tdTomato signals represented single cells, with only a rare occurrence of clusters containing more than 2-8 cells (Figure 3.5B). A similar pattern was observed in ConPKO cortices at the late time point, with no noticeable shift over time and the majority of detections corresponding to single cells or clusters of 2-8 cells (Figure 3.5B).

Interestingly, in VKO cortices, the distribution of cells changed over time, showing a shift towards clusters of 2-8 cells and a reduction in the number of single cells (Figure 3.5B). However, this shift was modest, with no apparent increase in clusters containing more than 8 cells. In contrast, in VPKO cortices at the late time point, the shift was more pronounced with a marked reduction in single cells and a notable increase in clusters containing 2-8 cells. Additionally, the number of clusters with 8-16 cells in VPKO cortices increased over time, a change not observed in any other genotype (Figure 3.5B).

The absence of changes in cell distribution in the ConPKO cortex, paired with only a modest increase in clusters of 2-8 cells in the VKO cortex, suggests that the shift from single cells and small clusters to larger clusters in VPKO kidneys is driven by the concomitant loss of both *Pbrm1* and *Vhl*. Neither *Vhl* loss nor *Pbrm1* loss alone appeared to drive the time-dependent increase in cluster size to the same extent as the concurrent loss of both tumour suppressor genes.

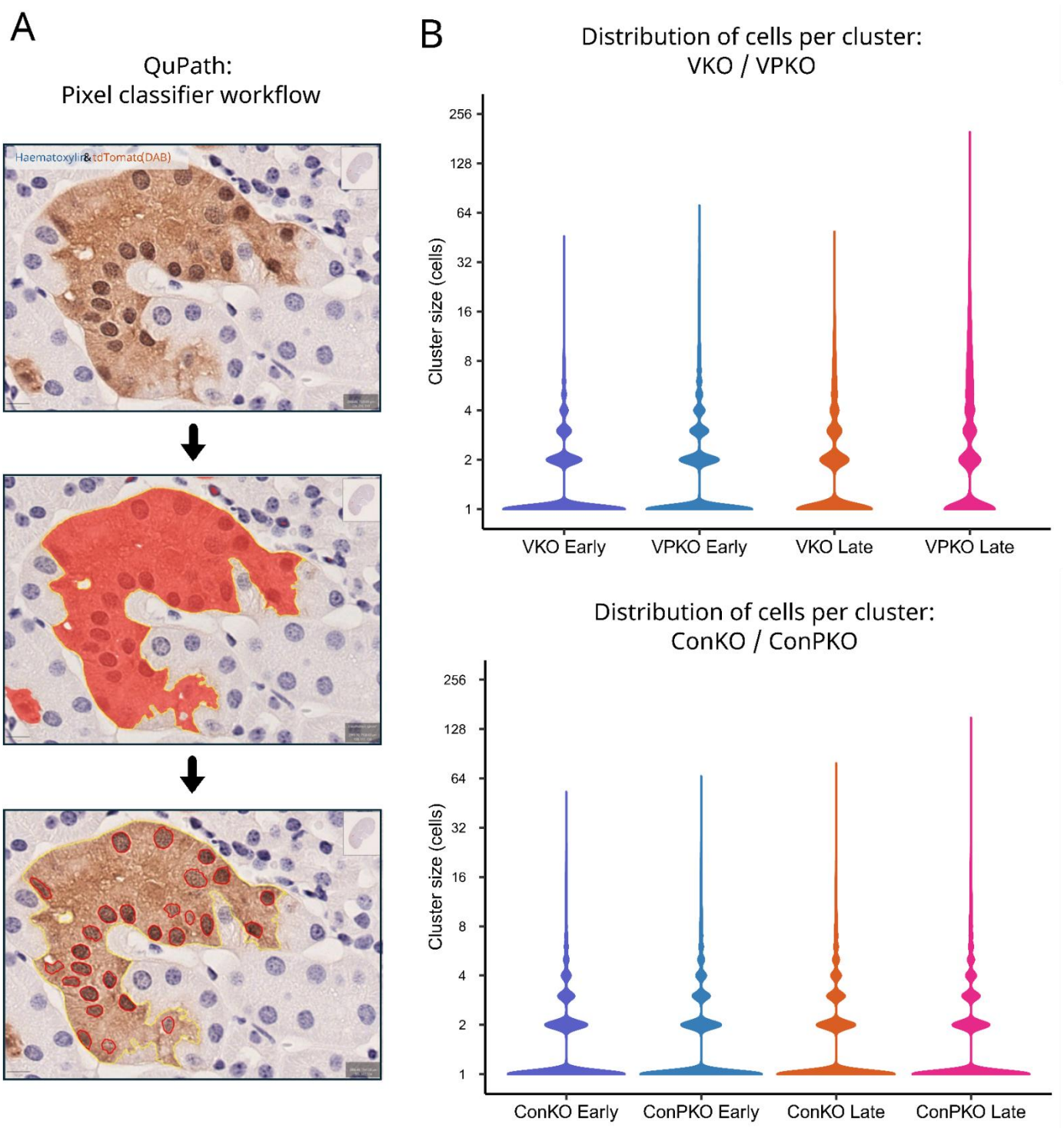

Figure 3.5: Example of QuPath tdTomato-positive cell cluster detection and quantitative display of the distribution of cell number per cluster: (A) *Example of a contiguous DAB-stained, tdTomato-positive cell cluster which is interspaced by tdTomato-negative cells. The red area displays the detected DAB signal by the trained, neuronal network-based cluster classifier. The yellow line around the cluster shows the as a cluster annotated area after being detected by the classifier and the red lines resemble the detected nuclei within the annotated cluster.* ***(B)*** *Contiguous tdTomato-positive clusters were detected by the trained neuronal network-based pixel classifier in QuPath with subsequent cell counting within the annotated clusters. The distribution of cluster size in cell number plotted on a log2 scale for clusters detected in the cortices of 12 ConKO, 6 ConPKO, 9 VKO and 8 VPKO kidney sections at the early time point and 11 ConKO, 8 ConPKO, 8 VKO and 15 VPKO at the late time point. Cluster size in number is plotted as violin plots with the same areas.*

To enable a statistical comparison of the average cluster size in the cortices of ConKO, ConPKO, VKO, and VPKO kidneys, and to assess changes over time, the average number of cells per cluster in each cortex was calculated. At the early time point, the median number of cells per cluster in the cortices of ConKO, ConPKO, VKO, and VPKO kidneys was consistent, with values of 1.905, 2.149, 1.819, and 2.010, respectively, showing no significant differences (Supplementary Figure 3). Similarly, when comparing the mean cluster size between the early and late time points in ConKO, ConPKO, and VKO kidneys, no significant changes were observed, with median values of 2.274 and 1.998 in ConKO and ConPKO, respectively (Figure 3.6).

Interestingly, despite an expansion of *Vhl*-null cells in the renal cortex over time, there was no significant increase in the average number of cells per cluster in the VKO cortex. The median cluster size in VKO cortices increased only slightly, from 1.819 to 2.028, between the early and late time points, which was not statistically significant (Figure 3.6). As anticipated, a significant increase ($p = 0.041$) in the mean number of cells per cluster was observed in the VPKO cortex at the late time point compared to the early time point. The median cluster size increased from 2.010 to 3.100 (Figure 3.6), supporting the hypothesis that the increase in cluster size is driven by the concomitant loss of *Vhl* and *Pbrm1*.

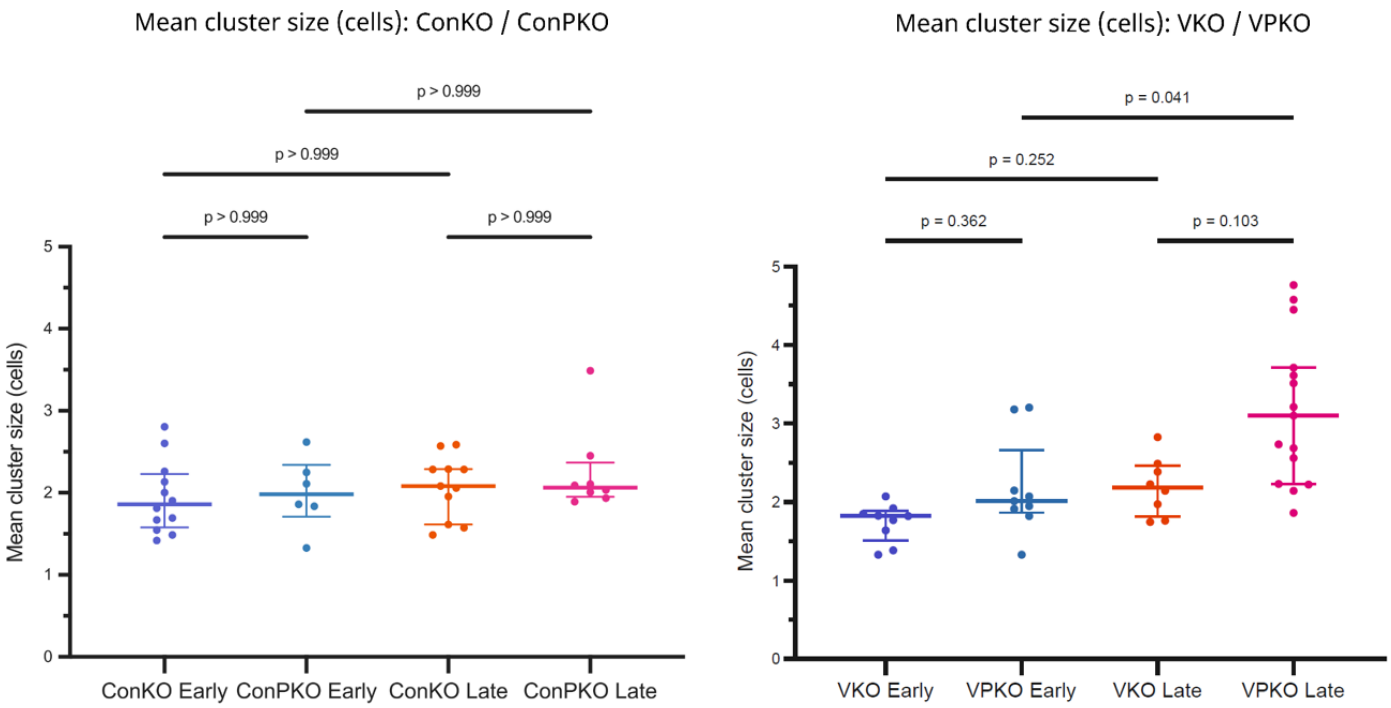

Figure 3.6: Comparison of the mean cluster size in ConKO, ConPKO, VKO and VPKO cortices at the early and late time point: *Contiguous tdTomato-positive clusters were detected by the trained neuronal network-based pixel classifier in QuPath with subsequent cell counting within the annotated clusters. The mean value of the number of cells detected in each cluster in the cortices of 12 ConKO, 6 ConPKO, 9 VKO and 8 VPKO kidney sections at the early time point and 11 ConKO, 8 ConPKO, 8 VKO and 15 VPKO at the late time point. Kidneys were harvested 1-3 weeks (early time point) and >4 months (late time point) after tamoxifen-induced recombination. ANOVA test was used to test for group variability and significance in multiple comparisons was tested using the non-parametric Kruskal-Wallis-test.*

Intriguingly, although a shift in cluster size distribution over time was observed in the cortices of VKO mice in the violin plot (Figure 3.5B), this change was only little reflected in the average number of cells per cluster, particularly when compared to the increase seen in VPKO mice over time (Figure 3.6A). The violin plots at the late time points for VKO and VPKO suggested a rise in the number of larger clusters in the VPKO cortex compared to the VKO cortex. To investigate this, clusters were categorised into three distinct groups: single cells and small clusters (1-5 cells), medium clusters (6-15 cells), and large clusters (15+ cells). The proportions of these groups were then compared between the early and late time points to identify any significant changes.

When analysing the proportions of small, medium, and large clusters in ConKO cortices at both time points, it was evident that the majority were small clusters, with only a minor proportion being medium-sized clusters, and large clusters were nearly absent (Figure 3.7A). These proportions remained consistent over time. In contrast, when comparing clusters in VKO cortices at the early and late time points (Figure 3.7B), the early time points displayed a similar distribution of cluster sizes as seen in ConKO cortices. However, unlike in ConKO cortices, the proportions in VKO cortices changed significantly over time, with a significant decrease ($p = 0.025$) in single cells and small clusters, alongside a significant increase ($p = 0.025$) in medium-sized clusters. The proportion of large clusters in VKO cortices remained unchanged and was still nearly non-existent. Similarly, the comparison of cluster sizes in ConPKO cortices between the early and late time points revealed no changes, with proportions resembling those in ConKO (Figure 3.8A). However, the analysis of VPKO cortices showed a significant decrease ($p = 0.005$) in the proportion of single cells and small clusters over time. Additionally, a significant increase ($p = 0.007$) in the proportion of medium-sized clusters was observed, which exceeded the increase seen in VKO cortices (Figure 3.8B). Moreover, VPKO cortices exhibited a

significant increase ($p = 0.003$) in the proportion of large clusters, a change not observed in any other genotype when comparing early and late time points.

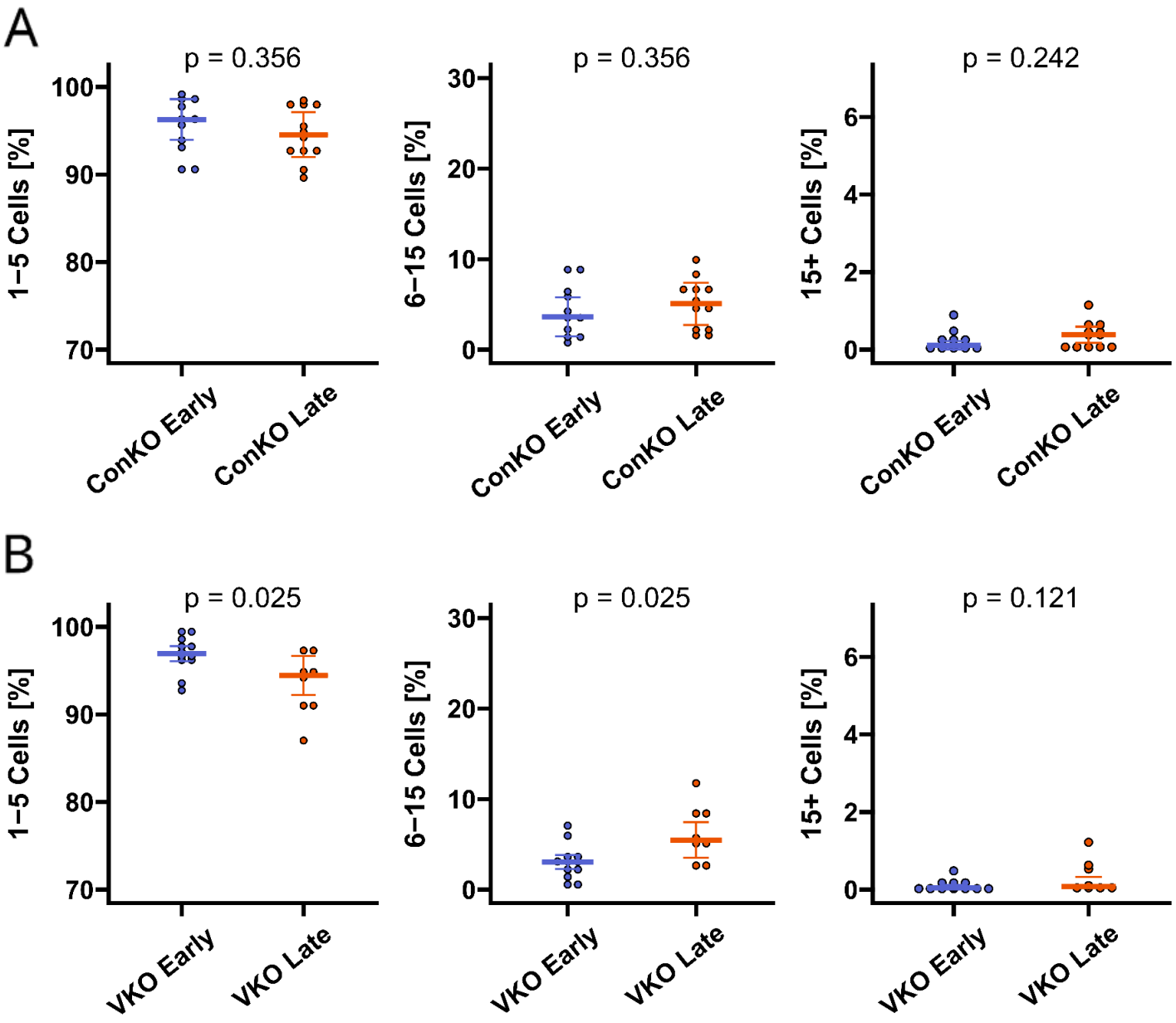

Figure 3.7: Comparing the proportion of small (1-5 cells), medium (6-15 cells) and large (15+ cells) clusters at the early and late time point in the cortex of ConKO and VKO: *Clusters of 1-5 cells, 6-15 cells and 15+ cells were counted in the cortex and divided by the total number of clusters to obtain their proportion. The proportion of the respective tdTomato-positive cluster sizes are displayed as a percentage and compared between 1-3 weeks (Early) and > 4 months (Late) after tamoxifen-induced recombination. Data is shown from clusters detected in* ***(A)*** *12 ConKO Early and 11 ConKO Late as well as* ***(B)*** *9 VKO Early and 8 VKO Late. Significance was tested using the non-parametric Kruskal-Wallis test.*

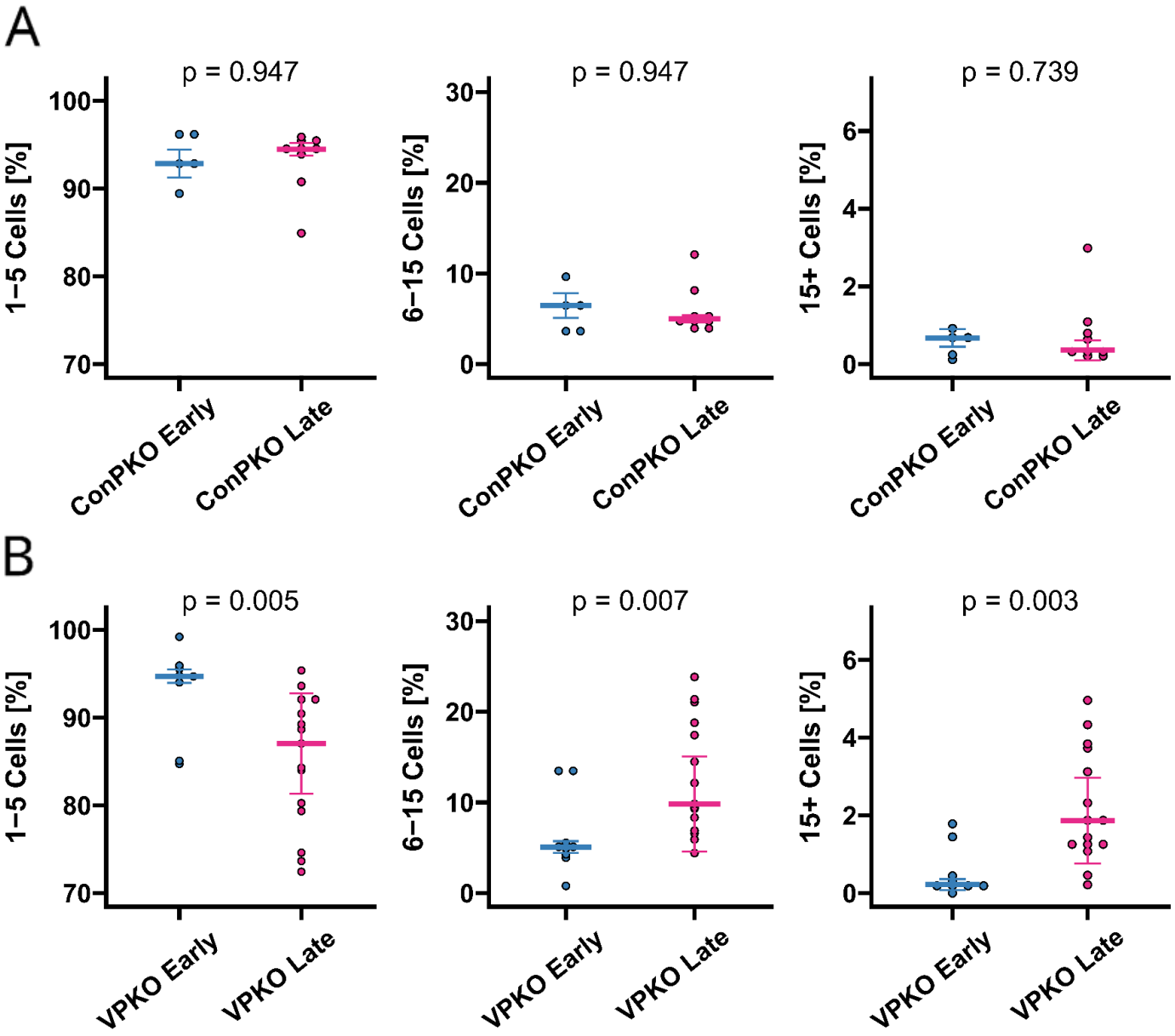

Figure 3.8: Comparing the proportion of small (1-5 cells), medium (6-15 cells) and large (15+ cells) clusters at the early and late time point in the cortex of ConPKO and VPKO: *Clusters of 1-5 cells, 6-15 cells and 15+ cells were counted in the cortex and divided by the total number of clusters to obtain their proportion. The proportion of the respective tdTomato-positive cluster sizes are displayed as a percentage and compared between 1-3 weeks (Early) and > 4 months (Late) after tamoxifen-induced recombination. Data is shown from clusters detected in (A) 6 ConPKO Early and 8 ConPKO Late as well as (B) 8 VPKO Early and 15 VPKO Late. Significance was tested using the non-parametric Kruskal-Wallis test.*

In summary, a method to detect contiguous tdTomato-positive cells and quantify the size of these clusters was successfully developed. When comparing tdTomato-positive cluster sizes among ConKO, VKO, ConPKO, and VPKO genotypes at early and late time points, the quantification confirmed the changes observed during the visual inspection of stained sections. Specifically, the analysis revealed a significant increase in the average number of cells per contiguous tdTomato-positive cluster in the cortices of VPKO mice. Furthermore, the data showed a significant decrease in the proportion of single cells and small clusters (1-5 cells) over time in the cortices of VKO and VPKO mice. This decrease was more pronounced in VPKO mice and was accompanied by a correspondingly strong and significant increase in the proportion of medium-sized clusters (6-15 cells). Additionally, a significant increase in the proportion of large clusters was observed exclusively in the cortices of VPKO mice, a change not detected in any other genotype.

These findings underscore the necessity of concomitant loss of *Vhl* and *Pbrm1* for the formation of cell clusters that eventually develop into the observed cystic and tumour-like tubules. The data presented demonstrate that the developed QuPath workflow accurately detects and quantifies the phenomena observed during visual inspection of tdTomato-stained kidney sections. This method enables the tracking of early changes in the topology of tdTomato-positive cell clusters and provides a valuable platform for testing the efficacy of potential interventions in the early stages of cluster formation.

3.2 Transcriptome analysis

3.2.1 *Pbrm1* loss in VKO cells only leads to minor changes in the transcriptome

Little is known about the mechanistic background of how concomitant loss of *Vhl* and *Pbrm1* is driving tumorigenesis. The need for the loss of both tumour suppressor genes to form tumours in previous mouse models points towards there being an interaction between *Pbrm1* and *Vhl* loss. Further, only clusters of cells which have lost both *Vhl* and *Pbrm1* displayed the formation of larger tumour-like lesions over time. This suggests that there might be a mechanism that is affected by the loss of *Vhl* and *Pbrm1* causing this change in the phenotype of clusters. The role of *Pbrm1* in the chromatin remodelling complex PBAF suggests that its loss might impact genome availability and therefore gene expression. This modulation of gene expression poses a potential point of interaction between *Vhl* loss and *Pbrm1* loss. Hence, it is of interest to investigate whether the loss of *Pbrm1* is causing changes in the transcriptome of *Vhl*-null renal tubular epithelial cells which could explain the observed change in cluster phenotypes.

RNA sequencing was conducted to determine whether the loss of *Pbrm1* in *Vhl*-null murine renal tubular epithelial cells in vivo results in transcriptomic changes that promote tumorigenesis and the observed alterations in the tdTomato-positive cluster phenotype. RNA for sequencing was extracted from FAC-sorted tdTomato-positive cells from one ConKO, two VKO, and two VPKO kidneys of male mice, 12 months after administering 5 doses of 2 mg tamoxifen. Samvid Kurlekar performed the RNA extraction, subsequent cDNA library preparation, and next-generation sequencing. Following this, detected gene reads were compared between VKO and ConKO, and between VPKO and VKO, to identify differentially

expressed genes, which were filtered using significance criteria (Bonferroni-adjusted p-value < 0.05). The pre-processing of raw RNA reads using DESeq2 was carried out by Ran Li.

In the comparison between VKO and ConKO, 687 significantly upregulated and 355 downregulated genes were identified following *Vhl* loss. As anticipated, HIF1A and HIF2A target genes were among the most differentially regulated genes detected after *Vhl* loss (Figure 3.9A). To examine the genes differentially regulated due to *Pbrm1* loss on a *Vhl*-null background, the transcriptomes of VPKO and VKO were compared. Interestingly, *Pbrm1* loss had only a modest impact on the transcriptome of *Vhl*-null cells, with 105 genes being significantly upregulated and 185 downregulated (Figure 3.9B).

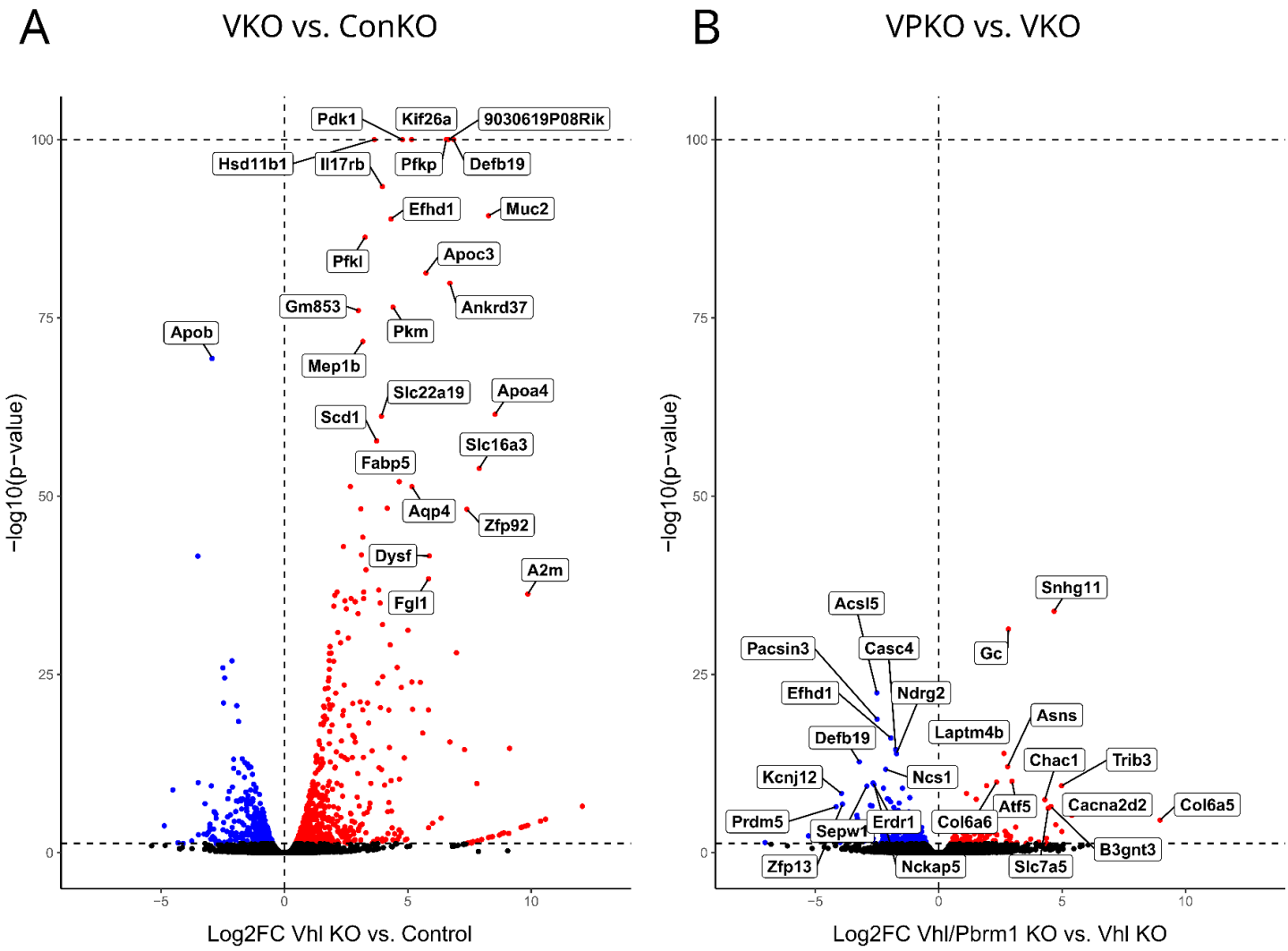

Figure 3.9: Differentially expressed genes after Vhl loss (VKO vs ConKO) and Pbrm1 loss in Vhl-null cells (VPKO vs VKO): *Volcano plots depicting the differential gene expression* ***(A)*** *after Vhl loss (VKO vs. ConKO) and* ***(B)*** *after Pbrm1 loss in Vhl-null cells (VPKO vs. VKO). The Log2 fold change (FC) is plotted against the -log10 of the Bonferroni adjusted p-value of differentially expressed genes detected by RNA sequencing. The significance cut-off value at the y-axis is at 0.05. Downregulated genes (FC <1.2) are marked in blue, and Upregulated genes (FC >1.2) are marked in red. In both volcano plots the top 25 differentially regulated genes, according to a gene score (-log10(p-value) * Log2FC) are labeled with their gene symbol.*

To elucidate the involvement of the detected differentially expressed genes in specific biological pathways, a Kyoto Encyclopedia of Genes and Genomes (KEGG) pathway enrichment analysis was performed. Initially, this analysis was conducted on genes upregulated following the loss of *Vhl* (VKO *vs* ConKO) as a positive control, with the expectation of identifying pathways associated with the stabilisation of HIF1A and HIF2A (Figure 3.10). As anticipated, the analysis revealed significant enrichment of the HIF1A signalling pathway ($q = 1.11 \cdot 10^{-6}$), alongside several metabolic pathways. Notably, glycolysis/gluconeogenesis ($q = 1.79 \cdot 10^{-8}$), carbon metabolism ($q = 4.19 \cdot 10^{-5}$), central carbon metabolism in cancer ($q = 1.59 \cdot 10^{-6}$), and fructose and mannose metabolism ($q = 5.85 \cdot 10^{-6}$) were among the most significantly enriched pathways.

Further KEGG pathway enrichment analysis was then performed on differentially expressed genes upregulated and downregulated following the loss of *Pbrm1* in *Vhl*-null cells. No significant pathway enrichment was observed among the downregulated genes. However, five pathways were significantly enriched in the upregulated genes, with the most prominent being focal adhesion ($q = 4.22 \cdot 10^{-2}$) and cell adhesion molecules ($q = 4.33 \cdot 10^{-2}$) (Figure 3.11).

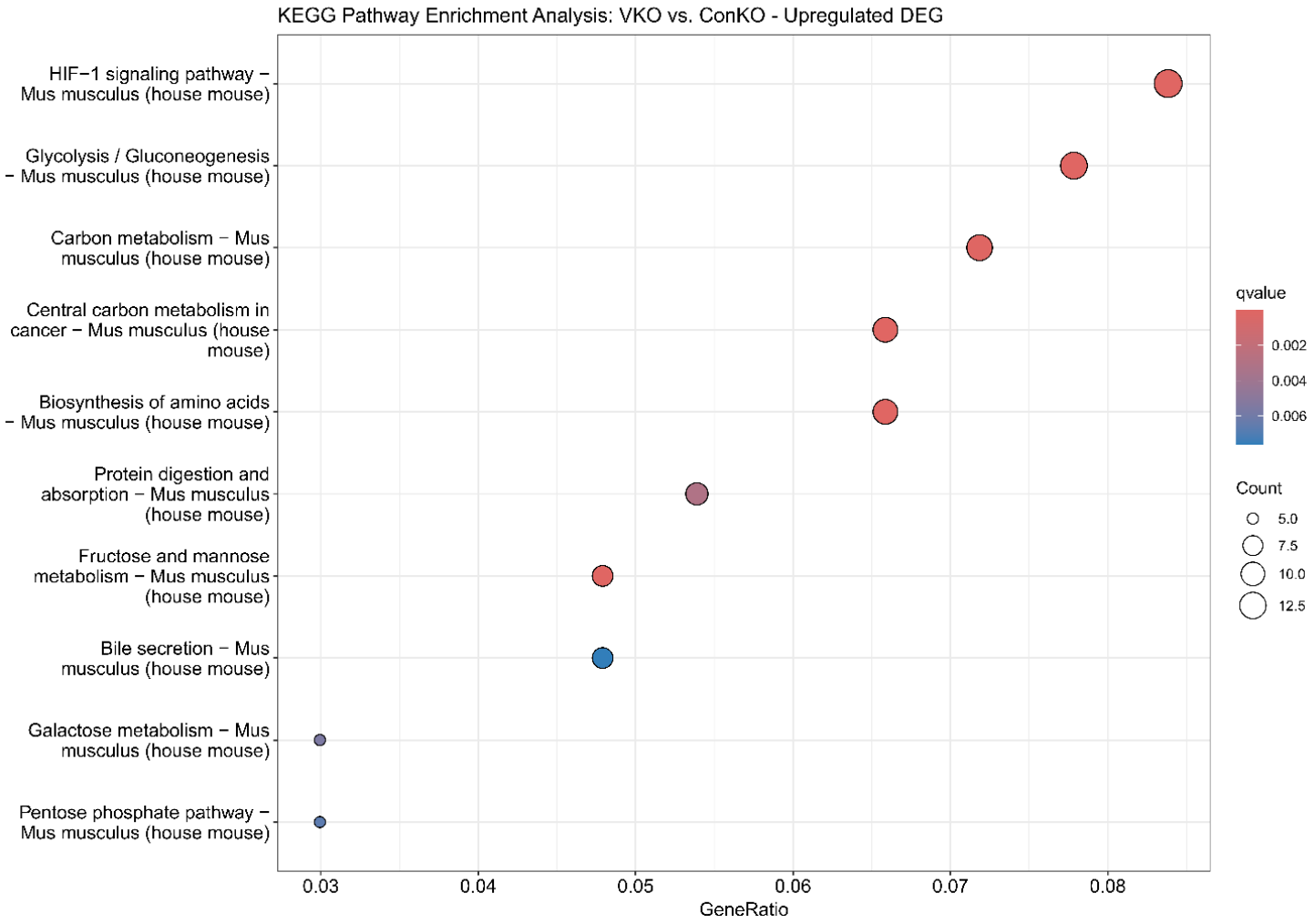

Figure 3.10: KEGG Pathway Enrichment Analysis of genes upregulated in VKO vs ConKO: *Kyoto Encyclopedia of Genes and Genomes (KEGG) pathway enrichment analysis was conducted on the significantly upregulated genes (p-value < 0.05, log2FC > 1.2) of VKO vs ConKO. The dot plot represents the 10 most overrepresented KEGG pathways ordered by their GeneRatio (number of genes mapped to KEGG pathway divided by the total number of genes). The colours of the dots represent the q-value (Benjamini-Hochberg adjusted p-value) and the size of the dots represents the gene count (number of genes mapped to KEGG pathway)*

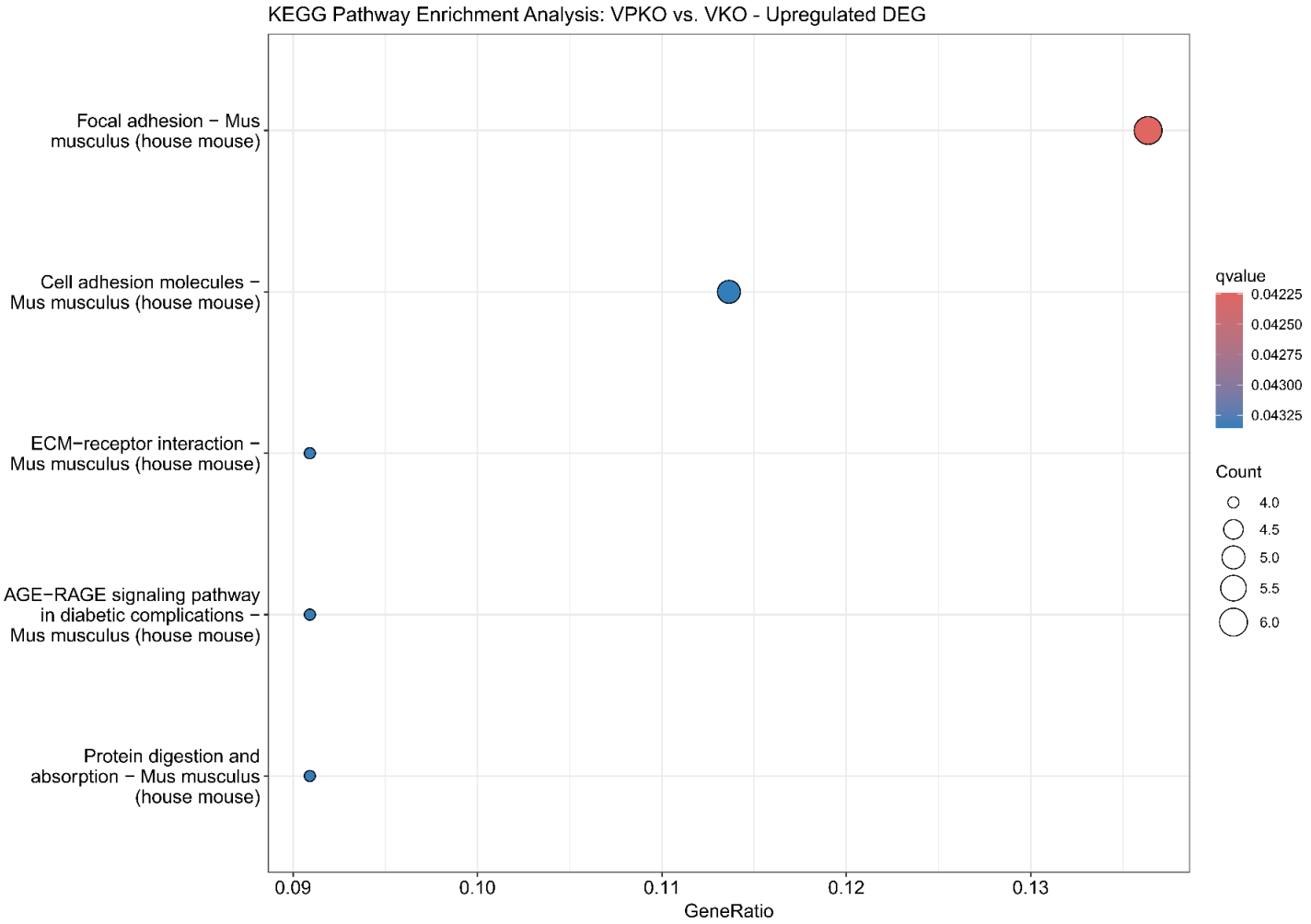

Figure 3.11: KEGG Pathway Enrichment Analysis of genes upregulated in VPKO vs VKO: *Kyoto Encyclopedia of Genes and Genomes (KEGG) pathway enrichment analysis was conducted on the significantly upregulated genes (p-value < 0.05, log2FC > 1.2) of VPKO vs. VKO. The dot plot represents the 5 overrepresented KEGG pathways ordered by their GeneRatio (number of genes mapped to KEGG pathway divided by the total number of genes). The colours of the dots represent the q-value (Benjamini-Hochberg adjusted p-value) and the size of the dots represents the gene count (number of genes mapped to KEGG pathway)*

To investigate the hypothesised interaction between *Vhl* and *Pbrm1* loss reflected in the transcriptome, differentially expressed genes from both comparisons were analysed using a scatterplot (Figure 3.12). The analysis revealed that the majority of significant genes were regulated either by the loss of *Vhl* or by the loss of *Pbrm1*, with minimal influence from the concurrent loss of both genes. This finding does not support the hypothesis of a broad interaction between *Vhl* and *Pbrm1* loss at the transcriptomic level. Only a small subset of genes were differentially regulated in both comparisons, with most genes upregulated by *Vhl* loss and downregulated by *Pbrm1* loss.

In summary, the analysis demonstrated that *Vhl* loss resulted in the upregulation of more genes (687) than downregulation (355). Conversely, when Pbrm1 was lost in *Vhl*-null cells, more genes were downregulated (185) than upregulated (105). Interestingly, the loss of *Pbrm1* in *Vhl*-null cells led to only minor changes in the overall transcriptome. KEGG pathway enrichment analysis identified Focal Adhesion and Cell Adhesion Molecules as pathways affected by genes upregulated following *Pbrm1* loss. Interestingly, Cell Adhesion Molecules included vascular cell adhesion molecule 1 (*Vcam1),* a cell adhesion molecule commonly found to be upregulated in ccRCC tumours. The downregulation of genes due to *Pbrm1* loss did not significantly impact any specific pathway. The investigation into the effects of *Vhl* and *Pbrm1* loss revealed that most genes were influenced by the loss of only one tumour suppressor gene. Among the genes differentially expressed under both conditions, the majority were initially upregulated following *Vhl* loss and subsequently downregulated after Pbrm1 loss. Preliminary downstream analysis of the transcriptomic changes induced by *Pbrm1* loss in *Vhl*-null cells provided no clear insights into the mechanisms driving the observed morphological and topological alterations in tdTomato-positive cell clusters.

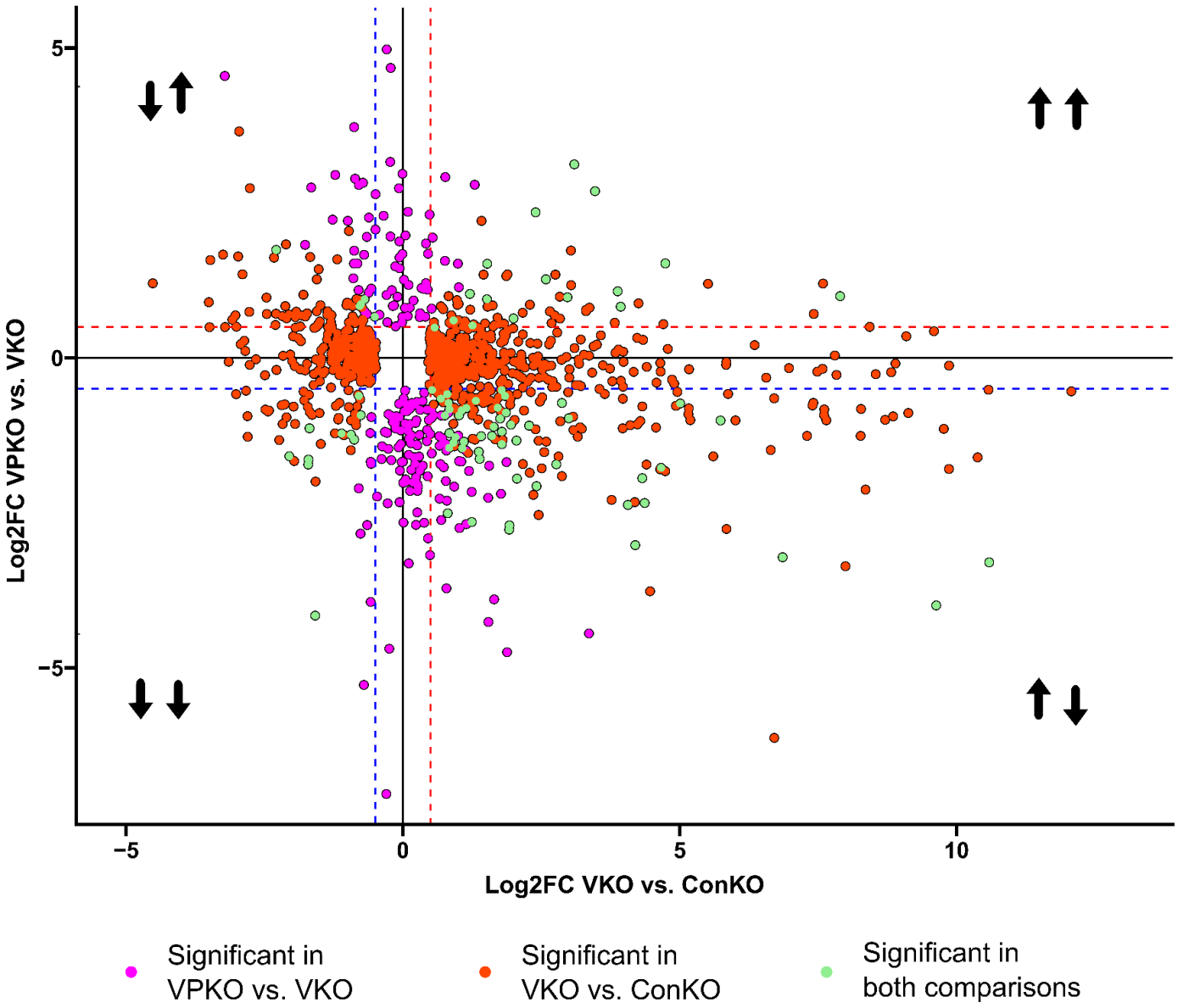

Figure 3.12: Differentially expressed genes upon Vhl loss and Pbrm1 loss in Vhl-null cells: *Genes found to be significantly differentially expressed (adjusted p-value < 0.05) in either VKO vs ConKO or VPKO vs VKO comparisons plotted according to the respective Log2FC (Fold change). Cut-off lines represent Log2FC = -0.5 (blue) and Log2FC = 0.5 (red). Dot coloured in purple were found to be significantly differentially regulated (adjusted p-value < 0.05) in VPKO vs. VKO, dots coloured in orange were found to be significantly differentially regulated (adjusted p-value < 0.05) in VKO vs ConKO and dots in green were significantly differentially regulated (adjusted p-value < 0.05) in both comparisons. Arrows in the four quadrants indicate the respective direction of up- or downregulation: the first arrow stand for the direction of regulation in VKO vs ConKO and the second arrow for the direction of regulation in VPKO vs VKO. Arrow pointing up indicates upregulation and an arrow pointing down indicates downregulation.*

3.2.2 *Pbrm1* loss in *Vhl*-null renal tubular epithelial cells leads to differential expression of HIF1A and HIF2A target genes

The differential gene expression analysis did not reveal the anticipated broad interaction between *Vhl* and *Pbrm1* loss within the transcriptome. This raises the question of how the concomitant loss of both genes leads to the observed morphological changes in tdTomato-positive clusters. Despite the limited overlap between genes differentially regulated by *Vhl* and *Pbrm1* loss, the shared differential regulation of a few key genes might give hints towards a potential mechanism of interaction. Given that *Vhl* loss activates several pro-tumorigenic pathways through the stabilisation of HIF1A and HIF2A, I sought to determine whether specific alterations in the HIF pathway due to *Pbrm1* loss could explain the observed morphological changes.

To explore potential alterations in the HIF pathways, genes differentially expressed following *Vhl* loss and additional *Pbrm1* loss were categorised into four groups. These groups are represented in Venn diagrams, with the intersections highlighting genes that were upregulated in both conditions (Figure 3.13A), downregulated in both conditions (Figure 3.13B), upregulated in VKO and downregulated in VPKO (Figure 3.13C), as well as downregulated in VKO and upregulated in VPKO (Figure 3.13D). A corresponding gene list is provided for each intersection, showcasing the differentially expressed genes identified. These gene lists were subsequently compared to a previously published general HIF target gene list (54), as well as to unpublished HIF1A-specific and HIF2A-specific target gene lists (Table 3.1). The latter two lists were obtained by Samvid Kurlekar and Joanna Lima, who conducted scRNA sequencing experiments using a similar mouse model as previously published (14). In these experiments, the VKO mouse model was extended to include *Hif1a* and/or *Epas1* (gene coding

for HIF2A) knockouts, and scRNA sequencing was performed on tdTomato-positive cells (Table 3.1).

Table 3.1: HIF1A and HIF2A target genes: *List of genes that were upregulated after Vhl loss. Additionally, compared to Vhl-null cells, genes were downregulated upon Vhl/Hif1a loss (HIF1A targets) or downregulated after Vhl/Epas1 loss (HIF2A targets) in scRNA-seq data of ex-vivo murine tubular epithelial cells. (According to experiments done by Joanna Lima and Samvid Kurlekar)*

HIF1A targets		HIF2A targets		
Acsm3	Pdk1	Defb19	Fabp5	Ipo5
Ctnnbip1	Ly6e	Apoc3	Gls	Acmsd
Gpi1	Pfkl	Angptl3	Efhd1	Pabpc1
Pgam1	Mif	Napsa	Mep1a	Me1
Pgk1	Dhx29	Odc1	Egln3	Rpl22l1
Bnip3		Adh1	Tmigd1	Ldc1
Fam162a		Kap	Agps	

When comparing genes upregulated following *Vhl* loss with those further upregulated after *Pbrm1* loss, 16 genes were identified as being commonly upregulated under both conditions. Among these, three genes *Aldoc*, *Cp*, and *Maff* were included in the general HIF target gene list and have been previously characterised as HIF1A target genes in the literature (55–57) (Figure 3.13A). Additionally, two of the 16 genes *Fam162a* and *Ctnnbip1* were found in the HIF1A-specific target gene list.

Further analysis revealed that 10 genes were downregulated in common in VPKO VKO (Figure 3.13B), and five genes were upregulated in VPKO after being downregulated in VKO (Figure 3.13C). None of these genes were present in any of the HIF target gene lists. Notably, the majority of common differentially expressed genes were upregulated in VKO and downregulated in VPKO (Figure 3.13D). Among these 50 genes, nine were identified as HIF

target genes, with five classified as general HIF targets and four, namely *Efhd1*, *Defb19*, *Apoc3,* and *Ipo3* specifically regulated by HIF2A (Figure 3.13D). These findings raise the question of whether *Pbrm1* loss selectively alters the expression of HIF1A and HIF2A target genes, potentially promoting the expression of HIF1A targets while repressing HIF2A targets.

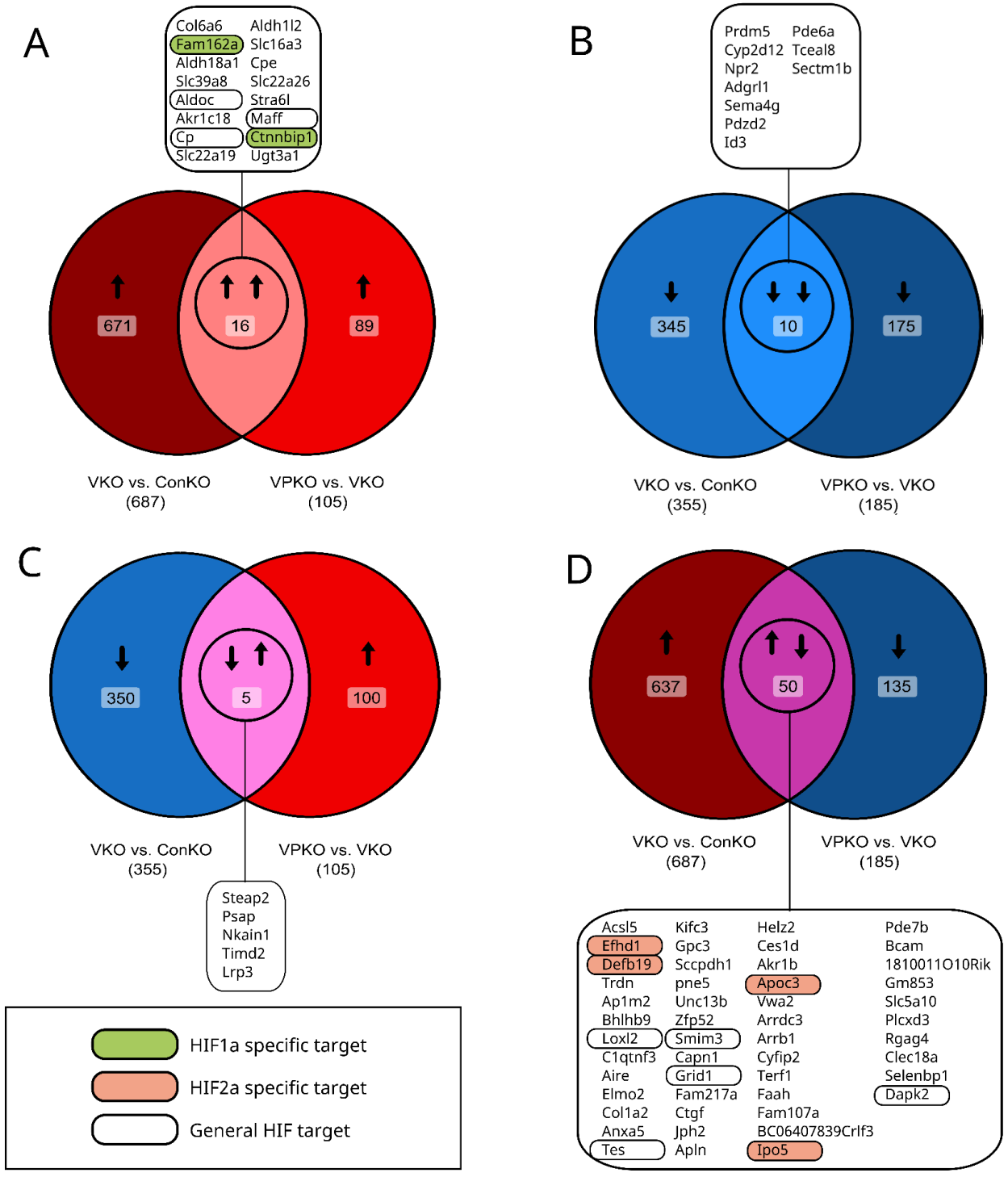

Figure 3.13: Comparison of significantly up and downregulated genes in VKO vs ConKO with VPKO vs VKO: *Differentially expressed genes VKO vs. ConKO and VPKO vs. VKO are separated in upregulated (Log2FC > 0.5) and downregulated (Log2FC < 0.5) genes and compared to each other. Each intersection represents genes found in both comparisons. Genes in each intersection are labelled in the boxes below with their respective gene symbol. Genes found to be HIF1A (green) or HIF2A (salmon) target genes according to the gene list in Table 1 are highlighted. General HIF target genes according to Lombardi et al. are marked with a box with a white background. Comparisons shown are in **A** genes upregulated in both VKO vs. ConKO (687) and VPKO vs. VKO (105), in **B** genes downregulated in both VKO vs. ConKO (355) and VPKO vs. VKO (185), in **C** genes downregulated in VKO vs. ConKO (355) and upregulated in VPKO vs. VKO (105), and in **D** genes upregulated in VKO vs. ConKO (687) and downregulated in VPKO vs VKO (185).*

To investigate whether HIF1A and HIF2A target genes are differentially regulated following *Pbrm1* loss in *Vhl*-null cells, gene set enrichment analysis using a previously defined list of specific HIF1A and HIF2A target genes (Table 3.1) was conducted. The regulation of these genes was compared upon *Vhl* loss and additional *Pbrm1* loss by ranking genes according to their log2 fold change (FC) values and plotting the positions of HIF1A and HIF2A target genes as the proportion of the gene set recovered.

Initially, upon *Vhl* loss, both HIF1A and HIF2A target genes were upregulated, displaying a shift towards positive log2FC values (Figure 3.14A). However, this trend was disrupted following the additional loss of *Pbrm1*. Specifically, while HIF1A target genes predominantly remained on the right side of the plot, indicating no substantial change or modest upregulation, most HIF2A target genes shifted towards the left, indicating negative log2FC values. Notably, five HIF2A target genes were modestly upregulated, whereas 14 out of 19 showed significant to moderate downregulation (Figure 3.14B).

To further analyse the expression of HIF1A and HIF2A target genes across ConKO, VKO, and VPKO conditions, a z-score was calculated from normalised read counts detected in each condition for each gene (z-score: $z = (x-\mu)/\sigma$, x: read count, μ: population mean, σ: population standard deviation). Subsequently, hierarchical clustering was performed for each gene according to the change in z-score in each condition (ConKO/VKO/VPKO) (Figure 10C). This analysis revealed two distinct clusters of genes with similar expression patterns. Cluster 1 included genes upregulated following *Vhl* loss that remained upregulated or showed further upregulation upon additional *Pbrm1* loss. This cluster contained all the detected HIF1A target genes and a few HIF2A target genes. Conversely, Cluster 2 comprised genes upregulated after *Vhl* loss but downregulated after *Pbrm1* loss, consisting exclusively of HIF2A target genes.

These findings suggest a differential regulation of HIF1A and HIF2A target genes following *Pbrm1* loss in *Vhl*-null cells. Gene set enrichment analysis indicated that most HIF2A

target genes shifted towards downregulation, while HIF1A target genes remained relatively constant or showed slight further upregulation. Although the downregulation of some HIF2A target genes was modest, it was more pronounced for others. A direct comparison of normalised read counts in the heatmap (Figure 3.14C) showed that genes such as *Defb19* and *Efhd1* were downregulated to levels similar to those in the ConKO control. Whether this effect is due to changes in genome accessibility following *Pbrm1* loss or alterations in HIF1A and HIF2A protein levels remains to be determined.

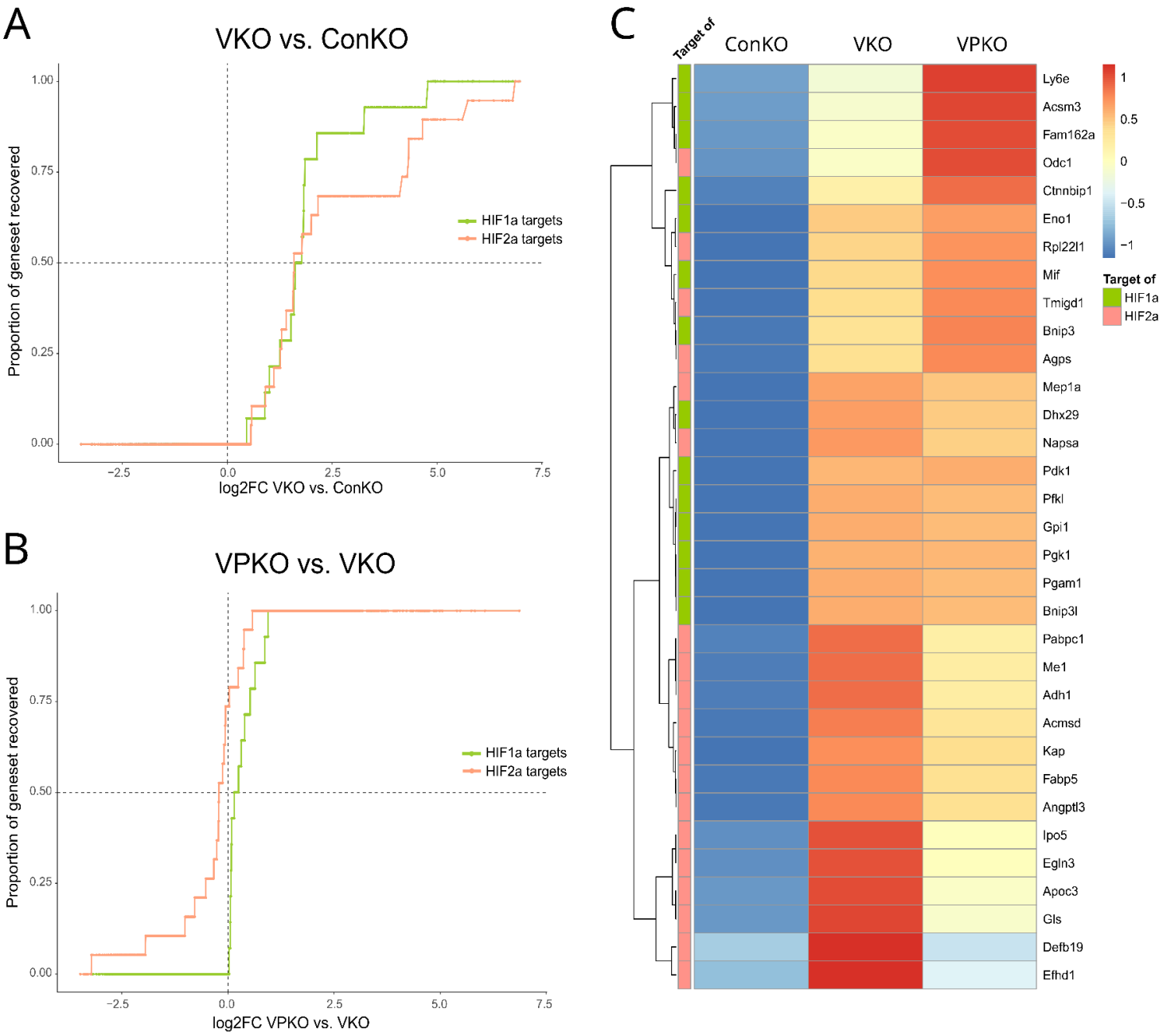

Figure 3.14: Gene set enrichment analysis of HIF1A and HIF2A target genes: *Gene set enrichment analysis was conducted on HIF1A (green) and HIF2A (salmon) target genes (Table 1) by ranking all detected genes in* ***(A)*** *VKO vs. ConKO and* ***(B)*** *VPKO vs. VKO according to their log2FC on the x-axis. This was plotted against the proportion of gene set recovered (1/total number of HIF1A or HIF2A target genes) to have every increment along the x-axis represent the position of a HIF1A or HIF2A target gene.* ***(C)*** *The heatmap represents all HIF1A and HIF2A target genes ordered according to their gene expression patterns in a unsupervised clustering. The read counts of each HIF1A or HIF2A target gene in each replica was averaged and normalized over all three conditions (ConKO + VKO + VPKO = 0). HIF1A (green) and HIF2A (salmon) target genes were labelled accordingly.*

4. Discussion

This study aimed to describe and quantify the expansion and morphological changes that have been observed over time in the tubular epithelial cells in the renal cortex of mice following the concomitant deletion of *Vhl* and *Pbrm1* and to compare these with the loss of *Vhl* and *Pbrm1* alone. Further, the aim was to elucidate why morphological changes are occurring in *Vhl/Pbrm1*-null renal tubular epithelial cells and whether these changes can be explained by alteration of the transcriptome compared to *Vhl*-null cells. To do so, a mouse model was utilised which couples the conditional inactivation of *Vhl* in the renal tubular epithelium to the expression of a tdTomato reporter. This model was expanded for the biallelic loss of *Pbrm1* to investigate the effects of concomitant *Vhl* and *Pbrm1* loss. This model enabled the visualisation and extraction of *Vhl/Pbrm1*-null cells before they underwent morphological transformation.

The results of the histological analysis suggest that while the loss of *Pbrm1* does not alter the previously reported expansion of *Vhl*-null cells in the renal cortex, as indicated through tdTomato staining *Pbrm1* loss is responsible for morphological alteration of recombined cell clusters. The simultaneous loss of both genes leads to a marked, quantifiable increase in cluster size and the emergence of two distinct morphologies of dysplastic tubules: tumour-like and cystic tubules. Interestingly, it was shown that *Pbrm1* loss in combination with monoallelic loss of *Vhl* already leads to morphological alteration of recombined cell cluster morphology which has not been reported before.

Surprisingly, transcriptome analysis has yielded only minor changes in *Vhl*-null cells upon the loss of *Pbrm1*, indicating only little difference in the gene expression of *Vhl*-null and *Vhl/Pbrm1*-null cells. Among the few differentially regulated genes associated with *Pbrm1* loss in *Vhl*-null cells, more were downregulated than upregulated. Additionally, it was shown that

HIF1A and HIF2A target gene expression is affected differently by the loss of *Pbrm1*, causing HIF1A targets to be stable or upregulated and HIF2A targets to be downregulated.

4.1 *Pbrm1* loss does not impact the overall expansion of *Vhl*-null cells in the renal cortex

Previous studies using this model have established that *Vhl* loss in the renal tubular epithelium leads to an increase in tdTomato-positive cells in the renal cortex over time, without apparent morphological changes (14). Consistent with these findings, the current study confirmed that *Vhl*-null cells (VKO) exhibited a modest but statistically significant increase in their number as a proportion of all cells in the renal cortex over time. However, the concomitant loss of *Pbrm1* (VPKO) did not enhance nor dampen this expansion, suggesting that *Pbrm1* loss alone does not directly influence the expansion or survival of *Vhl*-null cells in the renal cortex. Further, the loss of *Pbrm1* in cells with monoallelic *Vhl* loss (ConPKO) mimicked the behaviour of cells with monoallelic *Vhl* loss (ConKO) in the renal cortex, not showing any change in the number of cells as a proportion of all cortical cells over time.

The observed increase in tdTomato-positive cells in VKO and VPKO mice is likely driven by the disruption of the VHL-HIF pathway, which is known to regulate cellular responses to hypoxia, including angiogenesis, cell survival, and metabolism (2). Previous work on primary cultures of renal proximal epithelial cells supports these findings by showing that *VHL* loss does lead to senescence but only under atmospheric oxygen levels (21%) and not under physiological oxygen levels (5%) as found in the renal cortex (58–60). Further evidence for a positive effect of *VHL*-loss on proliferation in human renal proximal tubule epithelial cells (RPTEC) is brought by *in vitro* experiments in which *VHL*-null RPTEC cells showed growth despite confluency whereas cells expressing wild-type *VHL* showed limited growth (61).

Moreover, these findings are in line with data obtained from biopsies of ccRCC patients in which normal tumour adjacent tissue was stained for CAIX, a gene commonly overexpressed in ccRCC and a HIF1A target gene. Here, only cells of the renal cortex but not cells of other kidney layers stained positive for CAIX (62–64). The lack of a significant difference between VKO and VPKO at the late time point in terms of tdTomato-positive cell proportions suggests that *Pbrm1*, although involved in chromatin remodelling and potentially gene expression regulation (3), does not contribute to cell expansion or survival of *Vhl*-null cells in this context. These findings stand in contrast to earlier work done *in vitro* which indicates that upon reintroduction of *PBRM1* into *PBRM1*-null ACHN ccRCC cell lines cell cycle progression is altered and proliferation is inhibited through interaction with a chemokine/chemokine receptor (65). Additionally, MYC-driven proliferation has been suggested as a potential interaction between *VHL* loss, which stabilises MYC, and *PBRM1* loss which represses the epithelial-differentiation program that otherwise dominantly antagonises MYC (66).

This study clearly showed that *Pbrm1* loss does not affect the survival and expansion of *Vhl*-null renal tubular epithelial cells in the cortex. Although proliferative effects of *PBRM1* loss have been reported in ccRCC cell lines, these findings were not supported. This could potentially be owed to the fact that renal tubular epithelial cells in this study have not yet progressed to ccRCC and proliferation might be restricted by the tubular boundaries in the cells native environment. A caveat of this study is the inability to identify cell-type-specific effects in the renal tubular epithelial cell population within the cortex. Here, concomitant loss of *Vhl* and *Pbrm1* might also have different effects on proximal or distal tubular cells. The identification and the analysis of cell survival and expansion over time with respect to different epithelial cell types in the renal cortex might give more inside into the origin and early progression of ccRCC and should be subject of further investigation.

4.2 VPKO and ConPKO mice exhibit morphological abnormalities in the renal cortex

One of the most striking findings of this study is the morphological alterations observed in the renal cortex of VPKO and ConPKO mice over time. While VKO mice displayed an increase in the proportion of recombined cells in the cortex, similar to the expansion of VPKO cells, these cells did not exhibit apparent morphological abnormalities such as cystic and tumour-like tubules (Figure 3.3B). In contrast, VPKO mice developed clusters of tdTomato-positive cells along the cross-section of tubules which displayed an increasingly dysplastic morphology, cystic dilation or tumour-like accumulation of cells over time (Figure 3.4). Interestingly, similar morphological abnormalities were found in the cortex of ConPKO mice although not as commonly or as early as in VPKO mice (Figure 3.3C, D).

In the cortex of ConPKO mice, morphological abnormalities were detected by visual inspection 12 months after tamoxifen-induced recombination. These morphological abnormalities occurred in the cross-section of tubules in clusters consisting primarily of tdTomato-positive cells which are occasionally interspaced by tdTomato-negative cells. The tubules tend to either display a cystic phenotype with a dilated lumen and an intact epithelial monolayer (Figure 3.3C) or a tumour-like phenotype with crowded cells and disrupted epithelial monolayer (Figure 3.3D).

In contrast, early changes in the cortex of VPKO mice are observed as early as 5 months after tamoxifen supplementation in clusters of cells that are nearly exclusively stained for tdTomato. These dysplastic tubules can be classified into two distinct phenotypes, namely tumour-like and cystic tubule-type lesions. Tumour-like lesions were characterised by cells densely packed extending beyond the epithelial monolayer, alongside evidence of cellular displacement where epithelial cells appear to detach from the tubular basement membrane and

migrate or are displaced towards the tubular lumen which might indicate a dysregulation of cell adhesion (Figure 3.4). After 17 months these tumour-like cysts likely progressed to clear cell renal cell carcinoma (ccRCC)-like tumourlets. Alongside tumour-like lesions visual inspection found dysplastic lesions which resembled the early development of cysts. These cystic-type tubules were characterised by cystic dilation of the tubular lumen while mostly retaining the epithelial monolayer (Figure 3.4). This type of lesion likely progresses to full cysts over the course of 17 months. The morphological changes observed in VPKO mice, such as the formation of cystic tubules and tumour-like lesions, likely represent the early stages of tumorigenesis. The formation of tdTomato-positive, tumour-like lesions supports the hypothesis that *Pbrm1* functions as a tumour suppressor in the kidney, and its loss cooperates with *Vhl* loss to promote malignant transformation.

The findings in VPKO mice align with previous reports suggesting that *Pbrm1* loss, in conjunction with *Vhl* loss, is required for the formation of ccRCC-like lesions (11–14,37). These reports have studied the concomitant loss of *Vhl* and *Pbrm1* by Cre-recombinase targeted to the renal tubular epithelium (RTE) *in vivo* in a similar fashion as done in this study. One study reports progressive cystic abnormalities and nodular abnormalities with a decreased cystic appearance in knock-out mice after 8-17 months where the inactivation of genes was driven by constitutive *Ksp-Cre* (11). Similarly to this study, biallelic inactivation of *Vhl* and *Pbrm1* was induced in the renal tubular epithelium yet also in other cells like collecting ducts and thick ascending limbs of Henle's loops. Further, *Ksp-Cre* will start expression in the developing kidney *in utero* inducing the loss of *Vhl* and *Pbrm1* much earlier in life compared to when the loss occurs in real-life ccRCC patients (67). Another comparable study using constitutive *Pax8-Cre* to induce *Vhl/Pbrm1* loss in the renal tubular epithelium reported the formation of cysts and ccRCC-like tumours (13). Here *Pax8-Cre* is constitutively expressed which leads to the inactivation of *Vhl* and *Pbrm1 in utero* as well holding the same caveats of early inactivation

comparable to *Ksp-Cre* driven inactivation (68). A third study utilising an inducible *Pax8-CreER*^{T2}-driven knock-out mouse model, which was induced by 5x 2 mg tamoxifen supplementation, as done in this study, reported the formation of cysts and multifocal neoplastic tumours 20 months after recombination (12).

In contrast to these studies, which relied on the Cre-mediated homozygous knock-out of *Vhl* (*Vhl*$^{fl/fl}$), this study utilises mice that have inherited one inactive copy of *Vhl* (*Vhl*$^{iae.KO}$). This leads to conditions during development and up to the tamoxifen-induced recombination which models ccRCC caused by inherited *Vhl* disease more closely. The benefit of this study is that as opposed to simultaneous inactivation of both *Vhl* alleles, which is unlikely, the inheritance of one inactive *Vhl* allele and the inactivation of the other allele later in life as occurs clinically in VHL disease (69).

Interestingly, these studies have not reported any morphological abnormalities upon the loss of *Pbrm1* in combination with monoallelic *Vhl* loss in the renal tubular epithelium. This could be because these abnormalities in the cortex of ConPKO were relatively subtle as opposed to the lesions observed in the cortices of VPKO mice. In this study, the successful identification of lesions in cortices of ConPKO mice is owed to the induction of the fluorescent tdTomato marker gene in cells carrying the respective knock-out. This enabled the identification of small, early morphological abnormalities in stained tissue sections of VPKO mice as early as 5 months and in ConPKO mice as early as 12 months after tamoxifen-induced recombination. Of note is that this marking of recombined cells potentially brings a positive bias toward identifying tdTomato-positive abnormalities and might lead to tdTomato-negative abnormalities being missed during visual inspection. However, all observed lesions found were comprised mostly of tdTomato-positive cells. Since tdTomato-positivity has been confirmed to indicate concomitant *Vhl/Pbrm1*-loss in VPKO mice by immunoblotting and immunostaining (Figure 1.5B & 1.5C), we can confidently deduce that the formation of these lesions is a product of

concomitant *Vhl/Pbrm1*-loss. The presence of morphological abnormalities in VPKO mice as early as 5 months post-recombination suggests that the loss of both *Vhl* and *Pbrm1* creates a permissive environment for early tumour formation, even before the appearance of fully developed tumours. Importantly, in VPKO and ConPKO mice, only a few morphological abnormalities in the bowman capsule were observed with no difference between VPKO and ConPKO. This is contrary to the reports of previous studies which observed glomerular cysts following *Vhl* and *Pbrm1* loss. This challenges the hypothesis of parietal cells of the bowman capsule as cells-of-origin of ccRCC.

In summary, this study was able to reproduce the formation of cysts and tumour-like abnormalities when inactivating *Vhl* and *Pbrm1* in the renal tubular epithelium. These abnormalities were exclusively limited to the renal cortex and dysplastic tubules comprised of *Vhl/Pbrm1*-null cells occurred as early as 5 months after the induced concomitant gene loss. Further dysplastic tubules were observed in mice that lost *Pbrm1* but only one copy of *Vhl* 12 months after recombination. Whether this is owed to the biallelic loss of *Pbrm1* alone or caused by an interaction of monoallelic *Vhl* loss and biallelic *Pbrm1* loss remains elusive and should be ground for future investigation.

4.3 Size of tdTomato-positive cell clusters increases in VPKO cortices over time

Having established qualitatively that concomitant loss of *Pbrm1* and *Vhl* but also loss of *Pbrm1* in combination with monoallelic *Vhl* loss leads to morphological abnormalities in the renal cortex using this model, the next goal was to quantify these observed morphological changes. Hence, a robust digital pathology workflow developed in QuPath was established utilising, a neuronal-network-based pixel classifier, trained to accurately detect and quantify

tdTomato-positive clusters within the cortex of scanned kidney sections. This method allowed for a detailed analysis of cluster formation and size distribution across different genotypes and time points, revealing critical information about the underlying mechanisms driving tumour formation.

This analysis demonstrated that in the absence of both *Vhl* and *Pbrm1* (VPKO), there was a significant increase in the size of tdTomato-positive clusters over time, particularly when compared to the other genotypes (ConKO, VKO, and ConPKO). Notably, while VKO mice displayed a modest but significant increase in medium-sized clusters (6-15 cells), this increase was much more pronounced in VPKO mice. The VPKO genotype also uniquely exhibited a significant rise in large clusters (15+ cells), a phenomenon absent in other genotypes. This suggests that the concomitant loss of *Vhl* and *Pbrm1* exerts a synergistic effect, enhancing cellular proliferation or survival in a way neither gene's loss alone can achieve. These findings are in line with prior research that highlights the roles of *Vhl* and *Pbrm1* as tumour suppressors and suggests their combined loss accelerates tumorigenic processes (11–13).

Interestingly, while tdTomato-positive cells in VKO and VPKO cortices exhibit a similar increase in proportion over time, only the average size of VPKO clusters increased significantly over time. Alongside the significant increase in large clusters (15+ cells) only observed in VPKO cortices, these findings suggest that *Vhl/Pbrm1*-loss not only permits the formation of larger clusters but also causes the loss of some tdTomato-positive cells. This is reflected in the significant decrease of single cells and small clusters (2-5 cells) in VPKO cortices which is larger by number than in VKO cortices.

Earlier work on the same mouse model has shown an initial increase in the proportion of cycling tdTomato-positive cells (tdTomato + Ki67 positive) in the cortex of VKO mice when compared to ConKO at the early time point (14). This early proliferation was not sustained at the late time point. The increase in the proportion of large tdTomato-positive clusters (15+ cells)

observed in this study might suggest that the loss of *Pbrm1* in *Vhl*-null cells aids in sustaining this initial proliferative effect caused by *Vhl*-loss. This is supported by the absence of the expansion of tdTomato-positive cells in the cortex of ConPKO mice alongside the absence of size increase of tdTomato-positive cell clusters. These findings suggest that *Pbrm1*-loss on its own does not affect cell proliferation directly but creates a permissive environment for some tdTomato-positive cell expansion driven by *Vhl*-loss. This is of great interest for future research as studying proliferation in *Vhl/Pbrm1*-null cell clusters *via* Ki67 staining or BrdU supplementation could elucidate the origin of the observed formation of larger clusters. In addition to studying proliferation in tdTomato-positive cell clusters, investigating apoptosis markers might explain the observed decrease in single cells and small clusters in VPKO cortices. Further, due to the previously reported effects of *Pbrm1* in chromosome stability (33), it would be of interest to study the acquisition of DNA damage in *Vhl/Pbrm*1-null cell clusters.

Taken together, the trained neuronal network-based pixel classifier successfully detected contiguous tdTomato-positive cell clusters. Built into a QuPath workflow this enabled high-throughput analysis of scanned tissue sections and quantification of tdTomato-positive cluster size. This revealed that only cortical *Vhl/Pbrm1*-null clusters significantly expand towards large clusters (15+ cells) over time. This method of tracking tdTomato-positive clusters over time offers a way of monitoring early events of tumour development which could be potentially of use for testing therapeutical intervention. Further, this workflow could help to solve open questions about the mechanisms of cluster or tumour formation by potentially expanding the workflow to detect additional markers in clusters.

4.4 *Pbrm1* loss causes only minor transcriptomic changes in *Vhl*-deficient renal tubular epithelial cells

Having observed major morphological alterations in *Vhl*-null cells upon loss of *Pbrm1* 12 months after recombination, the next step was to identify any transcriptional changes potentially contributing to this early onset of tumorigenesis. To determine changes caused by *Pbrm1* loss in *Vhl*-null cells and to pinpoint a potential point of interaction of *Vhl* and *Pbrm1* loss, *Vhl*-null cells were compared to *Vhl/Pbrm1*-null and *Vhl*-competent cells using bulk RNA sequencing on FAC sorted tdTomato positive cells. With *Pbrm1* being a central component of the SWI/SNF chromatin remodelling complex PBAF its loss can affect genome accessibility and chromatin organisation and therefore transcription (29). Previous studies have described *Pbrm1* as a target recognition subunit of PBAF and reported that its absence in VHL-null ccRCC cell lines caused a loss of target specificity of the PBAF complex leading to the expression of pro-tumorigenic NF-κB target genes (32). Further, the expression of *PBRM1* correlated with p21 levels in human kidney cancer samples. It has been shown *in vitro* that PBRM1 can interact with p53, recruit it to its target promotor, and enhance its transcriptional activity (70). Generally, PBRM1 deficient ccRCC tumours have been associated with a more open chromatin confirmation in comparison to PBRM1 sufficient tumours (71). Interestingly, the literature is not clear on the molecular basis of how *Vhl* loss and *Pbrm1* loss interact. There are contradicting reports about the effects of *Pbrm1* loss on *Vhl* deficient cells concerning HIF1A and HIF2A target gene expression. In vitro studies have shown that PBRM1 loss in VHL-deficient Caki2 cells diminishes the HIF transcriptional response (72). On the other hand, similar studies have associated PBRM1 inactivation in VHL-deficient ccRCC cell lines with an amplification of the HIF transcriptional response (73). The latter is in agreement with *in vivo* studies that have utilised a mouse line introducing *Vhl*-, *Pbrm1*-, or *Vhl/Pbrm1*-loss in the renal tubular epithelium driven by *Ksp-Cre* recombination. Here, bulk RNA sequencing has shown

that *Pbrm1* loss amplifies HIF1A and STAT3 signalling incurred by *Vhl* loss alongside the upregulation of genes involved in focal adhesion (11). In contrast to this study, the expression of tdTomato upon *Vhl* loss enables the isolation of only renal tubular epithelial cells which have lost *Vhl* and *Pbrm1*. Therefore, RNA sequencing was conducted on FAC-sorted cells to ensure capturing changes in the transcriptome only caused by *Vhl* and *Pbrm1* loss.

Our findings using bulk RNA sequencing mostly stand in contrast to these previous studies. The data indicate that loss of *Pbrm1* has only very little impact on the transcriptome of *Vhl*-deficient RTE cells *in vivo*. A comparison of the transcriptome of *Vhl*-deficient and *Vhl/Pbrm1*-deficient RTE cells revealed that more genes were downregulated after *Pbrm1*-loss rather than upregulated (Figure 3.9). This suggests that *Pbrm1-loss* may not drastically alter the transcriptome directly but have a rather fine-tuning, restricting effect on gene expression. This is intriguing given the well-documented roles of *Pbrm1* in chromatin remodelling, which typically involves widespread effects on gene expression. Nonetheless, this study was able to confirm the findings of a previous report which showed the involvement of *Pbrm1* in focal adhesion and cell adhesion *in vivo* (11,72). Interestingly, the most upregulated gene of the latter pathway is the vascular cell adhesion molecule (*Vcam1*), a cell adhesion molecule that has been associated with ccRCC cells of origin in previous studies (14,74,75). Further, the data of this study suggests that HIF1A and HIF2A target genes are differentially regulated upon *Pbrm1* loss in *Vhl*-null cells leading to an upregulation or stabilization of HIF1A targets and a downregulation of HIF2 targets. This in part agrees with the mentioned *in vivo* study which found HIF1A signalling to be upregulated (11). Surprisingly, these findings contradict the expectations that *Pbrm1*-loss creates a permissive environment for *Vhl*-induced oncogenic pathways as reports have described HIF1A to be more tumour-suppressing, and HIF2A to be more oncogenic (76). Taken together, this might not pose as the mechanism behind tumorigenesis but could potentially explain the phenotypical difference between PBRM1-

deficient and PBRM1-sufficient tumours, the latter of which have shown to be more aggressive (77).

The contradicting results between this study and previous studies might arise due to various reasons. When comparing our results to the results of the mentioned *in vivo* study investigating transcriptional changes after *Vhl/Pbrm1* loss (33), one has to note that the *Vhl*- and *Vhl/Pbrm1*-knock out was induced using different Cre-recombinase systems. In this study, inducible *Pax8-CreER*^{T2} was used to target mostly proximal tubules of the renal tubular epithelium for *Vhl*- and *Vhl/Pbrm1*-knock out. In the comparable study, a constitutively active *Ksp-Cre* was used which targets distal convoluted tubules and collecting ducts more commonly rather than proximal tubules in the RTE (67). Moreover, was bulk RNA sequencing in this study conducted on FAC sorted, tdTomato-positive cells from kidneys harvested 12 months after recombination as opposed to whole kidneys of 12-week-old mice in the case of the Ksp-Cre driven knock-out study. Additionally, differences occur between this and previous studies with regards to the influence of *Pbrm1* on HIF1A and HIF2A target genes in *Vhl*-null cells. Here, the definition of HIF1A and HIF2A targets varies which makes it difficult to compare findings.

Overall, our study suggests that contrary to previous reports, *Pbrm1* loss in *Vhl*-null renal tubular epithelial cells *in vivo* does not lead to widespread changes in the transcriptome which could explain the formation of morphological abnormalities and tumours after concomitant *Vhl/Pbrm1*-loss. This analysis further implies that, although *Pbrm1* is affecting the expression of HIF1A and HIF2A target genes, this differential regulation cannot explain the observed onset of tumorigenesis. Further, this suggests other mechanisms than the role of *Pbrm1* as a PBAF component to be the driving force behind *Pbrm1*-loss-induced tumorigenesis in *Vhl*-null cells. A proposed mechanism here is the interaction of PBRM1 with the methylated cytoskeleton of the mitotic spindle contributing to chromosome stability during mitosis (33). On the other hand, more reports also suggest the involvement of *Pbrm1* in translation

suggesting it is associated with translation initiation through nucleosome profiling (78,79). In conclusion, this study has shown that *Pbrm1*-loss in *Vhl*-null cells has only minor, fine-tuning effects on the transcriptome with more downregulating than upregulating character. Therefore, of great interest for future research, is investigating mechanisms that involve *Pbrm1* but do not directly influence gene expression.

4.5 Limitations and Future Implications

The little changes observed in the transcriptome of *Vhl/Pbrm1*-null renal tubular epithelial cells when compared to *Vhl*-null cells are surprising not only in contrast to the published literature but also with regards to the vast morphological alteration of *Vhl/Pbrm1*-null cell clusters. This might suggest that the role of *Pbrm1* as a tumour suppressor gene does not derive from its function in the chromatin remodelling complex PBAF. This implies that the role of PBRM1 in chromosome stability is a suitable candidate for future investigation. As revised above, loss of PBRM1 has been shown to increase chromosome instability and cytoskeletal dysfunction (33). This way PBRM1 loss could induce oncogenic mutations without influencing overall gene expression. Moreover, other studies have shown that PBRM1 loss can rescue replication stress induced by VHL loss and therefore restore the proliferative potential and cellular fitness of cells which could contribute to the little change in transcription observed (12). Therefore, further investigation should be directed towards a potential accumulation of DNA damage in *Vhl/Pbrm1*-null cells and compared to *Vhl*-null and *Vhl*-haploinsufficient cells. Immunofluorescence staining and subsequent microscopy give insight into the accumulation of DNA damage (yH2X) and could potentially be used to uncover cytoskeletal disorganisation, especially in cycling cells. In addition to that it has been reported that the effects of PBRM1 loss, with respect to its function in genome stability, can induce the formation of micronuclei

(33). Since the HALO AI cell detection system showed great consistency and success in the detection of nuclei a suggestion would be to implement this system to analyse and compare the nuclear size of tdTomato-positive cells in the cortex of ConKO, VKO, ConPKO, and VPKO mice.

Another possible explanation for why *Vhl*-null cells exhibited only little change in the transcriptome upon *Pbrm1* loss despite the presence of distinct morphological abnormalities could be that morphologically altered cell clusters are lost during dissociation or FAC-sorting. This potential limitation could be overcome by employing laser-capture microdissection (80). Here, tdTomato staining enables the extraction of morphologically altered or normal cell clusters and adjacent tdTomato-negative healthy tissue of ConKO, ConPKO, VKO and VPKO cortices which can subsequently be subjected to transcriptome or proteome analysis. To further confirm the expression of individual genes in tdTomato-positive cells, RNA scope in-situ hybridisation assays could be applied in combination with tdTomato immunostaining.

An additional limitation of this model is that it is not possible to determine whether cells of a tdTomato-positive cluster are all progenies of the same cell or whether the cluster is comprised of the progenies of multiple cells. Although laborious the addition of lineage tracing to this mouse model could potentially bring further insight into the origin and development of ccRCC (81,82).

Important to note is also that this mouse model couples the expression of tdTomato to the inactivation of *Vhl* only. Although immunoblotting and immunostaining have confirmed that in the case of ConPKO and VPKO mice cells expressing tdTomato will have lost *Vhl* and *Pbrm1* it is difficult to say how many tdTomato-negative cells in these mice have lost *Pbrm1*. This would result in *Pbrm1*-null cells with monoallelic *Vhl*-loss in the case of VPKO and *Pbrm1*-null cells in the case of ConPKO which are tdTomato-negative. It is hard to say to what extent this is influencing our analysis but as shown in Figure 3.3C and D for ConPKO mice,

cell clusters with morphological abnormalities are mostly tdTomato-positive but interspaced with tdTomato-negative cells. These cells could potentially have lost only *Pbrm1* without recombining the Vhl^{pjr} allele.

On the other hand, no other group has previously reported morphological abnormalities in renal tubular epithelial cells that have lost *Pbrm1* alone. Therefore, it is important to note that the mouse model used by us is unable to provide information about the effects of *Pbrm1* loss by itself, only in combination with monoallelic *Vhl*-loss. Hence, if it holds true that the main role of *Pbrm1* as a tumour suppressor gene is maintaining genome stability (33), it is imaginable that cells in these rather rare morphologically altered clusters in ConPKO mice have acquired a mutation in their second (wild-type) *Vhl*-allele and therefore being *Vhl/Pbrm1* null. This could be tested by serial sectioning the ConPKO kidney with clusters of altered morphology and immunostaining these serial sections for tdTomato, HIF1A and HIF2A respectively.

5. Conclusion

In summary, this study was able to reproduce the findings of previous groups which have shown that biallelic inactivation of *Vhl* and *Pbrm1* in the renal tubular epithelium of mice leads to the formation of cysts and ccRCC-like lesions. Coupling *Vhl* loss to the expression of a tdTomato reporter gene enabled the visualisation of cells that have lost either or both tumour suppressor genes before they undergo morphological alteration. This not only made it possible to detect minor morphological alterations and an earlier time point than previous groups but also gave valuable insight into the expansion and survival of *Vhl/Pbrm1*-null cells in the renal cortex over time. Here it was shown that additional loss of *Pbrm1* does not affect the previously reported expansion and survival of *Vhl*-null cells in the cortex over time which indicates. This indicates that *Vhl*-loss solely drives the expansion of *Vhl/Pbrm1* cells in the renal cortex. Further, this study provided a workflow for the detection and subsequent quantification of tdTomato-positive cell clusters. This quantification showed that *Vhl/Pbrm1*-null cells in the renal cortex form larger clusters over time than *Vhl*-null, *Vhl*-haploinsufficient and *Pbrm1*-null/*Vhl*-haploinsufficient cells. Therefore, the increase in cell cluster size is a synergistic effect of *Vhl/Pbrm1*-loss.

Surprisingly transcriptome analysis yielded only minor changes in gene expression in *Vhl*-null cells upon *Pbrm1*-loss with more genes being downregulated than upregulated. This lack of change in transcription despite profound changes in the morphology of tdTomato-positive cell clusters indicates that *Pbrm1* is exhibiting its role as a tumour suppressor not through its function in the PBAF complex.

Taken together this study has provided new insight into early histological changes of *Vhl/Pbrm1*-null renal tubular epithelial cells with respect to survival, expansion and cell clustering. A high-throughput pipeline for the histological detection and quantification of

tdTomato-positive cell clusters in the kidney was developed which provides the basis for further investigation and enables the expansion for additional markers which can be used to investigate drug responses and underlying mechanisms of cell clustering. Further does this study suggest the role of *Pbrm1* as a tumour suppressor gene outside of the PBAF complex and therefore creates the basis for future investigations.

6. Supplementary Figures

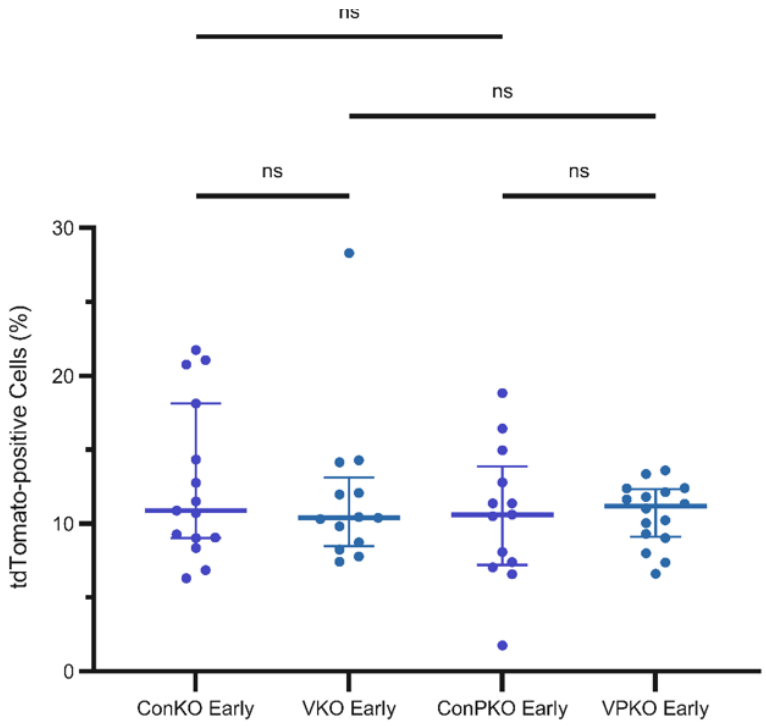

Supplementary Figure 1: Quantitative comparison of the proportions of tdTomato-positive cells in the renal cortex of ConKO and ConPKO mice at the early and late time point: *Percentage of tdTomato-positive cells in the renal cortex, as detected by the AI-based HALO® cell detection system in the cortices of 15 ConKO, 13 ConPKO, 13 VKO and 15 VPKO kidney sections at the early time point (1-3 weeks). ANOVA test was used to test for group variability and significance in multiple comparisons was tested using the non-parametric Kruskal-Wallis-test.*

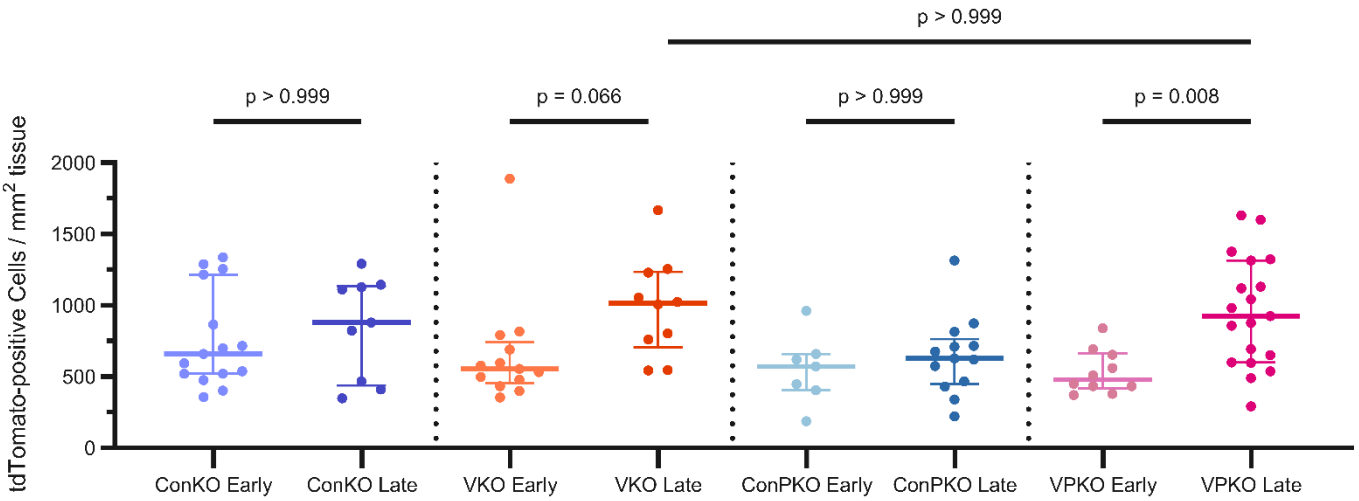

Supplementary Figure 2: Quantitative comparison of the number of tdTomato-positive cells per mm² tissue of renal cortex of ConKO, ConPKO, VKO and VPKO mice at the early and late time point:

Number of tdTomato-positive cells per mm² of renal cortex, as detected by the AI-based HALO® cell detection system in the cortices of 15 ConKO, 7 ConPKO, 13 VKO and 10 VPKO kidney sections at the early time point (1-3 weeks) and 9 ConKO, 13 ConPKO, 10 VKO and 19 VPKO at the late time point (>4 months). ANOVA test was used to test for group variability and significance in multiple comparisons was tested using the non-parametric Kruskal-Wallis-test.

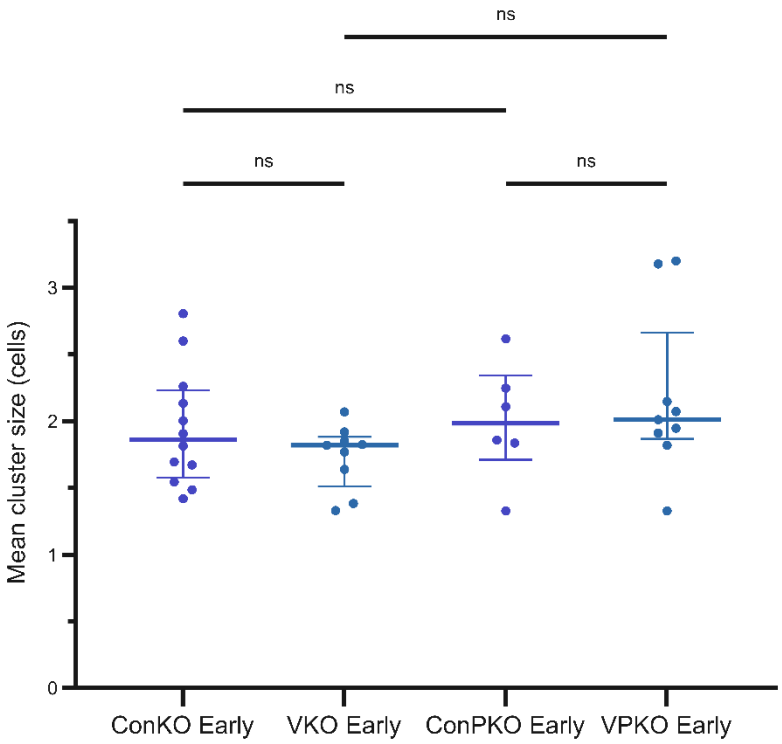

Supplementary Figure 3: Comparison of the mean cluster size in ConKO, ConPKO cortices at the early and late time point: *Contiguous tdTomato-positive clusters were detected by the trained neuronal network-based pixel classifier in QuPath with subsequent cell counting within the annotated clusters. The mean value of the number of cells detected in each cluster in the cortices of 12 ConKO, 6 ConPKO, 9 VKO and 9VPKO kidney sections at the early time point. Kidneys were harvested 1-3 weeks (early time point). ANOVA test was used to test for group variability and significance in multiple comparisons was tested using the non-parametric Kruskal-Wallis-test.*

7. References

1. Feng X, Zhang L, Tu W, Cang S. Frequency, incidence and survival outcomes of clear cell renal cell carcinoma in the United States from 1973 to 2014. Medicine (Baltimore). 2019 Aug 2;98(31):e16684.

2. Du W, Zhang L, Brett-Morris A, Aguila B, Kerner J, Hoppel CL, et al. HIF drives lipid deposition and cancer in ccRCC via repression of fatty acid metabolism. Nat Commun. 2017 Nov 24;8(1):1769.

3. Chen S lu, Huang Q sheng, Huang Y hua, Yang X, Yang M ming, He Y fan, et al. GYS1 induces glycogen accumulation and promotes tumor progression via the NF-κB pathway in Clear Cell Renal Carcinoma. Theranostics. 2020 Jul 14;10(20):9186–99.

4. Szücs S, Müller-Brechlin R, DeRiese W, Kovacs G. Deletion 3p: The only chromosome loss in a primary renal cell carcinoma. Cancer Genet Cytogenet. 1987 Jun 1;26(2):369–73.

5. Mitchell TJ, Turajlic S, Rowan A, Nicol D, Farmery JHR, O'Brien T, et al. Timing the Landmark Events in the Evolution of Clear Cell Renal Cell Cancer: TRACERx Renal. Cell. 2018 Apr 19;173(3):611-623.e17.

6. Shuch B, Vourganti S, Middleton L, Linehan WM. Defining early-onset kidney cancer: Implications for genetic counseling. J Clin Oncol. 2013 Feb 20;31(6_suppl):342–342.

7. Maher E r. Inherited renal cell carcinoma. Br J Urol. 1996;78(4):542–5.

8. Sato Y, Yoshizato T, Shiraishi Y, Maekawa S, Okuno Y, Kamura T, et al. Integrated molecular analysis of clear-cell renal cell carcinoma. Nat Genet. 2013 Aug;45(8):860–7.

9. Nickerson ML, Jaeger E, Shi Y, Durocher JA, Mahurkar S, Zaridze D, et al. Improved Identification of von Hippel-Lindau Gene Alterations in Clear Cell Renal Tumors. Clin Cancer Res. 2008 Aug 1;14(15):4726–34.

10. Gnarra JR, Tory K, Weng Y, Schmidt L, Wei MH, Li H, et al. Mutations of the VHL tumour suppressor gene in renal carcinoma. Nat Genet. 1994 May;7(1):85–90.

11. Nargund AM, Pham CG, Dong Y, Wang PI, Osmangeyoglu HU, Xie Y, et al. The SWI/SNF Protein PBRM1 Restrains VHL-Loss-Driven Clear Cell Renal Cell Carcinoma. Cell Rep. 2017 Mar 21;18(12):2893–906.

12. Espana-Agusti J, Warren A, Chew SK, Adams DJ, Matakidou A. Loss of PBRM1 rescues VHL dependent replication stress to promote renal carcinogenesis. Nat Commun. 2017 Dec 11;8(1):2026.

13. Gu YF, Cohn S, Christie A, McKenzie T, Wolff N, Do QN, et al. Modeling Renal Cell Carcinoma in Mice: Bap1 and Pbrm1 Inactivation Drive Tumor Grade. Cancer Discov. 2017 Aug;7(8):900–17.

14. Kurlekar S, Lima JDCC, Li R, Lombardi O, Masson N, Barros AB, et al. Oncogenic Cell Tagging and Single-Cell Transcriptomics Reveal Cell Type–Specific and Time-Resolved Responses to Vhl Inactivation in the Kidney. Cancer Res. 2024 Jun 4;84(11):1799–816.

15. Varela I, Tarpey P, Raine K, Huang D, Ong CK, Stephens P, et al. Exome sequencing identifies frequent mutation of the SWI/SNF complex gene PBRM1 in renal carcinoma. Nature. 2011 Jan;469(7331):539–42.

16. Peña-Llopis S, Vega-Rubín-de-Celis S, Liao A, Leng N, Pavía-Jiménez A, Wang S, et al. BAP1 loss defines a new class of renal cell carcinoma. Nat Genet. 2012 Jul;44(7):751–9.

17. Dalgliesh GL, Furge K, Greenman C, Chen L, Bignell G, Butler A, et al. Systematic sequencing of renal carcinoma reveals inactivation of histone modifying genes. Nature. 2010 Jan;463(7279):360–3.

18. Iwai K, Yamanaka K, Kamura T, Minato N, Conaway RC, Conaway JW, et al. Identification of the von Hippel–Lindau tumor-suppressor protein as part of an active E3 ubiquitin ligase complex. Proc Natl Acad Sci. 1999 Oct 26;96(22):12436–41.

19. Lisztwan J, Imbert G, Wirbelauer C, Gstaiger M, Krek W. The von Hippel–Lindau tumor suppressor protein is a component of an E3 ubiquitin–protein ligase activity. Genes Dev. 1999 Jul 15;13(14):1822–33.

20. Hon WC, Wilson MI, Harlos K, Claridge TDW, Schofield CJ, Pugh CW, et al. Structural basis for the recognition of hydroxyproline in HIF-1 alpha by pVHL. Nature. 2002 Jun 27;417(6892):975–8.

21. Schofield CJ, Ratcliffe PJ. Oxygen sensing by HIF hydroxylases. Nat Rev Mol Cell Biol. 2004 May;5(5):343–54.

22. Jiang BH, Rue E, Wang GL, Roe R, Semenza GL. Dimerization, DNA binding, and transactivation properties of hypoxia-inducible factor 1. J Biol Chem. 1996 Jul 26;271(30):17771–8.

23. Smythies JA, Sun M, Masson N, Salama R, Simpson PD, Murray E, et al. Inherent DNA-binding specificities of the HIF-1α and HIF-2α transcription factors in chromatin. EMBO Rep. 2019 Jan;20(1):e46401.

24. Benita Y, Kikuchi H, Smith AD, Zhang MQ, Chung DC, Xavier RJ. An integrative genomics approach identifies Hypoxia Inducible Factor-1 (HIF-1)-target genes that form the core response to hypoxia. Nucleic Acids Res. 2009 Aug 1;37(14):4587–602.

25. Rankin EB, Tomaszewski JE, Haase VH. Renal Cyst Development in Mice with Conditional Inactivation of the von Hippel-Lindau Tumor Suppressor. Cancer Res. 2006 Mar 1;66(5):2576–83.

26. Fu L, Wang G, Shevchuk MM, Nanus DM, Gudas LJ. Activation of HIF2α in Kidney Proximal Tubule Cells Causes Abnormal Glycogen Deposition but not Tumorigenesis. Cancer Res. 2013 Apr 30;73(9):2916–25.

27. Schietke RE, Hackenbeck T, Tran M, Günther R, Klanke B, Warnecke CL, et al. Renal Tubular HIF-2α Expression Requires VHL Inactivation and Causes Fibrosis and Cysts. PLOS ONE. 2012 Jan 27;7(1):e31034.

28. Owen-Hughes T, Utley RT, Côté J, Peterson CL, Workman JL. Persistent Site-Specific Remodeling of a Nucleosome Array by Transient Action of the SWI/SNF Complex. Science. 1996 Jul 26;273(5274):513–6.

29. Hodges C, Kirkland JG, Crabtree GR. The Many Roles of BAF (mSWI/SNF) and PBAF Complexes in Cancer. Cold Spring Harb Perspect Med. 2016 Aug;6(8):a026930.

30. Thompson M. Polybromo-1: The chromatin targeting subunit of the PBAF complex. Biochimie. 2009 Mar 1;91(3):309–19.

31. Centore RC, Sandoval GJ, Soares LMM, Kadoch C, Chan HM. Mammalian SWI/SNF Chromatin Remodeling Complexes: Emerging Mechanisms and Therapeutic Strategies. Trends Genet. 2020 Dec 1;36(12):936–50.

32. Yao X, Hong JH, Nargund AM, Ng MSW, Heng HL, Li Z, et al. PBRM1-deficient PBAF complexes target aberrant genomic loci to activate the NF-κB pathway in clear cell renal cell carcinoma. Nat Cell Biol. 2023 May;25(5):765–77.

33. Karki M, Jangid RK, Anish R, Seervai RNH, Bertocchio JP, Hotta T, et al. A cytoskeletal function for PBRM1 reading methylated microtubules. Sci Adv. 2021 Apr;7(14):eabf2866.

34. Cai W, Su L, Liao L, Liu ZZ, Langbein L, Dulaimi E, et al. PBRM1 acts as a p53 lysine-acetylation reader to suppress renal tumor growth. Nat Commun. 2019 Dec 20;10(1):5800.

35. Cai W, Su L, Yang H. PBRM1 suppresses tumor growth as a novel p53 acetylation reader. Mol Cell Oncol. 2020 May 3;7(3):1729680.

36. Creighton CJ, Morgan M, Gunaratne PH, Wheeler DA, Gibbs RA, Gordon Robertson A, et al. Comprehensive molecular characterization of clear cell renal cell carcinoma. Nature. 2013 Jul;499(7456):43–9.

37. Haase VH, Glickman JN, Socolovsky M, Jaenisch R. Vascular tumors in livers with targeted inactivation of the von Hippel-Lindau tumor suppressor. Proc Natl Acad Sci U S A. 2001 Feb 13;98(4):1583–8.

38. Wurster AL, Precht P, Becker KG, Wood WH, Zhang Y, Wang Z, et al. IL-10 transcription is negatively regulated by BAF180, a component of the SWI/SNF chromatin remodeling enzyme. BMC Immunol. 2012 Feb 15;13(1):9.

39. Rubera I, Poujeol C, Bertin G, Hasseine L, Counillon L, Poujeol P, et al. Specific Cre/Lox Recombination in the Mouse Proximal Tubule. J Am Soc Nephrol. 2004 Aug;15(8):2050.

40. Pringault E, Robine S, Louvard D. Structure of the human villin gene. Proc Natl Acad Sci. 1991 Dec;88(23):10811–5.

41. Espana-Agusti J, Zou X, Wong K, Fu B, Yang F, Tuveson DA, et al. Generation and Characterisation of a Pax8-CreERT2 Transgenic Line and a Slc22a6-CreERT2 Knock-In Line for Inducible and Specific Genetic Manipulation of Renal Tubular Epithelial Cells. PLoS ONE. 2016 Feb 11;11(2):e0148055.

42. Stebbins CE, Kaelin WG, Pavletich NP. Structure of the VHL-ElonginC-ElonginB complex: implications for VHL tumor suppressor function. Science. 1999 Apr 16;284(5413):455–61.

43. Lallemand Y, Luria V, Haffner-Krausz R, Lonai P. Maternally expressed PGK-Cre transgene as a tool for early and uniform activation of the Cre site-specific recombinase. Transgenic Res. 1998 Mar 1;7(2):105–12.

44. Kriz W, Kaissling B. Structural Organization of the Mammalian Kidney. Seldin Giebischs Kidney. 2008 Jan 1;1:479–563.

45. Comprehensive Clinical Nephrology von Richard J. Johnson | ISBN 978-1-4557-5838-8 | Fachbuch online kaufen - Lehmanns.de [Internet]. [cited 2024 Sep 7]. Available from: https://www.lehmanns.de/shop/medizin-pharmazie/29742963-9781455758388-comprehensive-clinical-nephrology

46. Bankhead P, Loughrey MB, Fernández JA, Dombrowski Y, McArt DG, Dunne PD, et al. QuPath: Open source software for digital pathology image analysis. Sci Rep. 2017 Dec 4;7(1):16878.

47. Kim D, Paggi JM, Park C, Bennett C, Salzberg SL. Graph-based genome alignment and genotyping with HISAT2 and HISAT-genotype. Nat Biotechnol. 2019 Aug;37(8):907–15.

48. Anders S, Pyl PT, Huber W. HTSeq—a Python framework to work with high-throughput sequencing data. Bioinformatics. 2015 Jan 15;31(2):166–9.

49. Love MI, Huber W, Anders S. Moderated estimation of fold change and dispersion for RNA-seq data with DESeq2. Genome Biol. 2014 Dec 5;15(12):550.

50. Wickham H, Chang W, Henry L, Pedersen TL, Takahashi K, Wilke C, et al. ggplot2: Create Elegant Data Visualisations Using the Grammar of Graphics [Internet]. 2024 [cited 2024 Sep 7]. Available from: https://cran.r-project.org/web/packages/ggplot2/index.html

51. Yu G, Wang LG, Han Y, He QY. clusterProfiler: an R Package for Comparing Biological Themes Among Gene Clusters. OMICS J Integr Biol. 2012 May;16(5):284–7.

52. Gao CH, Yu G, Dusa [aut A, venn cph] (Adrian D is the author and copyright holder of, diagram.) where ggVennDiagram imports the polygon coordinates enabling 5 7 sets V, Akyol TY. ggVennDiagram: A 'ggplot2' Implement of Venn Diagram [Internet]. 2024 [cited 2024 Sep 7]. Available from: https://cran.r-project.org/web/packages/ggVennDiagram/index.html

53. Raivo Kolde. pheatmap: Pretty Heatmaps [Internet]. 2010 [cited 2024 Sep 7]. p. 1.0.12. Available from: https://CRAN.R-project.org/package=pheatmap

54. Lombardi O, Li R, Halim S, Choudhry H, Ratcliffe PJ, Mole DR. Pan-cancer analysis of tissue and single-cell HIF-pathway activation using a conserved gene signature. Cell Rep [Internet]. 2022 Nov 15 [cited 2024 Sep 1];41(7). Available from: https://www.cell.com/cell-reports/abstract/S2211-1247(22)01523-6

55. Jean JC, Rich CB, Joyce-Brady M. Hypoxia results in an HIF-1-dependent induction of brain-specific aldolase C in lung epithelial cells. Am J Physiol-Lung Cell Mol Physiol. 2006 Nov;291(5):L950–6.

56. Moon EJ, Mello SS, Li CG, Chi JT, Thakkar K, Kirkland JG, et al. The HIF target MAFF promotes tumor invasion and metastasis through IL11 and STAT3 signaling. Nat Commun. 2021 Jul 14;12(1):4308.

57. Mukhopadhyay CK, Mazumder B, Fox PL. Role of Hypoxia-inducible Factor-1 in Transcriptional Activation of Ceruloplasmin by Iron Deficiency *. J Biol Chem. 2000 Jul 14;275(28):21048–54.

58. Leichtweiss HP, Lübbers DW, Weiss Ch, Baumgärtl H, Reschke W. The oxygen supply of the rat kidney: Measurements of intrarenalpO2. Pflüg Arch. 1969 Dec 1;309(4):328–49.

59. Aukland K, Krog J. Renal Oxygen Tension. Nature. 1960 Nov;188(4751):671–671.

60. Welford SM, Dorie MJ, Li X, Haase VH, Giaccia AJ. Renal Oxygenation Suppresses VHL Loss-Induced Senescence That Is Caused by Increased Sensitivity to Oxidative Stress. Mol Cell Biol. 2010 Oct 1;30(19):4595–603.

61. Baba M, Hirai S ichi, Kawakami S, Kishida T, Sakai N, Kaneko S, et al. Tumor suppressor protein VHL is induced at high cell density and mediates contact inhibition of cell growth. Oncogene. 2001 May;20(22):2727–36.

62. Maxwell PH, Wiesener MS, Chang GW, Clifford SC, Vaux EC, Cockman ME, et al. The tumour suppressor protein VHL targets hypoxia-inducible factors for oxygen-dependent proteolysis. Nature. 1999 May;399(6733):271–5.

63. Genega EM, Ghebremichael M, Najarian R, Fu Y, Wang Y, Argani P, et al. Carbonic anhydrase IX expression in renal neoplasms: correlation with tumor type and grade. Am J Clin Pathol. 2010 Dec;134(6):873–9.

64. Wykoff CC, Beasley NJ, Watson PH, Turner KJ, Pastorek J, Sibtain A, et al. Hypoxia-inducible expression of tumor-associated carbonic anhydrases. Cancer Res. 2000 Dec 15;60(24):7075–83.

65. Wang H, Qu Y, Dai B, Zhu Y, Shi G, Zhu Y, et al. PBRM1 regulates proliferation and the cell cycle in renal cell carcinoma through a chemokine/chemokine receptor interaction pathway. PLOS ONE. 2017 Aug 28;12(8):e0180862.

66. Gu X, Enane F, Tohme R, Schuerger C, Radivoyevitch T, Parker Y, et al. PBRM1 loss in kidney cancer unbalances the proximal tubule master transcription factor hub to repress proximal tubule differentiation. Cell Rep. 2021 Sep 21;36(12):109747.

67. Shao X, Somlo S, Igarashi P. Epithelial-Specific Cre/lox Recombination in the Developing Kidney and Genitourinary Tract. J Am Soc Nephrol. 2002 Jul;13(7):1837.

68. Narlis M, Grote D, Gaitan Y, Boualia SK, Bouchard M. Pax2 and Pax8 Regulate Branching Morphogenesis and Nephron Differentiation in the Developing Kidney. J Am Soc Nephrol. 2007 Apr;18(4):1121.

69. Maher ER, Neumann HP, Richard S. von Hippel–Lindau disease: A clinical and scientific review. Eur J Hum Genet. 2011 Jun;19(6):617–23.

70. Cai W, Su L, Liao L, Liu ZZ, Langbein L, Dulaimi E, et al. PBRM1 acts as a p53 lysine-acetylation reader to suppress renal tumor growth. Nat Commun. 2019 Dec 20;10(1):5800.

71. Wu Y, Terekhanova NV, Caravan W, Naser Al Deen N, Lal P, Chen S, et al. Epigenetic and transcriptomic characterization reveals progression markers and essential pathways in clear cell renal cell carcinoma. Nat Commun. 2023 Mar 27;14(1):1681.

72. Chowdhury B, Porter EG, Stewart JC, Ferreira CR, Schipma MJ, Dykhuizen EC. PBRM1 Regulates the Expression of Genes Involved in Metabolism and Cell Adhesion in Renal Clear Cell Carcinoma. PLOS ONE. 2016 Apr 21;11(4):e0153718.

73. Gao W, Li W, Xiao T, Liu XS, Kaelin WG. Inactivation of the PBRM1 tumor suppressor gene amplifies the HIF-response in VHL−/− clear cell renal carcinoma. Proc Natl Acad Sci. 2017 Jan 31;114(5):1027–32.

74. Muto Y, Wilson PC, Ledru N, Wu H, Dimke H, Waikar SS, et al. Single cell transcriptional and chromatin accessibility profiling redefine cellular heterogeneity in the adult human kidney. Nat Commun. 2021 Apr 13;12(1):2190.

75. Young MD, Mitchell TJ, Vieira Braga FA, Tran MGB, Stewart BJ, Ferdinand JR, et al. Single-cell transcriptomes from human kidneys reveal the cellular identity of renal tumors. Science. 2018 Aug 10;361(6402):594–9.

76. Raval RR, Lau KW, Tran MGB, Sowter HM, Mandriota SJ, Li JL, et al. Contrasting Properties of Hypoxia-Inducible Factor 1 (HIF-1) and HIF-2 in von Hippel-Lindau-Associated Renal Cell Carcinoma. Mol Cell Biol. 2005 Jul 1;25(13):5675–86.

77. Kapur P, Peña-Llopis S, Christie A, Zhrebker L, Pavía-Jiménez A, Rathmell WK, et al. Effects on survival of BAP1 and PBRM1 mutations in sporadic clear-cell renal cell carcinoma: a retrospective analysis with independent validation. Lancet Oncol. 2013 Feb;14(2):159–67.

78. Ulicna L, Kimmey SC, Weber CM, Allard GM, Wang A, Bui NQ, et al. The Interaction of SWI/SNF with the Ribosome Regulates Translation and Confers Sensitivity to Translation Pathway Inhibitors in Cancers with Complex Perturbations. Cancer Res. 2022 Aug 16;82(16):2829–37.

79. Shmakova A, Frost M, Batie M, Kenneth NS, Rocha S. PBRM1 Cooperates with YTHDF2 to Control HIF-1α Protein Translation. Cells. 2021 Jun;10(6):1425.

80. Espina V, Wulfkuhle JD, Calvert VS, VanMeter A, Zhou W, Coukos G, et al. Laser-capture microdissection. Nat Protoc. 2006 Aug;1(2):586–603.

81. Hsu YC. The Theory and Practice of Lineage Tracing. Stem Cells Dayt Ohio. 2015 Nov;33(11):3197–204.

82. Li L, Bowling S, McGeary SE, Yu Q, Lemke B, Alcedo K, et al. A mouse model with high clonal barcode diversity for joint lineage, transcriptomic, and epigenomic profiling in single cells. Cell. 2023 Nov 9;186(23):5183-5199.e22.